ELECTRODEPOSITION OF NICKEL AND NICKEL ALLOY COATINGS WITH LAYERED SILICATES FOR ENHANCED CORROSION RESISTANCE AND MECHANICAL PROPERTIES

Jeerapan Tientong, B.S., M.Sc.

Dissertation Prepared for the Degree of

DOCTOR OF PHILOSOPHY

UNIVERSITY OF NORTH TEXAS

August 2014

APPROVED:

Teresa D. Golden, Major Professor
Nandika Anne D'Souza, Co-Major Professor
Adel M.A. Mohamed, Committee Member
Oliver M.R. Chyan, Committee Member
Paul Marshall, Committee Member
William E. Acree Jr., Chair of the Department of Chemistry
Mark Wardell, Dean of the Toulouse Graduate School

Tientong, Jeerapan. Electrodeposition of Nickel and Nickel Alloy Coatings with Layered Silicates for Enhanced Corrosion Resistance and Mechanical Properties. Doctor of Philosophy (Chemistry-Analytical Chemistry), August 2014, 173 pp, 31 tables, 74 illustrations, 334 chapter references.

The new nickel/layered silicate nanocomposites were electrodeposited from different pHs to study the influence on the metal ions/layered silicate plating solution and on the properties of the deposited films. Nickel/layered silicate nanocomposites were fabricated from citrate bath at acidic pHs (1.6−3.0), from Watts' type solution (pH ~4-5), and from citrate bath at basic pH (~9). Additionally, the new nickel/molybdenum/layered silicate nanocomposites were electrodeposited from citrate bath at pH 9.5. The silicate, montmorillonite (MMT), was exfoliated by stirring in aqueous solution over 24 hours. The plating solutions were analyzed for zeta potential, particle size, viscosity, and conductivity to investigate the effects of the composition at various pHs. The preferred crystalline orientation and the crystalline size of nickel, nickel/layered silicate, nickel/molybdenum, and nickel/molybdenum/layered silicate films were examined by X-ray diffraction. The microstructure of the coatings and the surface roughness was investigated by scanning electron microscopy and atomic force microscopy. Nickel/molybdenum/layered silicate nanocomposites containing low content of layered silicate (1.0 g/L) had increase 32 % hardness and 22 % Young's modulus values over the pure nickel/molybdenum alloy films. The potentiodynamic polarization and electrochemical impedance measurements showed that the nickel/molybdenum/layered silicate nanocomposite layers have higher corrosion resistance in 3.5% NaCl compared to the pure alloy films. The corrosion current density of the nickel/molybdenum/layered silicate nanocomposite composed of 0.5 g/L MMT is 0.63 $\mu A\cdot cm^{-2}$ as compare to a nickel/molybdenum alloy which is 2.00 $\mu A\cdot cm^{-2}$.

ACKNOWLEDGEMENTS

First of all, I would like to express my special appreciation to my research advisor, Dr. Teresa D. Golden, without whom this research and dissertation would not have been possible. I would like to thank her for the opportunity to work in her research group which has provided the theory, skill, and confidence I need to tackle many different problems. I would like to thank Dr. Nandika Anne D'Souza for being my co-advisor and generously offering me the opportunity to collaborate in this research and utilize her lab. I would like to thank Dr. Adel M.A. Mohamed as co-supervisor from Qatar University for giving me an opportunity to collaborate in the research grant. I would also like to thank my committee members, Dr. Oliver M.R. Chyan and Dr. Paul Marshall, for their time, comments and constructive critism of my dissertation.

This work was made possible by NPRP grant 4-306-2-111 from the Qatar National Research Fund (A Member of The Qatar Foundation).

I would like to thank you to Dr. Yahia H. Ahmad from Qatar University for co-working with our research team. Special thank you to Dr. Heidi A. Conrad for wonderful recommendation and kindly guiding me in the lab since the first year I joined in Golden group. I would like to thank my entire research group for your great friendship and helpful discussions.

I would like to express my appreciation to Nakhon Sawan Rajabhat University for granting mea scholarship during my Ph.D. study.

Above all, I am grateful to my dearest mom and dad for their uncountable love. Their support and encouragement not only during graduate school, but also throughout my whole life is truly what motivates me every day to continue to work hard and reach my dreams. Thank you to my sister and brother who always give me constant love and encouragement and have taken care of my dad and mom while I was studying abroad. Thank you to Jaranya Sripalaew, my fiancé, who has provided me motivation and enhanced my enthusiasm for life.

TABLE OF CONTENTS

LIST OF TABLES

Page

LIST OF ILLUSTRATIONS

CHAPTER 1

INTRODUCTION TO CHAPTERS

Corrosion is a phenomenon that causes structural failures resulting in considerable preventative maintenance and repair costs. Coatings which incorporated ceramics enhance mechanical strength and high temperature resistance. In the oil field industry, high corrosion resistance and high thermal stability coatings are needed to extend the lifetime of currently used materials. One technique for reducing the corrosion of the metals is to coat them with thin layers of noble metals or alloys. Various techniques such as vapor deposition, dipping, or physical deposition have been utilized. Unfortunately, most coating processes have not been sufficient protecting against corrosion because of grain size and porosity. Electrodeposition is an effective method to synthesize the coating component onto the substrate because it gives a compact dense nanocrystalline coating. The electrodeposition is a convenient synthesis process. Moreover, it is a low cost synthesis process which requires an aqueous plating solution. Coating with metal alloys is a key component to improve corrosion protection. Nickel is a common metal to alloy with other metal elements such as chromium, zinc, copper, or molybdenum. They have very good corrosion resistance, good toughness and good weldability. Molybdenum, a type of refractory metal, is of interest to alloy with nickel to increase the resistance to pitting and crevice corrosion. In addition, molybdenum-nickel alloys improve the tolerance to high heat. Dispersing the layered ceramic into the metal film to improve the mechanical properties is consequently of interest. Once the materials have high hardness and fracture toughness, they are able to resist scratching which typically initiates corrosion. The objective of this work is to electrochemically deposit nickel incorporated with layered silicate platelets and nickel-molybdenum alloy with layered silicate to enhance corrosion resistance and mechanical properties. For an electrodeposition, the bath influences deposition through pH and mass transport of the charge body or particle. We investigate several different baths including citrate bath and Watt's bath at both acidity pH 1.6 to 4.3 and in citrate bath at alkaline pH of 9-9.5. The plating solution of nickel-citrate bath at pH 9.5 helps pave the way to electrodeposit nickel-molybdenum incorporate with layered silicate at the same pH, while the acidic citrate bath will be applied for the nickel-copper-layered silicate deposition. The parameters of the conductivity, viscosity and particle size which are able to influence the fluid movement were studied when plating solution is incorporated with layered silicate particles compared to the pure metal plating solution without adding the particles. The zeta potential and also particle size which influence the stability of the platelets suspending in the plating solution will influence the homogeneity of the solution resulting in the uniform dispersing layered silicate into metal matrix.

Inhibition of corrosion rate is controlled through decreasing the transport rate of the permeating fluid such as water and oxygen. The platelet architecture offers a brick line barrier to corrosion. Additionally, the insulated reinforcement such as ceramic particle is purposed to decrease the corrosion rate. Aruna S.T. and et. al. electrodeposition nickel-alumina nanocomposite onto steel substrate by galvanostatic mode at 15.5 mA/cm^2. The different particle size of alumina powder prepared from various process such as solution combustion process containing pure alpha alumina (40 nm), precipitation method containing pure gamma alumina (5 nm), and commercial alumina containing mixture of alpha, gamma, and delta crystalline phase (40 nm) were incorporated into nickel sulfamate bath and swirled for 24 hours. Nickel composite dispersed with gamma alumina of the finest size offered the superior corrosion resistance, while that containing the pure alpha alumina improved wear resistance. The nanosize particles enable a thin deposition and high dispersion due to offering a high surface area. Dispersing the layered ceramic in the metallic alloy film improve the mechanical properties. Once the materials have high hardness and fracture toughness, they are able to resist scratching which is the initiation of corrosion and a stress cracking corrosion.

In this dissertation, the following questions are explored.

(i) Parameters which influence mass transport of the nickel-MMT during electrochemical deposition.

(ii) Effect of the addition of MMT on the metal deposited crystalline phase.

(iii) Corrosion resistance arising from the pure metal films and MMT modified films.

(iv) Surface hardness values from the pure metal films and MMT modified films.

Chapter 1 covers electrodeposition as a depositing technique for metallic films. Chapter 2 introduces the incorporation of metals, ceramics, and polymers into various matrices as reinforcement materials. Chapter 3 covers the topic of corrosion in metals. Chapters 4-6 cover the data, results, and discussions for the new nanocomposite films produced for this research.

CHAPTER 2

ELECTROCHEMICAL DEPOSITION

2.1 Electrodeposition

Electrodeposition is a process resulting in the formation of a metallic coating on a substrate. This process is achieved through electrochemical reduction of metal ions from an electrolytic solution. Electrodeposition processes primarily involve the transfer of one or more electrons through the interface between electrode and solution, resulting in the formation of a metallic phase on the substrate. Metal ions are dissolved in an aqueous electrolyte solution and the electrons for the reduction reaction are provided by an external power supply [1]. Electrodeposition is a technologically simple and economical technique that has been utilized to produce nanocrystalline coatings with low residual porosity. [2]. Electrodeposition has been an attractive option for coating technology as a result of the following benefits [2]:

- Low cost and industrial applicability, as it involves little modification of existing electroplating technologies.
- Ease of control, as the electrodeposition parameters can be tailored to meet the required crystal size, microstructure and composition of products.
- Versatility, as the process can produce a wide variety of pore free coatings.
- High production rates.

The electrochemical deposition cells are simply comprised of a typical three electrode system including a counter electrode (CE), working electrode (WE) and reference electrode (RE). The electrodes are immersed in a conducting solution called an electrolyte containing dissolved metal salts as metal ions and other additives that enhance coating properties. A typical three-electrode arrangement for my work of an electrochemical cell is shown in figure 2.1.

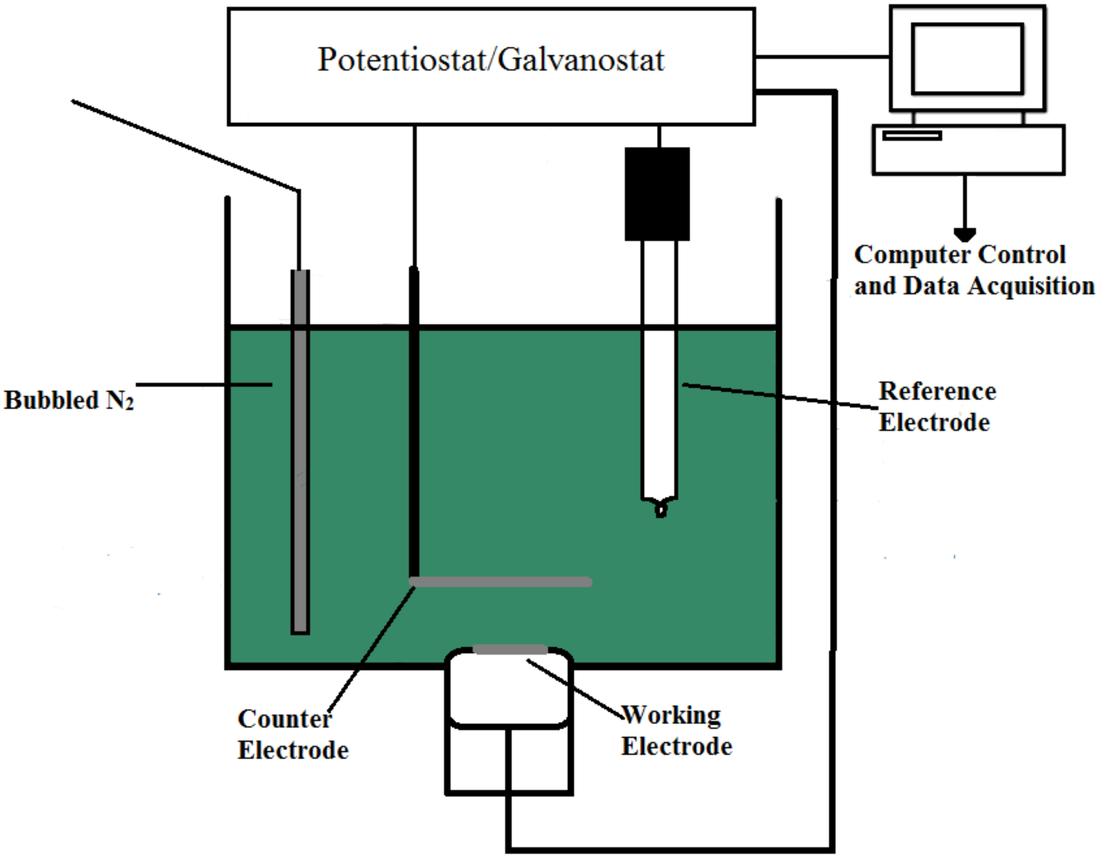

Figure 2.1: Schematic of a standard three-electrode cell.

The potential or current can be controlled by a potentiostat or galvanostat. During the electrodeposition process, current is passed between the working electrode and a counter (or auxiliary) electrode [3]. The counter electrode is placed facing the working electrode and is chosen so it does not interfere with the half reaction occurring at the working electrode surface. In addition, the counter electrode must be chosen carefully, so it does not produce any side products through an electrolysis reaction that can interfere with the reaction at the working electrode [3]. The applied potential at the working electrode is closely monitored by a reference electrode; consequently the reference electrode is located as close to the working electrode as possible to reduce the ohmic drop effect [3]. The potential of the working electrode is controlled relative to the reference electrode. The device used to measure the difference of the potential between the working electrode and the reference electrode is required to have high input impedance, so current is not drawn through the reference electrode [3]. Open circuit potential (OCP) is the potential of the working electrode relative to the reference electrode when no outside potential or current is being applied to the system. This potential remains constant. OCP is measured between the working electrode and reference electrode without connecting the counter electrode, thereby disabling the circuit created in the system [3]. The potentiostat circuit for the three-electrode cell is shown in figure 2.2.

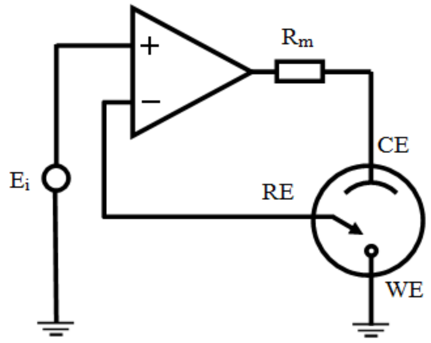

Figure 2.2: Potentiostat circuit for the three-electrode cell.

Metal ions in solution are discharged at the working electrode. The metal ions receive electrons and deposit onto the working electrode surface as metal atoms. The electrodeposition parameters including operating conditions and electrolyte composition influence the properties of the electrodeposited film including metal structure, crystallite size, morphology, and adhesion [4, 10-12, 17, 19-20, 22, 27-29, 31, 36-42]. It was concluded that many factors including the cathode current density, concentration of the ion containing the metal, agitation, temperature, pH, other cations and anions, complexation, inhibitors, and substrates also have an influence on the characteristics of deposits [4-38].

2.1.1 Electrolyte

The electrolyte is an ionic conductor, where chemical species containing the metal salts of interest are dissolved into a suitable solvent or brought to the liquid state to form a molten salt. The solvent is most often water; however, various organic compounds and other ionic liquids can also be used for the electroplating processes [1]. In the case of an electrodeposition of nickel, in an acidic plating, bath nickel is electrochemically deposited through Ni^{2+} ions while in an alkaline bath, nickel is deposited from a hydrated nickel cation species [6, 32-35]. Often metals are stabilized in solution as a metal complex prior to deposition. Nickel ions form various complex ions with citrate as a ligand in different pH ranges [6, 32-35].

In the electrolyte which contains positive charge of metal ions (cations), when an external electric field is applied, metal ions migrate to the cathode (negative pole) where they are discharged and eventually form a deposit as metal atoms on the surface.

$$M^{n+}_{(aq)} + ne^{-} \rightarrow M_{(s)} \qquad \text{Eq. (1.1)}$$

The reaction at the anode, where a noble metal (such as platinum or chromel) is used as the counter electrode, is oxidation of water.

$$2H_2O \rightarrow 4H^{+}_{(aq)} + O_{2(g)} + 4e^{-} \qquad \text{Eq. (1.2)}$$

The concentration of M^{n+} ions is decreased, while that of H^{+} ions is increased with time, which can eventually result in the increase of acidity of the solution.

In practice, electrodeposition from one metal component solution does not offer high quality coatings. Therefore, it is crucial to introduce some additional substances to enhance the properties of the deposits [1]. Adding or adjusting pH with an inorganic acid or base increases the electrical conductivity of the solution [1]. The increase in conductivity value of the electrolyte improves the uniformity of deposit thickness due to reducing the voltage, resulting in conservation of energy [1]. Acidic or alkaline solutions, which were adjusted by addition of acid or base, need to be stable or constant in pH throughout the entire depositing bath including around the electrode area [1]. Adding buffering agents in the plating solution is especially important when hydrogen evolves during the deposition process [1]. For example, boric acid is introduced in nickel plating baths to improve adhesion to the substrate due to increase current density which enhances the nucleation density of the deposit [44-51]. The increase of nucleation density on the surface is attributed to the adsorptive interaction of boric acid on the electrode surface [46]. Boric acid which acts as a surface agent or surfactant blocks the electrode surface from passivation [48]. Water electrolysis generated hydroxide ions and hydrogen gas resulting in the pH near the electrode surface increase, as the following reaction: $H_2O + M–H + e^- \rightarrow M + H_{2(ads)} + OH^-$. Boric acid is accordingly added to electrolyte to act as a buffer to avoid the local pH rise and prevent forming metal hydroxide species. This parallel hydrogen evolution reaction (HER) has strong influence on the morphological, structural properties, and decrease the overall process efficiency [44]. Nickel can eventually form nickel hydroxide precipitation at high pH [50]. Some other additives such as surfactants are introduced into the plating solution in order to reduce the energy at the electrode surface and prevent hydrogen bubbles from attaching to the substrate or deposit surface [52]. Consequently, the use of surfactants facilitates the removal of undesirable pitting, a microscopic point defect, resulting in improved uniform thickness and smooth surface of the deposits [1]. Additives can be brightening agents which produce bright metal deposits without polishing the surface after the deposition process [1]. Some coatings use leveling agents to smooth the surface and to seal the pre-existing pits from hydrogen evolution [1]. Additionally, there are many kinds of additives applied to the deposition bath to improve the properties of the coatings by decreasing internal stresses in the deposits, increasing current efficiency, activating anode dissolution, and suppressing dendrite formation [1]. However, adding additives in the plating bath inhibits the deposition role of the metal. Hence, it is suggested that the additive's concentration be limited to 10^{-2} moles per liter [1].

2.1.2 Electrode Processes. Faraday's Law [1, 3]

The electrochemical process occurs at the interface between the metal and solution. Metal ions dissolved in aqueous solution may form a complex species and take part in the charge transfer process which is consequently called the electroactive species.

The simplest case of metal ion discharge is explained as a simple metal ion. The reaction in this case is as follows:

$$M^{n+}_{(aq)} + ne^{-} \rightarrow M_{(s)} \qquad \text{Eq. (1.3)}$$

The amount of electrons (n), equal to a charge of metal ion (n+), need to be transferred for the deposition of one atom of metal. The formation of one mole of the metal requires coulombs of electricity:

$$Q = nF \qquad \text{Eq. (1.4)}$$

$$m = \left(\frac{Q}{F}\right) M \qquad \text{Eq. (1.5)}$$

where:

Q is the net charge passed through the circuit (coulombs),
F is Faraday's constant of 96485 coulombs per mole,
n is the number of electrons in reaction (moles),
M is the molar mass of the metal (grams/mole), and
m is the deposited metal mass (grams).

The total charge (Q) accumulated onto an electrode in term of an electric current is equal to the integration of the electric current, $i(\tau)$, over time (τ).

$$Q = \int_0^t i(\tau) d\tau \qquad \text{Eq. (1.6)}$$

where:

i is the current,
τ is the corresponding time, and
t is the duration of electrodeposition.

The quantity of the deposit has the residence time on the surface equal to some certain τ.

These three equations are important and commonly applied to calculate the amount of metal deposited during electrodeposition. The thickness of the electrodeposited film on the substrate can be determined by the duration of the plating. It is necessary to know the metal density, plating efficiency, and the coating substrate area to determine film thickness. In general, the longer the plating time of the substrate in the plating bath, the thicker the resulting electrodeposited film [1]**.** Typical layer thicknesses vary from 0.1 to 30 microns [1].

The electrode surface is the region at which the electrochemical process of interest is occurring. It can be a cathode where a reduction occurs or the anode where oxidation occurs [1]. Electrode potential is another physical variable, along with current density, controlling the electrode process. The potential of the electrode is the potential drop between the solution and the bulk of the metal. This quantity cannot be measured experimentally since the solution cannot be defined operationally without introducing an additional metal/electrolyte interface, and therefore cannot be used as a reference point. For this reason it is conventional to measure the electrodeposited potential compared with the reference potential resulting in applying a constant, reproducible and stable potential [1]. Current density and electrode potentials of any given electrode reaction at steady state are related to each other through a one-to-one correspondence; however, actual conditions at an electrode where a growth process is occurring are rarely stationary. For this reason a potentiostatic process is where the metal is electrochemically fabricated at a constant potential (E= constant) with current density changing over time whereas a galvanostatic process is where electrodeposition is performed at a constant current (i= constant) accompanied by variations of potential. The potential or current density applied to the electrode results in changes to the surface state (roughness and morphology) evolving with time. In addition, the composition of the solution adjacent to the electrode (concentration of chemical species and local pH) can change during the process [1].

2.1.3 The Influence of Deposition Parameters on Microstructure of Growing Metal Surface

It has long been recognized that the microstructure of the deposits are significantly influenced by the deposition parameters, which consequently affect the film properties [1, 59]. Electrodeposition is initiated with the nucleation of stable metal clusters, followed by propagation of metal growth. This is progressed by attachment of atoms to the lattice across the whole surface. The ions adding to the cluster at a given potential are in equilibrium with the solution. From this equilibrium process, the overall displacement of the boundary-solution along such a normal process is called normal growth. The quality of the surface morphology is mainly determined by the surface growth stability during motion of the phase boundary. The growth of the crystal is associated with the rate of nucleation [1]. In general, it is agreed that at high rate of nucleation and slow propagation growth of metal, that fine-grained deposits are formed, and vice-versa [1]. This behavior was exhibited from electrochemically fabricating nanocrystalline films. It was shown that current density plays an important role on the grain size of electrodeposited coatings [53-61]. It was also supported that electrodepositing at high current densities promoted the grain refinement of the deposits [59]. The amplification of current density results in raising the overpotential, which is associated with an increase of nucleation rate and enhanced cluster density [1].

2.2 Experimental Techniques

An EG&G PAR Potentiostat/Galvanostat Model 273A was used for all electrodeposition and cyclic voltammetry.

2.2.1 Particle Sizing

Dynamic light scattering (DLS) can be named as photon correlation spectroscopy or quasi elastic light scattering [62]. The particle size can be determined down to 1 nm diameter. It allows measuring wide range of applications including emulsion, micelles, protein, polymers, and nanoparticle colloids. A laser beam is used to illuminate the sample and a fast photon detector is used to detect the scattering light fluctuation at a known scattering angle (θ). A simple DLS instruments allows determining the mean particle size in a limited size range with a fixed angle, while the more complicated multi angle instruments can measure the full particle size distribution.

The particle which has ability to suspend in the solution are in Brownian movement due to random collision with solvent molecules resulting to the particles diffuse through the liquid media [62]. The diffusion coefficient (D) is inversely proportional to the particle's radius (R) according to Stroke-Einstein equation [62].

$$D = \frac{kT}{6\pi R\eta} \qquad \text{Eq. (1.7)}$$

where:

k is the Boltzmann constant,
T is the temperature, and
η is the viscosity

According to this equation, it is shown that when particle size is large, diffusion coefficient is small, hence, the particle moves slowly. In contrast, a small particle moves rapidly as a result of the larger diffusion coefficient. In dynamic light scattering, the fluctuations in time of scattered light from the particles in Brownian movement are determined after dynamic light scattering. The light which is scattered in all directions is collected within a scattering volume which is defined by the scattering angle and detection apertures. Because the particles are moving, the relative positions of the particles changing in time, consequently, fluctuation in time of the scattered light intensity is monitored. The Brownian movement of the particle travel randomly leads to the scattered intensity fluctuates randomly. The fluctuation for the small particle changes faster while the lager particle shows slow fluctuation due to the slow moving particle. The fluctuations of the scattered light are analyzed using the autocorrelation function.

2.2.2 Zetapotential Measurment

Zetapotential was determined by electrophoretic light scattering [62]. Zetapotential is used as the index of the surface charge of the particle. It represented the stability of the dispersing particle in solution. The Brownian movement of the particle in liquid solution is influenced by the ions in the Stern layer where the ions strongly attached near to the particle surface and part of the diffusion layer (Figure 2.3) [62]. The layer outside the Stern layer is called diffusion layer. The electric field that influences the particle to move is at the slipping plane. Zetapotential is the electric potential in the interfacial double layer (Stern and diffusion layers) of the particle or potential difference between dispersion medium and the stationary layer of the fluid attached to the dispersed particle [62]. If zeta potential is high, the particles have stability to suspend in the dispersion fluid due to high electrostatic repulsion between particles [62]. In contrast, having low zeta potential value approaching to zero, the particles have more probability to collide result in increased forming particle aggregation.

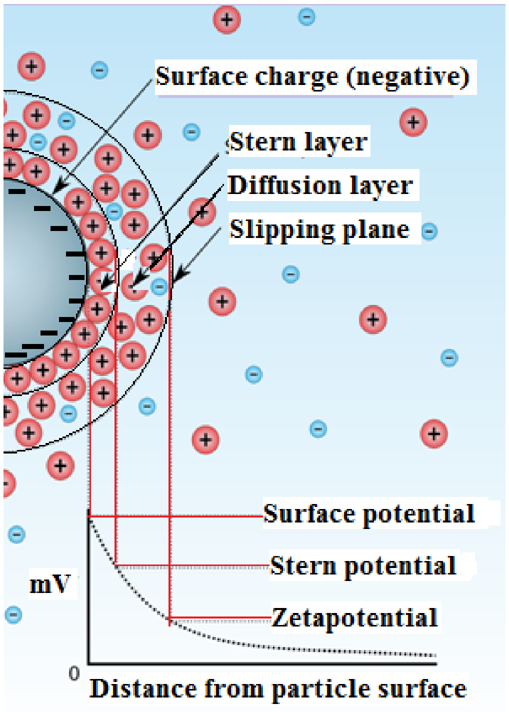

Figure 2.3: Concept of Zetapotential [62].

For the measurement of the zetapotential, layered silicate particles have an electrical charge on their surface when dispersed in the solution. When electric field is applied to the cell containing particle suspension, the charge particles move toward the electrode which has an opposite charge. While the particle movement, electroosmotic flow close to the wall of the cell moves toward the opposite electrode due to the surface charge on the cell wall as shown in figure 2.4 (left). Electroosmotic flow is the motion of liquid induced by an applied potential across a capillary tube. The electroosmotic flow moves until hitting to the cell wall then flows back to the center of the cell. When the zetapotential is measured, the evident mobility of the particles is observed from the summation of the particle true mobility and the electroosmotic flow which appear opposite direction.

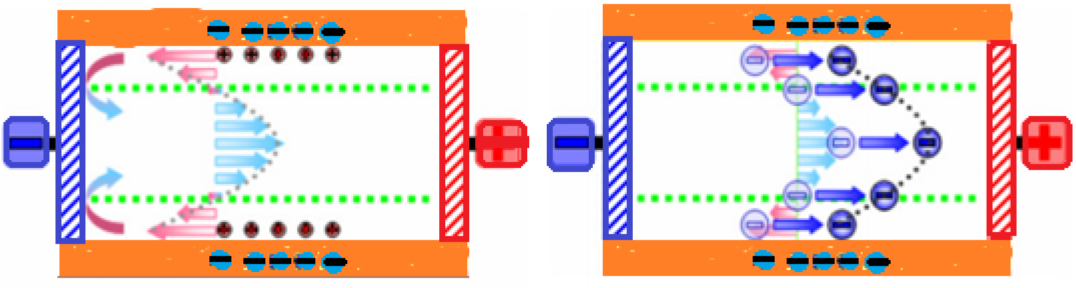

Figure 2.4: Schematic diagram of the electroosmotic flow occurring in a close cell [62].

The flow in the cell has a symmetric parabolic profile when the concentration of the particle is homogenoues. The equivalent elctrical charges of the upper and lower surface of the cell leads to the symetric parabolic flow as shown in figure 2.4 (right). However, asymmetric electroosmotic flow due to a difference in the charges of the upper and lower cell surfaces occurs when the dispersed particles aggregates.

2.2.3 Solution Studies

The solutions prepared for measurement of kinematic viscosity, zeta potential, particle size, and conductivity consisted of the exfoliated MMT solutions and the nickel-citrate plating solution. The zeta potential of the various plating solutions were measured using a Delsa Nano-C (Beckman-Coulter Instruments). The size of the particles in the solution was determined by photon correlation spectroscopy using the Delsa Nano-C [62]. The samples were allowed to equilibrate at 25^{o}C for 60 seconds using a peltier device in the instrument. The samples were measured for zeta potential three times to show reproducibility of the measurement. Kinematic viscosity (cSt) was measured with a Cannon Ubbelohde viscometer size 50 and 100. The viscometer with 20mL of sample was placed into a Brinkmann RM6 water bath at 25^{o}C and allowed to equilibrate for 20 minutes. The flow time was measured in seconds and multiplied by the kinematic viscosity constant (cSt/s).

Each sample was measured five times to show reproducibility. The conductivity was measured with a Thermo Orion 550A conductivity meter.

2.2.4 Characterization Techniques

The surface morphology of the films was characterized with an Environmental FEI Quanta 200 scanning electron microscope (SEM). X-ray diffraction data was obtained on a Siemens D-500 Diffractometer using Cu Kα radiation (λ = 0.1541 nm) at 35 kV and 24 mA. The scans were run from 2–100^{o} 2θ at a step size of 0.05 degrees and dwell time of 1 second.

The particle size was estimated from the XRD patterns using the Scherrer formula:

$$L = \frac{k\lambda}{\beta_r cos\theta} \qquad \text{Eq. (1.8)}$$

The Williamson-Hall plot is a plot of $\beta_r\cos\theta$ versus $\sin\theta$ which yielded a straight line with a slope of η and intercept of $k\lambda/L$ [63, 64]. The crystallite size given by Scherrer equation are: where λ is the wavelength of the x-rays, θ is the diffraction angle, L is the crystallite size, k is a constant (0.94 for Gaussian line profiles and small cubic crystals of uniform size) and βr (in radians) is the corrected full width at half maximum of the peak given by:

$$\beta_r^2 = \beta_m^2 - \beta_s^2 \qquad \text{Eq. (1.9)}$$

where β_m is the experimental measured width at half maximum and β_s is the corresponding value of a silicon powder standard with peaks corresponding to the same two theta region [65]. This equation is used to correct for instrumental broadening, when the observed peaks have a near-Gaussian shape.

The preferred crystalline orientation of Ni was examined by X-ray diffraction (XRD) techniques utilizing a Miniflex II X-ray diffractometer, Rigaku Corporation, Japan. The measurement was carried out using 30 kV voltage, 15 mA current, 0.3 mm receiving slit, scintillation counter detector and Cu-kα radiation (0.1541 nm). To examine the preferred crystalline orientation, the term relative texture coefficient is used [66]. It can be defined as:

$$RTC_{(hkl)} = \frac{I_{s(hkl)}/I_{p(hkl)}}{\sum_{i=1}^{n} I_{s(hkl)}/I_{p(hkl)}} \times 100\% \qquad \text{Eq. (1.10)}$$

where Is(hkl) and Ip(hkl) are the diffraction intensities of the (hkl) plane as measured from X-ray diffraction of the composite and the standard Ni powder, respectively. $RTC_{(hkl)}$ expresses the percentage of the relative intensity of a given orientation (hkl) to the whole crystallographic orientations.

The microstructure of the coatings was studied by scanning electron microscopy (SEM) and recorded with a Nova NanoSEM 450 FEI company, Netherlands. The amount of MMT incorporated in the nickel matrix was evaluated using energy dispersive X-ray spectroscopy (EDX). The surface topography and heterogeneities of Ni and Ni-MMT samples was examined by atomic force microscopy (AFM). Measurements were performed under ambient conditions using the standard topography AC air (tapping mode in air). An AFM head scanner applied with Si cantilever adjacent vertically in the sample resonant frequency of the free-oscillating cantilever set as the driving frequency.

Flame atomic absorption spectroscopy (AAS) was used to determine the metal composition of the coatings. The nickel-molybdenum alloy coatings were electrodeposited from different $[MoO_4^{2-}]/[Ni^{2+}]$ molar ratio of 0.1 and 0.2. The coatings were dissolved in 1% HNO_3 and diluted to 250 mL until its absorbance was in the working range of the calibration. The standard calibration method was used to determine the Ni and Mo concentration in the coatings. The standard nickel and molybdenum concentration were in range of 20 to 80 and 10 to 50 mg/L, respectively. The working conditions for measuring Ni and Mo are shown in table 2.1.

Table 2.1: AAS calibration of nickel and molybdenum

	Ni	Mo
Lamp current (mA)	4 mA	7 mA
Wavelength	352.4 nm	320.9 nm
Slit Width	0.5	0.2 nm
Fuel	Acetylene	Acetylene
Support	Air	Nitrous oxide

Table 2.2: AAS calibration and measurement of nickel and molybdenum

Metal	Films coated from $[MoO_4^{2-}]/[Ni^{2+}]$ molar ratio	Equations and R^2 values	Metal absorption (Abs)	Metal in coatings (%)
Ni	0.1	$y = 0.0048x + 0.0245$ $R^2 = 0.9999$	0.408	79.90
Mo	0.1	$y = 0.0043x + 0.0341$ $R^2 = 0.9998$	0.118	19.51
Ni	0.2	$y = 0.0048x + 0.0245$ $R^2 = 0.9999$	0.341	65.94
Mo	0.2	$y = 0.0043x + 0.0341$ $R^2 = 0.9998$	0.181	34.16

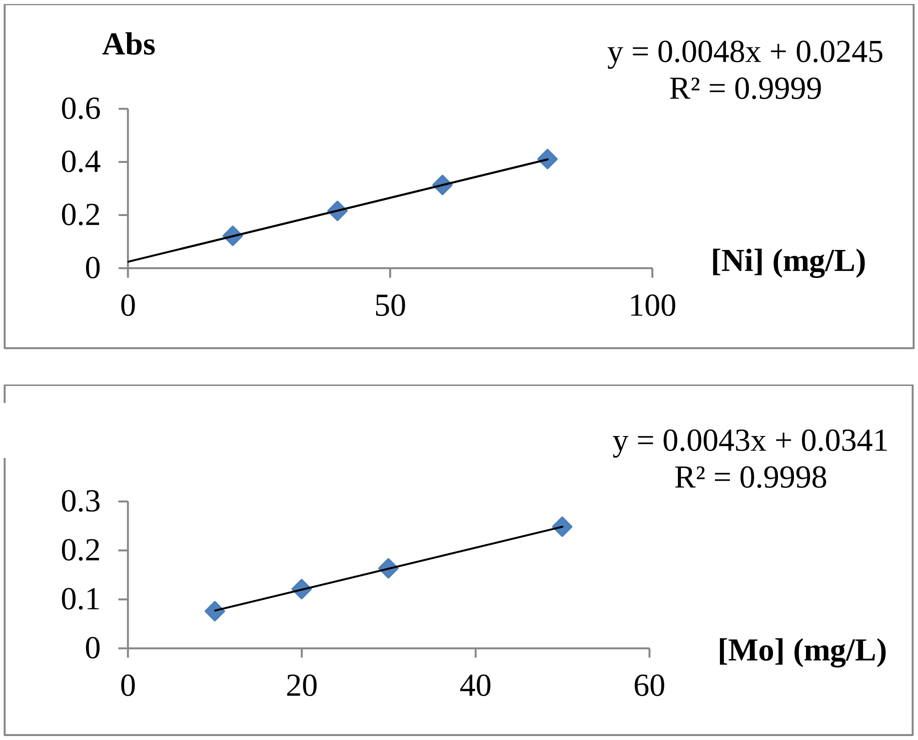

Figure 2.5: Calibration curve of nickel and molybdenum

2.3 Chapter References

[1] Y.D. Gamburg, G. Zangari, *Theory and Practice of Metal Electrodeposition*, Springer Science Business Media: New York, 2011.

[2] A.M. Rashidi, A. Amadeh, Surface and Coatings Technology. 2008, 202(16), 3772-3776.

[3] A.J. Bard, L.R. Faulkner, *Electrochemical methods: fundamentals and Aaplications*, 2nd Ed., John Wiley & Sons, Inc.:New York, 1944.

[4] R. Abdel-Karim, A.F. Waheed, Chapter6:Nanocoatings, Modern Surface Engineering Treatments, Intech, 1-157, http://cdn.intechopen.com/pdfs-wm/44877.pdf, May 22, 2013.

[5] E.S. Güler, E. Konca, İ. Karakaya, *Int. J. Electrochem. Sci.* **2013**, 8, 5496 – 5505.

[6] J. Tientong, C.R. Thurber, N.A. D'Souza, A. Mohamed, T.D. Golden, *International Journal of Electrochemistry*, **2013**, 1-8.

[7] J. Tientong, Y.H. Ahmad, M. Nar, N. D'Souza, A.M.A. Mohamed, T.D. Golden, *Materials Chemistry and Physics*. **2014**, 145, 44-50.

[8] Y.H. Ahmad, J. Tientong, N.A. D'Souza, T.D. Golden, A.M.A. Mohamed, *Surface & Coatings Technology*. **2014**, 242, 170–176.

[9] A. Butts, V.D. Nora, *J. Electrochem. Soc.* **1941**, 79(1), 163-185.

[10] M. Hakamada, Y. Nakamoto, H. Matsumoto, H. Iwasaki, Y. Chen, H. Kusuda, M. Mabuchi, *Materials Science and Engineering: A*. **2007**, 457(1–2), 120-126.

[11] D.T. Read, Y.W Cheng, R. Geiss, *Microelectronic Engineering*. **2004**, 75(1), 63-70.

[12] M. Donten, H. Cesiulis, Z. Stojek, *Electrochimica Acta*. **2005**, 50(6), 1405-1412.

[13] L.S. Sanches, S.H. Domingues, C.E.B. Marino, L.H. Mascaro, *Electrochemistry Communications*. **2004**, 6(6), 543-548.

[14] Y. Zeng, Z. Li, M. Ma, S. Zhou, *Electrochemistry Communications.* **2000**, 2(1), 36-38.

[15] D. Nikolova, R. Edreva-Kardjieva, M. Giurginca, A. Meghea, J. Vakros, G.A. Voyiatzis, Ch. Kordulis, *Vibrational Spectroscopy*. **2007**, 44(2), 343-350.

[16] A. Marlot, P. Kern, D. Landolt, *Electrochimica Acta.* **2002**, 48(1), 29-36.

[17] I. Gurrappa , L. Binder, *Sci. Technol. Adv. Mater.* **2008**, 9(4), 1-11.

[18] E. Beltowska-Lehman, *Surface and Coatings Technology.* **2002**, 151–152, 440-443.

[19] Q. Han, S. Cui, N. Pu, J. Chen, K. Liu, X. Wei, *International Journal of Hydrogen Energy.* **2010**, 35(11), 5194-5201.

[20] K. Hashimoto, T. Sasaki, S. Meguro, K. Asami, *Materials Science and Engineering: A.* **2004**, 375–377, 942–945.

[21] L.S. Sanches, C.B. Marino, L.H. Mascaro, *Journal of Alloys and Compounds.* **2007**, 439(1–2), 342-345.

[22] M.H. Allahyarzadeh, B. Roozbehani, A. Ashrafi, S.R. Shadizadeh, *Surface and Coatings Technology*. **2011**, 206(1), 137-142.

[23] E. Beltowska-Lehman, P. Indyka, *Thin Solid Films.* **2012**, 520(6), 2046-2051.

[24] A.G. Dolati, M. Ghorbani, A. Afshar, *Surface and Coatings Technology.* **2003**, 166(2–3), 105-110.

[25] E. Gómez, E. Pellicer, E. Vallés, *Electrochemistry Communications.* **2005**, 7(3), 275-281.

[26] M.P. Zach, K.H. Ng, R.M. Penner, *Science.* **2000**, 290, 2120-2123.

[27] H. Alimadadi, M. Ahmadi, M. Aliofkhazraei, S.R. Younesi, *Materials & Design*, **2009**, 30(4), 1356-1361.

[28] P. Gyftou, E.A. Pavlatou, N. Spyrellis, *Applied Surface Science.* **2008**, 254(18), 5910-5916.

[29] T. Ohgai, Y. Tanaka, R. Washio, *J Solid State Electrochem.* **2013**, 17, 743–750.

[30] S. Rode, C. Henninot, M. Matlosz, *Journal of The Electrochemical Society*, **2005**, 152(4), C248-C254.

[31] H. A. Conrad, J. R. Corbett, and T. D. Golden, *Journal of the Electrochemical Society.* **2012**, 159(1), C29–C32.

[32] T. A. Green, A. E. Russell, and S. Roy, *Journal of the Electrochemical Society.* **1998**, 145(3), 875–881.

[33] C.-Q. Li, X.-H. Li, Z.-X.Wang, and H.-J.Guo, *Transactions of Nonferrous Metals Society of China*. **2007**, 17(6), 1300–1306.

[34] O. Y. Zelenin, *Russian Journal of Coordination Chemistry.* **2007**, 33(5), 346–350.

[35] S. Rode, C. Henninot, and M. Matlosz, "Complexation chemistry in nickel and copper-nickel alloy plating from citrate baths," *Journal of the Electrochemical Society.* **2005**, 152(4), C248–C254.

[36] Y. Xuetao, W. Yu, S. Dongbai, and Y. Hongying, *Surface and Coatings Technology.* **2008**, 202(9), 1895–1903.

[37] E. M. Hofer, H. E. Hintermann, *J. Electrochem. Soc.***1965**, 112(2), 167-173.

[38] A. Ibañez, E. Fatás, *Surface and Coatings Technology.* **2005**,191(1), 7-16.

[39] G. Fu, Z. Hu, L. Xie, X. Jin, Yu. Xie, Y. Wang, Z. Zhang, Y. Yang, H. Wu, *Int. J. Electrochem. Sci.* **2009**, 4, 1052-1062.

[40] D. D. Zhao, W. J. Zhou, H. L. Li, *Chem. Mater.*, **2007**, 19, 3882.
[41] G. S. Attard, P. N. Bartlett, N. R. B. Coleman, J. M. Elliott, J. R. Owen, J. H. Wang, *Science*. **1997**, 278, 838.

[42] P. A. Nelson, J. M. Elliott, G. S. Attard, J. R. Owen, *Chem. Mater*. **2002**, 14, 524.

[43] Y. Tan, S. Srinivasan, K. S. Choi, *J. Am. Chem. Soc*. **2005**, 127, 3596.
[44] J.S. Santos, R. Matos, F. Trivinho-Strixino, E.C. Pereira, *Electrochimica Acta*. **2007**, 53(2), 644-649.

[45] C. Karwas, T. Hepel, *J. Electrochem. Soc.*, **1988**, 135(4), 839-844.

[46] C. Karwas, T. Hepel, J. Electrochem. Soc. **1989**, 136(6), 1672-1678.

[47] N. Zech, D. Landolt, *Electrochimica Acta.* **2000**, 45(21), 3461-3471.

[48] K.-M. Yin, B.-T. Lin, *Surface and Coatings Technology.* **1996**, 78(1-3), 205-210.

[49] Y. Wu, D. Chang, D. Kim, S.-C. Kwon, *Surface and Coatings Technology*, **2003**, 173(2-3), 259-264.

[50] L. Marder, E.M.O. Navarro, V. Pérez-Herranz, A.M. Bernardes, J. Z. Ferreira, *Desalination*. **2009**, 249(1), 348-352.

[51] M. Sˇupicova´, R. Rozik, L. Trnkova´ , Orinˇa´kova´, M. Ga´lov, *J. Solid State Electrochem*. **2006**, 10, 61-68.

[52] E. S. Güler, E. Konca, İ. Karakaya, *Int. J. Electrochem. Sci.* **2013**, 8, 5496-5505.

[53] R. Winand, *Electrochimica Acta.* **1994**, 8-9, 1091-1105.

[54] L. Wang, Y. Gao, T. Xu, Q. Xue, *Mater. Chem. Phys.* **2006**, 99, 96.

[55] A.M. El-Sherik, U. Erb, *J. Mater. Sci.* **1995**, 30, 5743.

[56] R. Winand, *Electrochim. Acta*. **1994**, 39 1091.

[57] R. Winand, *J. Appl. Electrochem.* **1991**, 21, 377.

[58] I. Bakony, E. Tóth-Kádár, L. pogány, Á. Cziráki, I. Gerőcs, K. Varga-Josepovits, B. Arnold, K. Wetig, *Surf. Coat. Tech.***1996,** 78 124.

[59] A.M. Rashidi, A. Amadeh, *Surface and Coatings Technology*. **2008**, 202(16), 3772–3776.

[60] R. Winand, *Electrochim. Acta.* **1998**, 43, 2925.

[61] L. Qin, J. Lian, Q. Jiang, *Transactions of Nonferrous Metals Society of China*. **2010**, 20(1), 82-89.

[62] User’s Manual: Delsa™Nano Submicron Particle Size and Zeta Potentia, Beckman Coulter, Inc., PN A54412AC, May 2011.

[63] F.A. Marinho, F.S.M. Santana, A.L.S. Vasoconcelos, R.A.C. Santana, S. Prasad, *J. Brazil. Chem. Soc.* **2002**, 13, 522.

[64] T. Sato, H. Takahashi, E. Matsubara, A. Muramatsu, Mater. *Trans. A.* **2002**, 43, 1525.

[65] Y. Zeng, L. Zelin, M. Ming, Z. Shaomin, *Eletrochem. Commun*. **2000**, 2, 36.

[66] A. Gomes, I. Pereira, B. Fernandez, R. Pereiro, *Electrodeposition of metal matrix nanocomposites: improvement of the chemical characterization techniques*. InTech: 2011.

CHAPTER 3

REINFORCED MATERIAL COATINGS

3.1 Composite Coatings

Composites contain at least two main types of components: matrix component and reinforcement component [1]. The purpose of incorporating reinforcement materials into matrix materials is to introduce special physical or mechanical properties into the matrix [2, 3]. Matrix materials or matrices typically surround and hold the reinforcement materials by conserving their relative positions [2, 3]. The combination of beneficial properties that the composite gains from the individual materials used enhances the mechanical strength over the individual components' properties [2, 3]. Composites provide the attributes of matrix materials combined with the strengthening properties of reinforcement materials which allow one to choose an optimum combination for the application of interest [1-3]. The fabrication of composite materials has been of increasing interest due to the discovery of improved mechanical strength. It is important to understand the relationship between structures and properties of their reinforcement materials [2, 3]. Additionally, the surface area to volume ratio of the reinforcement employed in the matrices is also vital for optimal content [2, 3]. According to engineering applications, composite materials can be classified into the following four categories [3]:

- Composite construction materials such as cement and concrete [2].
- Reinforced plastics such as fiber-reinforced polymer, glass-reinforced plastic [3].
- Metal composites such as metal fibers reinforcing other metals [3]
- Ceramic composites such as ceramic matrix composites, including bone (hydroxyapatite reinforced with collagen fibers) and cermet (combination of ceramic and metal) [1]. The ceramic matrix composites are fabricated principally for increased fracture toughness, not for improved strength.

3.2 Nanocomposites

Nanocomposite materials or nanocomposites are composite materials which contain at least one component that exhibits at least one dimension in the nanometer scale [4]. Nanocomposites are being examined as alternative prospects to overcome limitations of microcomposite and monolithic materials. It has been reported that change in particle size to nanometer level lead to dramatic improvement in interactions at phase interfaces [4]. For this reason nanoparticle incorporation is being examined to improve material properties by reinforcing matrix materials with nanoparticles. Nanocomposites can be classified as shown in table 3.1 into three categories: metal, ceramic, and polymer.

Table 3.1: Categories of nanocomposites [4].

Class	Examples
Metal	Fe-Cr/Al_2O_3, Ni/Al_2O_3, Fe/MgO, Al/CNT, Co/Cr, Mg/CNT
Ceramic	Al_2O_3/SiO_2, SiO_2/Ni, Al_2O_3/TiO_2, Al_2O_3/SiC, Al_2O_3/CNT
Polymer	Polymer/layered silicates, polyester/ TiO_2, Thermoplastic/thermoset polymer, polymer/layered double hydroxides, polymer/CNT

Note: CNT is abbreviation for carbon nanotubes.

3.2.1 Reinforcement Materials

Reinforcement materials are commonly incorporated into matrix materials to enhance physical and mechanical properties [3]. Reinforcement, which strengthens matrices, is predominantly rigid and proficient at blocking crack propagation. Incorporating nanometer-sized particles into matrices improves the material by homogenously dispersing into the matrix; satisfactorily attaching to the matrix results in overall uniform coverage of the nanocomposites [3].

3.2.2 Ceramic Reinforced Metal Nanocomposites

Metals or metal alloys are ductile [4]. Ceramics appear remarkably brittle; provide good wear resistance, and have high thermal and chemical stability [4]. In order to overcome the limited strength of metals, metal matrix nanocomposites are frequently fabricated [39]. The composites combine metal and ceramic properties, i.e., ductility and toughness with high strength and modulus [4]. Thus the composites with high strength are able to withstand shear or compression processes and elevated service temperature fields [4]. They offer extraordinary potential for many applications, such as automotive industries and aerospace [3,4,14,37]. The examples of some heterogeneous reinforcing metal matrix nanocomposites and their properties are shown in table 3.2 [4].

Table 3.2: Ceramic-reinforced metal nanocomposites and their properties.

Matrix/Reinforcement	Properties	Material Processing
α-Fe/$Fe_{23}C_6$/Fe_3B [5]	-Drastic increased hardness -Increased heat treatment temperature	Melt infiltration
Cu/Al_2O_3 [6]	Enhanced microhardness	Mechanical milling method
Al/SiC [7]	Increased hardness and elastic modulus	Powder metallurgy technique
Al/AlN [8]	Increased compression resistance and low strain rate	Mechanical alloying and double pressing by sintering route
Ni/PSZ (partially stabilized zirconia) and Ni/YSZ (Y_2O_3-stabilised ZrO_2) [9]	Enhanced hardness and strength	Solution combustion process
Cu/WC [10]	Increased hardness	Powder metallurgy techniques by milling and mechanical synthesis
Ni/ZrO_2 [11]	Improved hardness	Electrodeposition
Ni/AZY (alumina yttria doped cubic zirconia) [12]	Superior wear resistance and corrosion resistance and improved microhardness	Electrodeposition
Ni–SiC [13]	Increased microhardness and wear and corrosion resistance	Electrodeposition
Ni/CeO_2 [14, 38]	Improved microhardness, thermal stability, and corrosion resistance	Electrodeposition
Ni/ Al_2O_3 [15]	Increased hardness	Electrodeposition

Most of the metal matrix nanocomposites are fabricated by common techniques including electrodeposition, spray pyrolysis, vapor techniques, solidification, liquid metal infiltration, and chemical methods (colloidal and sol-gel processes) [4,21].

In this work, the focus is to reinforce metal and metal alloys, specifically nickel and nickel-molybdenum alloys, with ceramic nanoparticles through electrochemical deposition technique to enhance mechanical strength and corrosion resistance. Metal-ceramic nanocomposites are of interest because they offer properties of both ceramic and metal materials resulting in improved hardness, elastic modulus, heat stability, and corrosion resistance [4-16]. The incorporation of ceramic particles into metal alloys improves strength heat stability and corrosion resistance [5-41].

In 1963, Sautter electrochemically deposited nickel incorporated with alumina (Al_2O_3) powders to enhance mechanical strength [17]. Since then the electrochemical synthesis of cermet has been developed by reinforcing metal matrices with several kinds of the ceramic particles. Some of the ceramics include α-Al_2O_3, TiO_2, SiC, TiC, WC, TaC, ZrC, ZrO_2, ZrB_2, Si_3N_4, graphite, and diamond [18,24]. The composites have been formed electrochemically with nickel [9,11-15,19]. Nickel-zirconium oxide layers were electrophoretically deposited and then sintered at 1150 and 1050 ^{o}C for 3 h providing a strong adhesion of the thin film (5-10 μm) onto the stainless steel substrate [19]. The nickel- zirconium oxide film is an example of the advantage of incorporating a ceramic into a metal matrix.

Superalloys have superior strength and sufficient tolerance to oxidation in high temperature environments. They commonly contain a minimum 40% nickel content with other refractory elements including molybdenum, tungsten, titanium, and niobium [33,34]. Aluminum-titanium alloys are graded as age-harden types. The addition of a small amount of boron and zirconium helps improve high-temperature resistance. Some silicide compounds such as molybdenum silicide ($MoSi_2$) and silicon carbide (SiC) or aluminide compounds such as NiAl are able to develop a protective scale so that they resist to high temperature over 1200 K [34-35]. Silicon, when incorporated in nickel-based alloys, improves hardness resulting in good abrasion and wear resistance. Incorporation of various metal oxides such as SiO_2, Al_2O_3, and Fe_3O_4 by several methods including spin coating, spraying, and sol-gel improved thermal stability and mechanical strength of the composites [6,15,32].

Tungsten carbide (WC) particles are electrochemically codeposited with nickel or copper by sediment codeposition compared to conventional electrodeposition [10,24-30]. The solution was stirred to promote the incorporation of the particles. The increase of current density leads to promotion of incorporation of WC in the nickel metal film. The percentage of WC incorporated into the nickel film synthesized by sediment codeposition increased over that provided by the conventional electrodeposition.

3.3 Layered Silicate Nanoparticles

Clay minerals are composed of hydrous aluminum silicate structures and are classified as phyllosilicates [41]. Clay minerals have been extensively used to improve nanocomposite properties because they form naturally, are abundant, and inexpensive. Montmorillonite clay, a layered silicate, is widely used in various applications in industry due to its high degree of swelling ability, high cation exchange capacity, and high surface area [41]. Montmorillonite is classified as a smectite mineral containing a 2:1 layered structure of two tetrahedral silicate sheets sandwiching one octahedral aluminate sheet [41]. The tetrahedral sheets are bonded to the octahedral sheet by sharing of apical oxygens. Silicon is the main atom located in the middle of the tetrahedral structure, while mainly aluminum atoms occupy the central octahedral site (Figure 4.1). Montmorillonite is a hydrous aluminum silicate with approximate formula of (Na,Ca)(Al,

$Mg)_6(Si_4O_{10})_{3-}(OH)_6 \cdot nH_2O$ [41]. The Al(III) and Si(IV) atoms located in the octahedral and tetrahedral structure can be substituted by lower valent atoms such as Mg(II), causing an excess of electrons on the layered silicate structure. The insertion of sodium ions (Na^+) into the interlayer improves the hydrophilic property of the clay. Sodium ions promote water penetration leading to a greater degree of water swelling. The degree of hydration depends on many factors such as the interlayer cations or element composition of the layers [42,45-46]. The species incorporated in the interlayer such as sodium ions are referred to as intercalants, while the other species that exchange with the intercalants are called intercalated dispersions [42,44]. Once montmorillonite is exfoliated as an individual layer, each layered silicate platelet has a thickness of 10 nm, called a nanoclay or nanoparticle [41]. The size of an exfoliated layered silicate sheet can be large, up to 2 microns in length [41]. Due to the layered silicate structure containing silicate and aluminate sheets, it is an attractive option to reinforce the metal matrix materials due to increased stiffness with their incorporation. In addition, exfoliated montmorillonite has large surface area up to 760 x 10^3 m^2/kg, which enhances the composite performance with low loading content [4, 43].

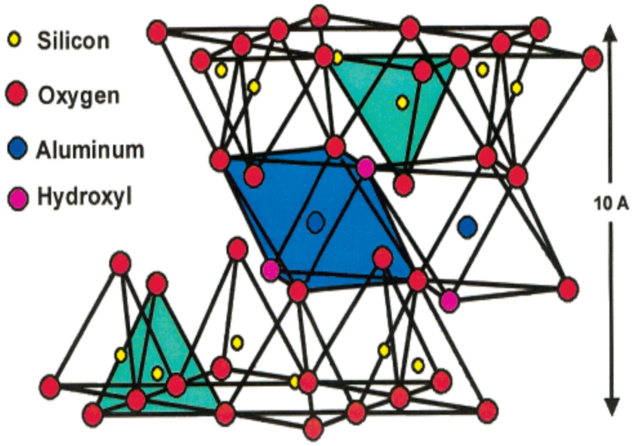

Figure 3.1: Cross-sectional model of the montmorillonite layered silicate structure.

The bonding between each layer of the layered silicate is quite weak, mainly held together through van der Waals forces. Sodium ions are intercalated in the interlayer which is the space between the layered silicate sheets (Figure 3.2, left) [41]. When water molecules penetrate the interlayer, the clay swells. Water molecules widen the space between the layered silicate sheets until sufficient attraction between each silicate layer used to maintain uniformity no longer exists, destroying the order of the layers. Then the layered silicates are exfoliated (Figure 3.2, right). The layered silicate sheets are separated as individual sheets freely suspended in the solution as shown in figure 3.3.

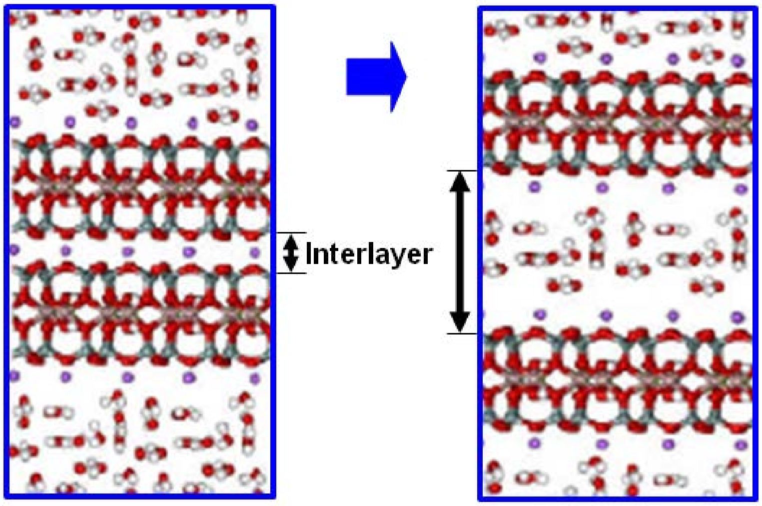

Figure 3.2: A typical platelet arrangement (left), the exfoliated layered silicate platelet (right).

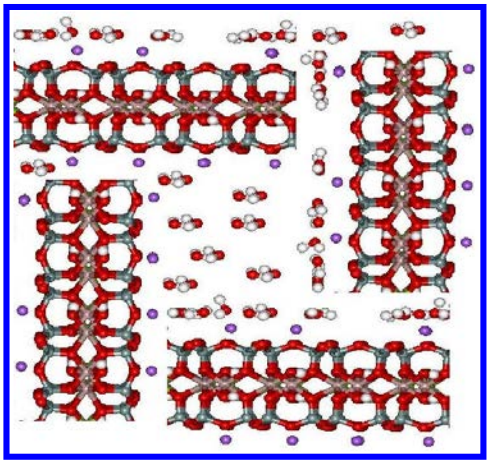

Figure 3.3: The individually suspended exfoliated layered silicate platelets.

The introduction of an interlayer to the montmorillonite with sodium ions consequently improves solubility of the clay. The hydrophilic properties increase the potential of swelling of the nanoclays in water [44]. The aggregation of nanoclay in water or in an electrolytic solution enhances an exchangeability of cations and water molecules between the interlayer resulting in exfoliating the clay platelets in a short time frame [23].

3.3.1 Barrier and Mechanical Properties of Nanocomposites

Incorporating matrix materials with reinforcing materials to improve strength of composites leads to enhanced protection of their surfaces from stress or abrasion [4, 23, 39, 40, 45]. Layered silicates have been incorporated into matrix materials such as polymers and metals through electrochemical synthesis [23,45,54,55,56]. Ritchie (2009) enhanced the fracture toughness and hardness of polymer composites by dispersing layered ceramics into polymethylmethacrylate polymer [46,47,48]. Nanostructured coatings improved the corrosion protection of materials. Dispersing of layered silicate nanoparticles into matrix materials allows a uniform fabrication due to high surface area and fine platelets which enhance nanocomposite performances with low loading content [4]. In fact, the optimal loading of an exfoliated nanoclay in polymer matrix nanocomposites is around 4-5 wt % [18,19]. Montmorillonite was dispersed into polymer matrices to increase mechanical strength [42-50]. The presence of layered silicates in conductive polymer coatings enhanced the corrosion resistance of the nanocomposites due to reducing coating porosity and decreasing the path length of water and gas permeation [51]. The layered silicate retarded the mobility of small molecules through the matrix by creating a “tortuous path” as shown in Figure 3.4 which protected the substrate from reacting with the permeable molecules. [4].

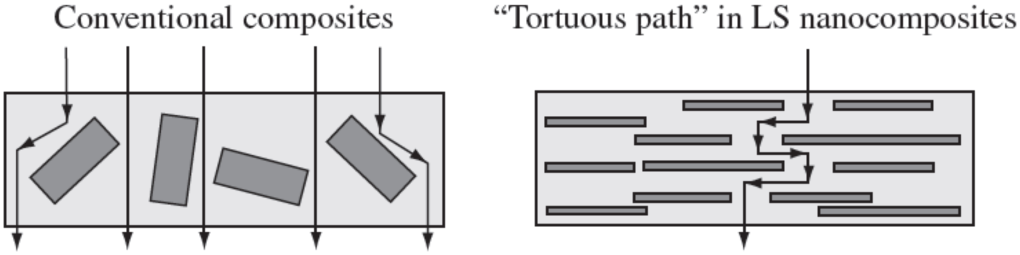

Figure 3.4: Tortuous path in polymer/layered silicate nanocomposites [4].

Reinforcing polymers with montmorillonite improved the thermal stability and mechanical strength of nanocomposites [4,50,51,53]. Wang et.al. (2010) reported that incorporation of montmorillonite into the polypyrole polymer by electrochemical synthesis improved both thermal stability and hardness of the polypyrole/montmorillonite composite film [52]. It is shown that a low percentage of clay, only 0.02%, enhanced the hardness of the composite from 0.13 GPa to 0.18 GPa [52].

An electrochemical fabrication of nickel incorporated with montmorillonite layered silicate was first deposited onto copper and stainless steel substrates [54-57]. It was reported that the electrosynthesized nickel/layered silicate nanocomposite film showed higher hardness and Young modulus values than that of the pure nickel film. It was exhibited that the nickel nanocomposite, which was incorporated with 1% layered silicate particles, enhanced crystallization growth. [54]. However, the increased concentration of the montmorillonite over 1% caused an inhibiting effect on the crystalline growth after sintering [54]. It was supported that the developed horizontal orientation of the electrochemical cell by inversely positioning working the electrode enhanced incorporation of the layered silicate nanoparticles into the nickel deposit, and as a result increased hardness and modulus values.

The purpose of this research is to reinforce nickel and nickel alloy coatings with layered silicates for enhanced corrosion resistance and mechanical properties based on nacre inspired materials. Nacre is a kind of marine shell which itself is fabricated by combining the two beneficial components of brittle calcium carbonate and ductile organic matter as an adhesive leading to enhanced toughness [46-48]. To incorporate this concept into my work, I developed an engineered nanocomposite by reinforcing nickel and nickel alloy matrices with layered silicate nanoparticles to increase mechanical strength and corrosion resistance. Electrochemical deposition is a method used to fabricate the nanocomposite coating onto stainless steel discs. The layered silicate-reinforced metal nanocomposites lead to high hardness and increased fracture toughness which resist mechanical impact, i.e. stress [54]. Additionally, an optimal amount of layered silicate nanoparticles were used to reinforce metal matrices required to enhance corrosion resistance to chloride ions and improve mechanical strength, resulting in an expanded service life and decreased maintenance cost for use in the offshore oil and gas field.

3.4 Mechanical Properties

The nanoindentation technique is used for determining both modulus and hardness corresponding to the microstructure and mechanical properties of the materials [58]. The indentation results obtained using a continuous loading indenter. The hardness-depth relationship was obtained using continuous stiffness measurement (CSM) with a dynamic technique. The tests were conducted at a constant strain of 0.05 to a maximum depth of 400 nm. The load-displacement data obtained during the final unloading were analyzed to establish the hardness and elastic modulus using the method of Oliver and Pharr [57]. The depth of displacement together with the known geometry of the indenter offers an indirect measuring area of contact at full load, from which the mean contact pressure, and thus hardness is estimated. The hardness (H) is calculated from the indentation load divided by contact area regarding to the formula:

$$H = \frac{P}{A_C}, \qquad \text{Eq. (2.1)}$$

where A_c is the actual contact area and P is a maximum load. When load is removed from the indenter, an analysis of the initial portion of this unloading response gives an estimate of the elastic modulus. The reduced modulus, E_r, describing to an elastic displacement of the samples and indenter is represented as the equation:

$$E_r = \frac{1}{\beta}\frac{\sqrt{\pi}}{2}\frac{S}{\sqrt{A_C}}, \qquad \text{Eq. (2.2)}$$

where β is a constant value of 1.034 for a Berkovich tip, S is a contact stiffness characterized by a curve fitting the upper portion of the unloading curve and measuring its slope at peak load. A_c is contact area and can be deduced from an empirically determined shape function. The elastic modulus of the specimen (E) is calculated from the effective modulus as the following form:

$$\frac{1}{E_r} = \frac{1-\nu_i^2}{E_i} + \frac{1-\nu_s^2}{E}, \qquad \ldots\text{Eq. (2.3)}$$

where E_i is modulus of indenter, and ν_s and ν_i are Poisson's ratio for the specimen and the indenter, respectively. The values E_i = 1140 GPa, ν_i = 0.07 and ν_s = 0.29 are used in the calculation. The load-displacement data obtained during the final unloading were analyzed to establish the modulus (E_r) and hardness (H) using the method of Oliver and Pharr. The measured E_r was converted to elastic modulus using CSM method with the equation (2.3). The average data of elastic modulus (E) and hardness (H) are from different 25 indentations.

Nanoindentation experiments were performed with a MTS nanoindenter XP following the constant stiffness method standard hardness/modulus with a three-sided pyramid Berkovich tip [58]. Prior to testing, the indenter system was calibrated on a sample of fused silica with 25 indents. The specimen was mounted on an aluminum stub where it was fixed to the sample holder stage and with the help of a microscope the indentation spots were identified. Twenty indentations were done in square array with a gap of 20 microns between each indent. The percent unload in the stiffness calculation was kept to 50% and allowable drift correction was kept at 0.05 nm/s with a drift correction of 1.

Vickers hardness was measured using Buehler microhardness testing machine model Micromet 5101, Mitutoyo Corporation, Japan. The applied load was 10 gf for 20 s. For each test, five readings were done to represent the average value.

3.5 Chapter References

[1] Callister Jr., W.D., Rethwisch, D.G., *Materials Science and Engineering: An Introduction*, 8th Ed., New York: John Wiley and Sons, 2010.

[2] Hull, D., Clyne, T. W., *An introduction to composite materials*, second edition, Cambridge Solid State Science Series, The Press of the Syndicate of the University of Cambridge, Cambridge University Press: New York, 1996.

[3] Kaw, A.K., *Mechanics of composite materials, Mechanical and Aerospace Engineering Series*, 2nd Ed., Florida: CRC Press Taylor and Francis Group, 2006.

[4] Camargo, P.H.C., Satyanarayana, K.G., Wypych, F., *Materials Research.* **2009**, 12(1), 1-39.

[5] Branagan, DJ, Tang, Y., *Applied Science and manufacturing*. **2002**, 33(6), 855-859.

[6] Ying DY, Zhang DL., *Materials Science and Engineering*. **2000**, 286(1), 152-156.

[7] Marchal Y, Delannay F, Froyen L., *Scripta Materialia*. **1996**, 35(2), 193-198.

[8] Goujon C, Goeuriot P., *Materials Science and Engineering*: A. **2001**, 315(1-2), 180-188.

[9] Aruna ST, Rajam KS, *Scripta Materialia*. **2003**, 48(5), 507-512.

[10] Stobrawa, J.P., Rdzawski, Z.M., *Journal of Achievements in Materials and Manufacturing Engineering.* **2009**, 32(2), 171-178.

[11] Möller, A., Hahn, H., *Nanostructured Material.* **1999**, 12(1-4), 259–262.

[12] Aruna, S.T., William Grips,V.K., Rajam, K.S., *Journal of Alloys and Compounds.* **2009**, 468(1-2), 546–552.

[13] Vaezi, M.R., Sadrnezhaad, S.K., Nikzad, L., *Colloids and Surfaces A: Physicochem. Eng. Aspects*. **2008**, 315, 176-182.

[14] Aruna, S.T., Bindu, C.N., Ezhil Selvi, V., William Grips, V.K., Rajam, K.S., *Surface and Coatings Technology*. **2006**, 200(24), 6871-6880.

[15] Shao, I., Vereecken, P.M., *J. Mater. Res.* **2002**, 17(6), 1412-1418.

[16] Branagan, DJ., Alman, DE, Newkirk, J.W., *Powder metallurgy, particulate materials for industrial applications.*, Ed., TMS Publication: St. Louis, 2000.

[17] Sautter, F.K., *J. Electrochem. So*c. **1963**, 110, 557-560.

[18] Boch, P., Niepce, J.C., *Ceramic materials: processes, properties and applications*, 2nd Ed., Hermes Science Publications: France, 2001.

[19] Liang, C., Guo, J., Hu, X., *Journal of Wuhan University of Technology-Mater. Sci. Ed*. **2007**, 22(1), 12-16.

[20] E. Munch, M. E. Launey, D. H. Alsem, E. Saiz, A. P. Tomsia, R. O. Ritchie, *Science*. **2008**, 322, 1516-1520.

[21] Takahashi, R., Sato, S., Sodesawa, T., Suzuki, M., Ichikuni, N., Microporous and Mesoporous Materials. **2003**, 66(2-3), 197-208.

[22] Yao, Y., Yao, S., Zhang, L., Wang, H., Materials Letters. **2007**, 61(1), 67-70.

[23] Wang, A.Q., D'Souza, N., Golden, T.D., *Applied Clay Science.* **2008**, 42, 310-317.

[24] Surender, M., Balasubramaniam, R., Basu, B., Surface and Coatings Technology. **2004**, 187(1), 93-97.

[25] Surender, M., Basu, B., Balasubramaniam, R., *Tribology International*. **2004**, 37(9), 743-749.

[26] N. Sombatsompop, K. Sukeemith, T. Markpin, N. Tareelap, *Materials Science and Engineering: A*. **2004**, 381(1-2), 175-188.

[27] M. Stroumbouli, P. Gyftou, E.A. Pavlatou, N. Spyrellis, *Surface and Coatings Technology.* **2005**, 195(2-3), 325–332.

[28] C.T.J. Low, R.G.A. Wills, F.C. Walsh, *Surface and Coatings Technology*. **2006**, 201(1-2), 371-383.

[29] P. Wu, H.M. Du, X.L. Chen, Z.Q. Li, H.L. Bai, E.Y. Jiang, *Wear*. **2004**, 257(1-2), 142-147.

[30] Y. Boonyongmaneerat, K. Saengkiettiyut, S. Saenapitak, S. Sangsuk, *Surface and Coatings Technology*. **2009**, 203(23), 3590-3594.

[31] I. Garcia, J. Fransaer, J.-P Celis, *Surface and Coatings Technology*. **2001**, 148(2-3), 171-178.

[32] B. Szczygieł, M. Kołodziej, *Electrochimica Acta*. **2005**, 50(20), 4188-4195.

[33] B. Xiong, C. Cai, Z. Wang, *Journal of Alloys and Compounds*. **2014**, 583, 574–577.

[34] T. Tabaru, J.-H. Kim, K. Shobu, M. Sakamoto, H. Hirai, S. Hanada, *Metallurgical and Materials Transactions A*. **2005**, 36A, 619-626.

[35] E. A. Beidler, C. F. Powell, I. E. Campbell, L. F. Yntema, *Journal of the Electrochemical Society*, **1951**, 21-25.
[36] I. Corni, R. J. Chater, A. R. Boccaccini, M. P. Rya, *J Mater Sci*. **2012**, 47, 5361–5373.

[37] M.E. Bahrololoom, R. Sani, *Surface and Coatings Technology*. **2005**, 192(2-3), 154-163.

[38] R. Sen, S. Das, K. Das, *Metallurgical and Materials Transactions A*. **2012**, 43A, 3809-3823.

[39] C.T.J. Low, R.G.A. Wills, F.C. Walsh, *Surface and Coatings Technology*.**2006**, 201(1-2), 371-383.

[40] W. Chen, Y. He, W. Gao. *Journal of The Electrochemical Society*. **2010**, 157(8), E122-E128.

[41] D.M.; Moore, R.C., Reynolds Jr. *X-ray diffraction and the identification and analysis of clay minerals, X-Ray Diffraction and the Identification and Analysis of Clay Minerals*, Ed., Oxford University Press: New York, 1997.

[42] Madejová, J., Arvaiová, B., Komadel, P., *Spectrochimica Acta Part A*. **1999**, 55(12), 2467-2476.

[43] J.M. Cogen, T.S. Lin, A.B. Morgan, J.M. Garces, *Novel synthetic nanocomposite materials and their application in polyolefin-based wire and cable compounds*, The Dow Chemical Company, LOES Form number 311-01101, 1-7.

[44] Kim, T. H., Jang, L. W., Lee, D.C., Choi, H. J., Jhon, M. S., *Macromol.Rapid Commun*. **2002**, 23, 191-195.

[45] A. Q. Wang, N. A. D'Souza, T.D. Golden, J. *Mater. Chem*. **2006**, 16, 481-488.

[46] M.E. Launey, E. Munch, D.H. Alsem, H.B. Barth, E. Saiz, A.P. Tomsia, R.O. Ritchie, *Acta Materialia*. **2009**, 57, 2919–2932.

[47] M.E. Launey, R. O. Ritchie, *Adv. Mater*. **2009**, 21, 2103–2110.

[48] E. Munch, M. E. Launey, D. H. Alsem, E. Saiz, A. P. Tomsia, R. O. Ritchie1, *Science*, 322, 2008, 1516-1520.

[49] Ogunsona, E., Ogbomo, S., Nar, M., D'Souza, N.A., *Cellular Polymers*. **2011**, 30(2), 79-93.

[50] M.C. Richardson, J. Kim, D. Ho, C.R. Snyder, N.A. D'souza and G.A. Holmes, *Polymer Composites*. **2011**, 32(1), 67-78.

[51] D. Zaarei, A. A. Sarabi, F. Sharif, S. M. Kassiriha , *J. Coat. Technol. Res*. **2008**, 5 (2) 241-249.

[52] Wang, C. A.; Chen, K.; Huang, Y., *J. Mater. Res.* **2010**, 25(4), 658-664.

[53] L. Sahu and N.A. D’Souza, *The Open Macromolecules Journal.* **2012**, 628-632.
[54] R. A. Horch,; T. D. Golden, N.A. D'Souza, L. Riester, *Chemistry of Materials.* **2002**, 14 (8), 3531-3538.

[55] J. Tientong, C. R. Thurber, N.A. D’Souza, A. Mohamed, T. D. Golden, *International Journal of Electrochemistry*, **2013**, 1-8.

[56] J. Tientong, Y.H. Ahmad, M. Nar, N.A. D'Souza, A.M.A. Mohamed, T.D. Golden, *Materials Chemistry and Physics.* **2014**, 145, 44-50.

[57] Y.H. Ahmad, J. Tientong, N.A. D'Souza, T.D. Golden, A.M.A. Mohamed, *Surfaace & Coatings Technology.* **2014**, 242, 170-176.

[58] The Nano Indenter® XP, *TestWorks 4 Nanoindentation*, MTS Systems Corporation. A, 1999-2002.

[59] W.C. Oliver, G.M. Pharr, *J. Mater. Rev.* **1992**, 7, 1564–1583.

CHAPTER 4

CORROSION

4.1 Corrosion Theory

Corrosion, a natural phenomenon, is deterioration of metal through an electrochemical process [1, 2], a destructive result of a chemical reaction occurring between a metal and its environment [3]. When metal is exposed to moisture rich environments, such as in air, acidic or basic solutions or salt systems, the metal will react with the environment to reach a more stable state. The metal can be in contact with the corrosive environment through a small droplet or complete immersion [3]. The corrosion product formed on the metal surface is called rust which can be similar to its mineral [3, 4]. The corrosive system is comprised of anodic and cathodic regions where the metal transfers electrons from the anode (electron donor) to a cathode (electron acceptor) through the metal component, completing the electrical circuit. The resulting dissolved metal at the anode then becomes a positively charged ion [3]. This process is known as oxidation. In natural environments, all metals have a tendency to be oxidized. Some metals are easier to oxidize than others depending on the relative strength of the galvanic series. The galvanic series chart shows the metals' potential information (Figure 4.1), which is useful for metal selection in industrial applications [3]. The potential series are used to select appropriate metals used in certain environments to prevent corrosion through cathodic corrosion protection [3].

The typical steps involved in promotion of the corrosion process are summarized as the following [1]:

(1) Ions involved in the process need a medium in which to migrate, known as an electrolyte (typically water).

(2) Oxygen molecules are supplied in the corrosion process.

(3) The metal elements have to release electrons to initiate the process.

(4) The products generated may promote rust formation or form a barrier to protect the original underlying metal.

(5) All steps are required and a driving force is needed to achieve the process.

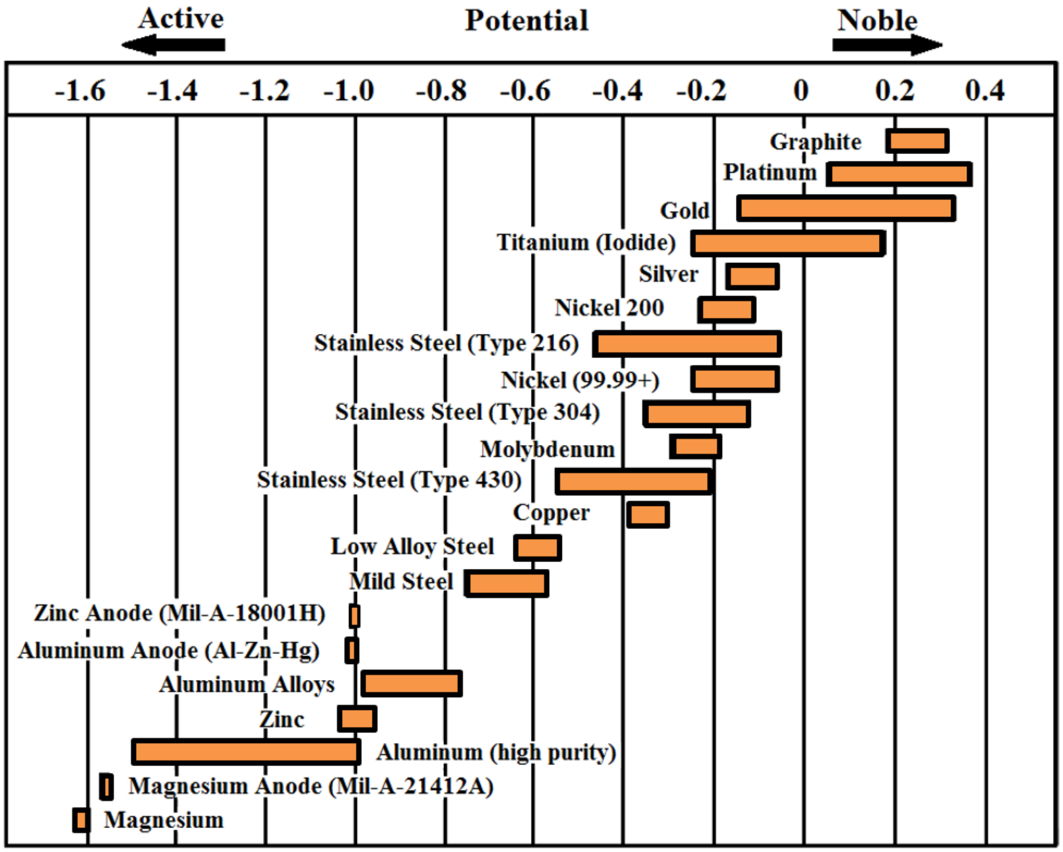

Figure 4.1: The galvanic series of metals in seawater.

In general corrosion, the dissolution of metal begins with oxidation (loss of electrons) which generates metal ions (positively charged) and electrons in the system [1].

$$M \rightarrow M^{n+} + ne^{-} \qquad \text{Eq. (3.1)}$$

where

M = metal
M^{n+} = positively charged metal species
n = valence of corroding metal species
e^{-} = electrons

On the surface of the metal, electrons generated at the anode flow through the metal to the cathode. The cathode is an electron acceptor and undergoes reduction (gain of electrons) at the metal-electrolyte interface [1]. In neutral or alkaline solutions with the presence of dissolved oxygen, the predominant cathodic reaction in water results in the generation of hydroxide ions [1].

$$O_{2(g)} + 2H_2O_{(l)} + 4e^- \rightarrow 4OH^-_{(aq)} \qquad \text{Eq. (3.2)}$$

Under deaerated acidic conditions, the cathodic reaction results in the formation of hydrogen gas [1].

$$2H^+_{(aq)} + 2e^- \rightarrow H_{2(g)} \qquad \text{Eq. (3.3)}$$

In aerated acidic conditions, dissolved oxygen reacts with hydrogen ions at the cathode, forming water molecules [1].

$$O_{2(g)} + 4H^+_{(aq)} + 4e^- \rightarrow 2H_2O_{(l)} \qquad \text{Eq. (3.4)}$$

In a corrosive environment, anodic and cathodic reactions must occur. The anodic reaction involves the dissolution of metal creating metallic ions and electrons. The secondary process involves consumption of the electrons in a cathodic reaction. The number of electrons generated by the corrosion process is equivalent to the electrons consumed in the cathodic reaction. The cathode and anode need to be adjacent areas which are immersed in the electrolyte or exposed to a moisture rich environment. The electrons flow from the anode (negative electrode) to the cathode (positive electrode) through the metal (electrical circuit connecting anode and cathode) resulting in corrosion [3].

Steels, typically constructed from iron (Fe), are a simple example of the corrosion process [5]. When steel is exposed to an aerated solution as shown in figure 4.2, the reaction of iron occurring at the anode is [3]:

$$2Fe_{(s)} \rightarrow 2Fe^{2+}_{(aq)} + 4e^- \text{ (anodic)} \qquad \text{Eq. (3.5)}$$

Then the following redox reaction commonly occurs to generate ferric ion.

$4Fe^{2+}_{(aq)} + O_{2(g)} \rightarrow 4Fe^{3+}_{(aq)} + 2O^{2-}_{(aq)}$ Eq. (3.6)

At the cathode adjacent to the anode, the reduction of oxygen will occur:

$O_{2(g)} + 2H_2O_{(l)} + 4e^- \rightarrow 4OH^-_{(aq)}$ (cathodic) Eq. (3.7)

The overall oxidation- reduction (redox) reaction of the iron corrosive system is:

$2Fe_{(s)} + O_{2(g)} + 2H_2O_{(l)} \rightarrow 2Fe^{2+}_{(aq)} + 4OH^-_{(aq)}$ Eq. (3.8)

After dissolution of iron, ferrous ion (Fe^{2+}) quickly combines with hydroxide ion to form iron (II) hydroxide precipitate at the cathode.

$Fe^{2+}_{(aq)} + 2OH^-_{(aq)} \rightarrow Fe(OH)_{2(s)}$ Eq. (3.9)

In addition, the following acid-base reactions lead to the formation of iron (II) and iron (III) hydroxide precipitation.

$Fe^{2+}_{(aq)} + 2H_2O_{(l)} \rightarrow Fe(OH)_{2(s)} + 2H^+_{(aq)}$ Eq. (3.10)

$Fe^{3+}_{(aq)} + 3H_2O_{(l)} \rightarrow Fe(OH)_{3(s)} + 3H^+_{(aq)}$ Eq. (3.11)

The dehydration reactions of the precipitation result in forming corrosion product or rust as following.

$Fe(OH)_{2(s)} \rightarrow FeO_{(s)} + H_2O_{(l)}$ Eq. (3.12)

$Fe(OH)_{3(s)} \rightarrow FeO(OH)_{(s)} + H_2O_{(l)}$ Eq. (3.13)

$2FeO(OH)_{(s)} \rightarrow Fe_2O_{3(s)} + H_2O_{(l)}$ Eq. (3.14)

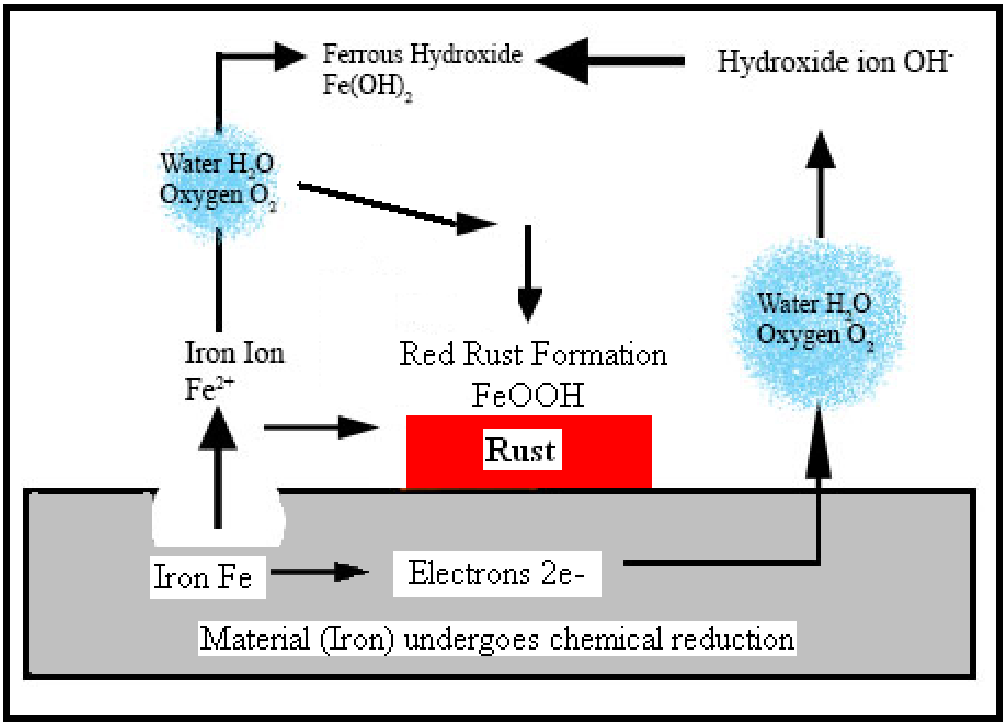

Figure 4.2: The basic corrosion cell consists of an anode, a cathode, an electrolyte and a metallic path for electron flow. Note the corrosion current always flows from the anode to the cathode in the electrolyte.

4.2 Localized Corrosion

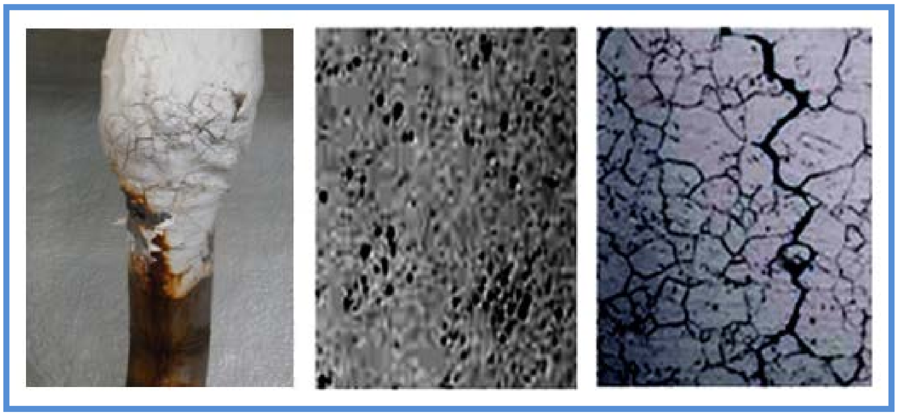

Figure 4.3: Localized corrosion: crevice corrosion (left), pitting corrosion (middle), intergranular corrosion (right) [21].

Localized corrosion is an intense attack at confined area of the metal while the surrounding corrodes at lower rate. The deterioration initiates from a miniature area on the metal surface, which may be concealed by the corrosion products and consequently difficult to detect. The localized corrosion forms include pitting corrosion, crevice corrosion, and intergranular corrosion (Figure 4.3) [21]. In particular, alloys or metals which develop passivation are predominantly damaged by penetration of chloride ions into the weakest part of the oxide film leading to the underneath metal rapidly dissolving [24]. Chloride ions preferring to migrate into the defect of an oxide layer result in growing pit nucleation [24]. This small pit on the surface can rapidly propagate by chloride penetrating into the bulk can cause the structure failure [3].

4.2.1 Pitting Corrosion

Pitting corrosion is a miniature hole or cavity on the metal surface typically occurring by de-passivating of the self-protective metal oxide film [20-21]. The small cavity becomes anodic, while the large area of the passive film becomes cathodic, consequently producing a localized galvanic reaction [22-23]. The vast ratio of the small active anodes to large passive cathodes leads to severe pitting due to the increased corrosion rate of the pit [22-23]. The small attack penetrates deeply into the metal ultimately resulting in a structure collapse [3, 20-23]. This small attack which may be covered with its rust, is accordingly difficult to investigate [22-23]. The cross-section of a typical growing pit on stainless steel in chloride media is shown in figure 4.4.

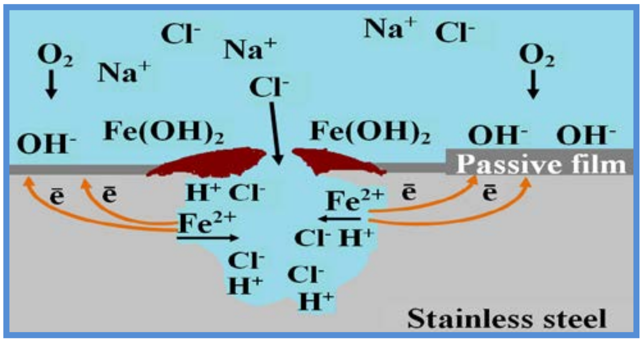

Figure 4.4: The cross-section through a typical growing pit of the stainless steel in chloride media.

4.2.2 Crevice Corrosion

Crevice corrosion or concentration-cell corrosion occurs at a specific region which is typically associated with stationary environments such as under rivet heads, gaskets, clamps or joints [22-23]. The difference in oxygen concentration between the covered spot and the outside exposed to the bulk solution consequently leads to the driving force for the crevice corrosion. Creating salt deposits or metal oxide films on the metal surface also leads to the reduction of oxygen concentration [23]. Additionally, the region where the metal surface is exposed to water containing oxygen can also generate the oxygen-concentration cell by the water-oxygen reduction reaction to give hydroxyl ions [23]: $O_2 + 2H_2O + 4e^- \rightarrow 4(OH^-)$. The metal surrounded with low oxygen concentrations acts as an anode [23]. Inside the cavity, there is high metal ions concentration due to the dissolution of the metal [23], such as the anodic reaction of: $Fe \rightarrow Fe^{2+} + 2e^-$. Additionally, inside the cavity or underneath the lap joint or gasket, the solution is stagnant resulting in the increased metal ions concentration [22-23].

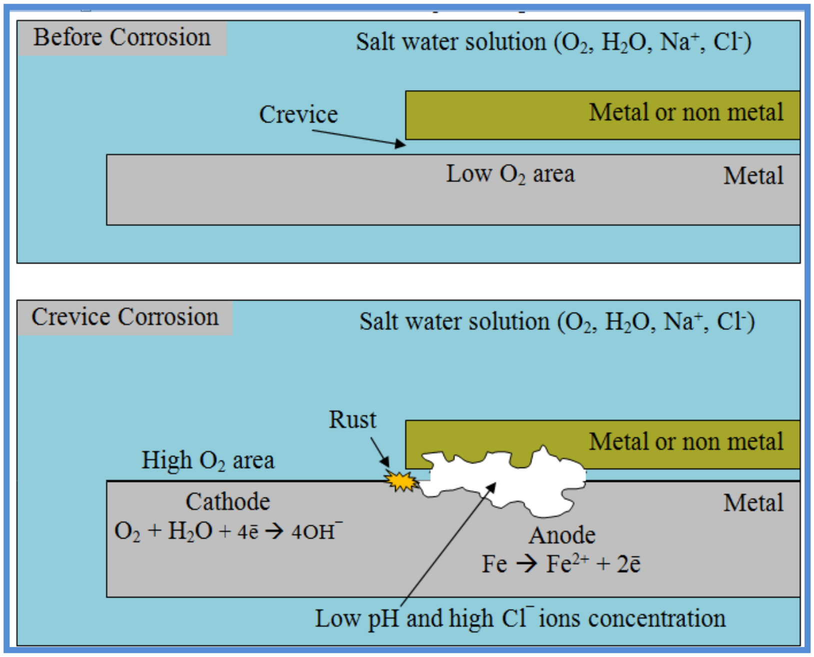

Figure 4.5: Schematic of occurring crevice corrosion.

In the presence of chloride ions in the environment and due to an electrical imbalance, chloride ions, which are negatively charged ions, are consequently attracted into the cavity which contains the high positively charged metal ions concentration [23]. The reaction occurring in the cavity is accordingly shown as: $FeCl_2 + 2H_2O \rightarrow Fe(OH)_2 + 2HCl$. Once pitting or crevice corrosion is started, it becomes an autocatalytic reaction to form hydrochloric acid and decrease the pH and increase the chloride ion concentration inside the cavity [23]. The schematic crevice corrosion is shown in figure 4.5.

4.2.3 Intergranular Corrosion

Intergranular corrosion or intercrytalline corrosion is from local damage arising along the grain boundaries of an alloy [21]. It occurs when each crystalline grain exhibits different physical and chemical properties where resulting in posing different electrochemical potential. For example, if crystalline has the physical properties difference between center and its boundary, it poses the two separate electrochemical potential behaving as an anode and cathode when immersed in an electrolyte leading to occurring corrosion reaction [21]. The tiny localized corrosion rapidly arises at the grain boundary which causes the protective film to ultimately delaminate from the underlying metal [21]. The inappropriate alloy production process such as incorrect heat treatment (sensitization) is at risk to cause the alloy to intergranular corrosion. [21]**.** Chromium-nickel stainless steel is the most well-known example to occur the intergranular corrosion. In the presence of small number of the carbon in the steel, in the heating process, chromium is able to form small carbide compound. At the low heat processing ($<400\ ^{o}C$) the diffusion is slow resulting in the chromium carbides are formed only at the grain boundaries leading to a different composition between bulk and boundaries. During the sensitization, chromium carbides form at the grain boundaries. The chromium atoms diffuse from the bulk to the grain boundaries then chromium depletion occurs. At a high temperature processing then bulk diffusion is sufficient results in carbide can be formed everywhere. Hence, it is crucial to control the heat treatment temperature and time to avoid the different metal diffusion in the grain which is able to cause the intergranular corrosion

4.3 Corrosion Protection

One method to prevent the onset of corrosion is to reduce the metal dissolution rate. Generally, at low pH the metal dissolves directly from the metal surface into free metal ions, whereas at high pH the metal dissolves through an oxyhydroxide film. Corrosion can be inhibited thermodynamically through cathodic protection or kinetically by a passive surface layer. Improvement of the passive layer is the most common form of protection for metals. The study of the passive film is consequently a key to prevent corrosion through kinetic properties and a key to developing materials which are able to extend the service life of the materials when exposed to aggressive environments.

4.3.1 Mechanism of Passive Film Growth

When metals or metal alloys are exposed to aqueous media, a two-layered passive film forms naturally on the surface of the metals, consisting of a metal oxide barrier (inner layer) and a metal hydroxide or salt film (outer layer). Passivity is a natural formation of a metal oxide thin film with thickness of 1-3 nm on the metal surface [6, 25]. Passivation is rapidly achieved due to surface-adsorbed hydrated complexes of metals which are able to remain on the surface of the alloy (Figure 4.6). The hydrated metal complexes are further reduced to metal hydroxides. Ultimately, the reaction rapidly progresses by deprotonating to form an insoluble metal oxide film bound to the alloy surface. The inner oxide layer prevents the underlying metal from corroding, leading to a decline in the corrosion rate of the metal. Thus, the key to improve corrosion resistance is to alloy the metal of interest with other corrosion resistant metals which are able to further enhance passivation of the metal [6]. For instance, alloying nickel with molybdenum is to improve creating passive layer because molubdenum is able to form a stable molybdenum oxide film rapidly to stop pitting nucleation.

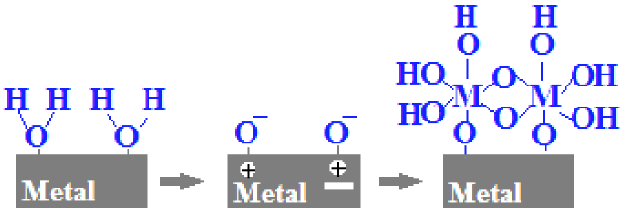

Figure 4.6: Schematic of a metallic passivated surface [6].

The oxide films protect the metal surface from corrosive aqueous solutions. The passive films, nanometer in thickness, are at risk of localized breakdown resulting in accelerated dissolution of the underlying metal. Additionally, scratching causes mechanical damage that can destroy the passive layer. In the presence of chloride ions, the attack initiates pitting on the metal surface, and chloride ions migrate and obstruct the pitting site propagating a large destructive area leading to crevice corrosion. This localized corrosion can lead to structural failure. The resistance of the anodic oxide film to dissolution is related to the chemical and physical properties of the metal oxide (Figure 4.7). Aggressive environments with temperature, pH and chloride ions are major factors affecting increase of corrosion rates. The environmental and material parameters including potential, alloy composition, electrolyte concentration and temperature are used to evaluate the breakdown of the passive layer which leads to pitting corrosion. These parameters affect pit growth, growth and stability of the passive film, and self-healing of the corrosion pit.

However, the mechanism of the initiation of pitting, or the breakdown of the protective passive film, is not clearly understood.

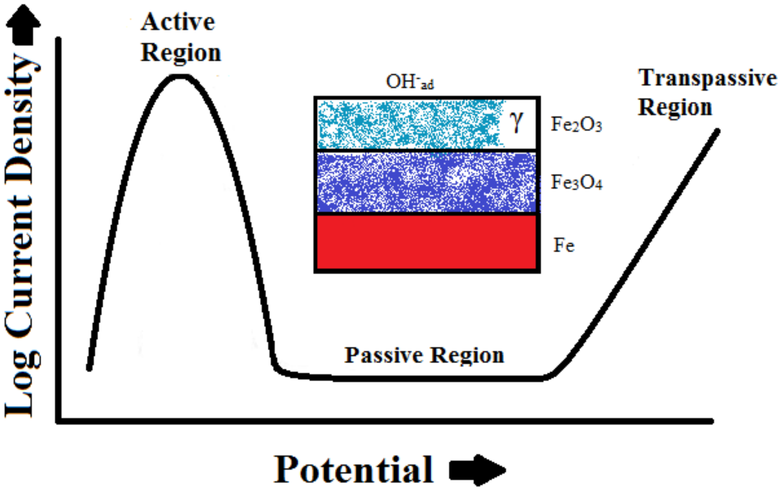

Figure 4.7: Illustration of an active-passive transition where iron is anodically polarized in an aqueous solution.

4.3.2 Stainless Steels and Corrosion Issues

Stainless steels are iron based alloys [5] and are most extensively studied in corrosive environments. Stainless steel type 304 (UNS number S30400) is a general purpose grade, is comprised of 18-20% chromium, 8-10% nickel, 2% maganese, 1% silicon, 0.080% carbon, 0.045% phosphorus, 0.030% sulfur and balance % iron [5]. Stainless steel type 304 is widely used in applications requiring a good combination of corrosion resistance and formability. Steels containing a minimum of 11% chromium are believed to enhance corrosion resistance [5], however some stainless steels now comprise up to 30% chromium. Additionally, many other elements are incorporated into steel to provide specific desired properties or ease production of the material [5]. For instance, nickel, molybdenum and nitrogen are introduced to enhance corrosion resistance. Carbon, molybdenum, titanium, aluminum, copper and nitrogen increase mechanical strength of steel. Nickel improves formability and toughness while sulfur and selenium are used to improve machinability [5].

Type 316 is a nickel based stainless steel [6]. Nickel stainless steels are the largest produced steels in the United States. Type 316, which includes 2-3% molybdenum, has increased resistance to pitting in seawater and chemical industry environments as compared to type 304. Alloy 625 is a high-molybdenum nickel base steel offering high temperature stability. For example, inconel alloy is a type 625 steel, containing 22% chromium, 9% molybdenum, 5% iron and balance % of nickel [5]. Steel forms a thin metal oxide layer known as the passive film which protects the underlying steel from corrosion [5, 7]. The passive film has self-healing behavior when exposed to a wide range of environments [5, 7]. The metal oxide may be formed on the metal surface as a barrier to corrosion in the presence of oxygen or oxidizing chemicals, however when the temperature of the solution increases or the environment is filled with chloride ions the protective films dissolve [8]. Consequently, it has been reported that many corrosion failures can occur in service owing to localized attack such as pitting, crevice corrosion, intergranular corrosion and stress-corrosion cracking as a result of the breakdown of the passive film [8].

From 1968 to 1971, the incidences of about 50% of the 685 failures of DuPont corrosion resistant piping and equipment in the chemical process were attributed to corrosion, while the others were caused by the weakening mechanical properties of the material [5]. In fact, it was revealed that localized corrosion of stainless steel accounted for one half of the corrosion failures [5]. The localized corrosion, which is a result of corrosion initiating on the metal surface is a fundamental issue that needs to be first understood in order to then correct it. The metal is able to construct a metal oxide as its protective film, but some of the film growth is not a strong barrier against the harsh environments to which it is exposed, such as high chloride environments, and eventually loses its resistant properties. A mechanical scratch is another imperative factor that can damage the metal oxide film, leading to severe corrosion. The metal oxide, protecting the underlying metal, must be durable and able to quickly repair itself when the film is broken.

4.3.3 Nickel for Corrosion Protection

Nickel use has been continually increasing for corrosion protection purposes since the beginning of commercial production in the twentieth century [8]. Pure nickel offers high ductile ability and toughness due to its capacity to hold a face-centered cubic crystalline structure until its melting point (1455^{o}C) is reached [8]. Therefore, nickel provides an important basis for developing specialized alloys. Nickel can form intermetallic phases when alloyed with specific materials, resulting in enhanced high strength for both low and high- temperature systems [8,9]. Due to the stable nature of nickel, it is often used to alloy with other metals to protect materials operating under severe conditions such as high corrosive, high temperature or high stress environments. Nickel is tolerant of nonaerated reducing acids such as hydrochloric, sulfuric and phosphoric acids, but can be rapidly corroded by oxidizing acids such as nitric and other mineral acids containing significant amounts of oxidizing salts like ferric or cupric salts, nitrates or peroxides [8]. Nickel is able to moderately withstand high-heated air and oxygen rich environments and has particular resistance at elevated temperatures to strong corrosive alkaline solutions such as caustic soda. Due to the formation of a protective nickel halide film, nickel is also able to offer protection at elevated temperatures with the presence of halogen gases, e.g. chlorine and fluorine, as opposed to the majority of other metals [8]. Nickel is resistant to most deaerated organic acids and other organic compounds. Ultimately, nickel is often utilized in food processing or consumer-product applications where nontoxic effects and non-promotion of fat oxidation is advantageous [8]. In most natural fresh waters, including ground, distilled, deionized, and high-purity waters, nickel has a high degree of corrosion resistance. It is resistant in rapidly moving seawater systems; however severe pitting attacks arise under fouling organisms or other precipitates which can deposit on the surface of the metal in stagnant or low-velocity seawater [8].

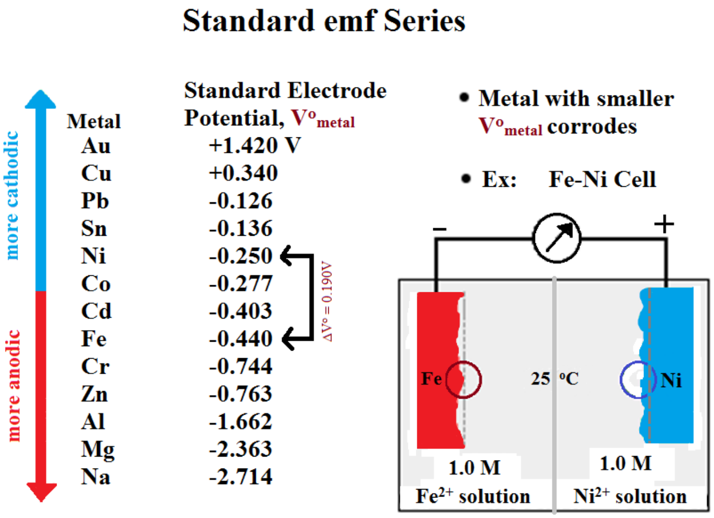

Figure 4.8: Electromotive force series.

In the electromotive force series, as can be seen in figure 4.8, the standard reduction potential of nickel (-0.25 V) is more noble than that of iron (-0.44 V) but less noble than that of copper (+0.34 V). As a general rule, nickel favors corrosion under oxidizing conditions, e.g. in nitric acid whereas under reduction conditions, such as in hydrochloric acid and alkaline solutions, corrosion is retarded. However, nickel has the ability to protect itself from specific types of attack through formation of corrosion-resistant or passive oxide film formation allowing nickel to behave as a more noble material than copper. As a result of passive metal formation, the reducing condition does not typically accelerate corrosion. However, when an oxide film is locally destroyed such as in hot chloride solutions, it may cause nickel to undergo pitting in this area [8].

4.3.4 Molybdenum for Enhancement of Corrosion Resistance

Molybdenum, in the same periodic group as chromium and tungsten, has a melting point of 2620 °C. Molybdenum has similar heat stability as compared to tungsten [8]. It is currently the most common material used in Cu(In, Ga)Se_2 (CIGS) solar cell back contacts due to its chemical and mechanical inertness, high conductivity, low resistance contact with the CIGS layer, and commensurate coefficient of thermal expansion [10,11]. Molybdenum metal offers high resistance to corrosive nonoxidizing solutions including hydrofluoric, hydrochloric and phosphoric acids under a wide range of concentrations and temperatures. It is particularly resistant to boiling sulfuric acid at concentrations up to 60% [8]. In addition to nickel and nickel alloys, molybdenum is particularly resistant to corrosion and pitting attack by chlorides [8].

Nickel-molybdenum alloys comprising 26 to 30% molybdenum exhibit useful resistance to corrosion under all concentrations and temperatures of hydrochloric acid [8]. The alloys are resistant to boiling acids, up to 60% sulfuric acid and pure 85% phosphoric acid, yet, the alloy does not offer resistance under strong oxidizing conditions [8]. Molybdenum, which improves pitting resistance, has been alloyed in stainless steel used in high chloride containing media [12]. The incorporation of molybdenum in stainless steel improves corrosion resistance by decreasing current density [12]. Molybdenum added to stainless steel increased pitting corrosion protection by formation of molybdenum oxide passive films which is more resistant to pitting corrosion [12]. The addition of molybdenum to nickel increases resistance to reducing environments and pitting attack from chloride containing solutions, while the addition of sufficient chromium to nickel increases resistance to oxidizing environments such as nitric acid and high-temperature oxidation [8]. Thus, molybdenum and chromium are suitable options for nickel alloy components to provide a broad range of corrosion protection for systems encountered in commercial practice under both oxidizing and reducing conditions [8].

As an example of the enhanced corrosion protection of molybdenum addition to an alloy, in 1986, a North America nuclear power plant equipped the service water piping system with INCO alloy 25-6MO stainless steel [13]. The 25-6MO alloy replaced the 304 and 316 alloys previously used [13]. It was found that 6% molybdenum added to the stainless steel piping used in the nuclear power plant, where the water supply contained high chloride water fed as an open loop, resulted in an extended service life twice that of the normal time frame previously reported by inspection cycles [13].

The typical chemical composition of stainless steel grade 304 (UNS No. S30400) is 18% Cr, 9% Ni; type 316 (UNS No. S31600) is 2% Mo, 17% Cr, 11% Ni; INCO alloy 25-6MO (UNS No. N08926) is 6% Mo, 20% Cr, 24% Ni, 0.2% N and 0.75% Cu, balance % of all alloys being iron [13]. The service temperature ranges from 32°F (0°C) to 85°F (28°C) for these alloys. Type 316 was previously used as it could commonly resist water containing chloride ions up to 1000 ppm at a flow rate of 3ft (1m)/sec until the next maintenance cycle. By actual applications, it was estimated that 25-6MO stainless steel could potentially extended to three or four times the normal operational time frame as compared to Type 316 [13]. The plants equipped with 25-6MO stainless steel could save over $1.2 million in maintenance and inspection costs and over 1200 staff hours every eighteen months [13]. Ultimately, they could omit every other inspection cycle, now performing the inspection only every 36 months [13].

4.3.4.1 Role of Molybdenum in Passive Film

Molybdenum is one of the most promising elements included in alloys leading to improvement against pitting corrosion. In order to enhance the properties of the passive film the incorporation of molybdenum into stainless steel alloys is proposed to (1) increase the thickness of the passive film, (2) allow stronger bonding within the metal oxide film, (3) reduce the vacancy concentration of the passive film by forming vacancy-solute complexes and (4) increase the rate of passive film formation growth [14]. According to the pH-potential diagram of M. Pourbaix (Figure 4.9a and 3.9b), at applicable pH, the oxide films can approximate the metal in equilibrium with the electrolyte.

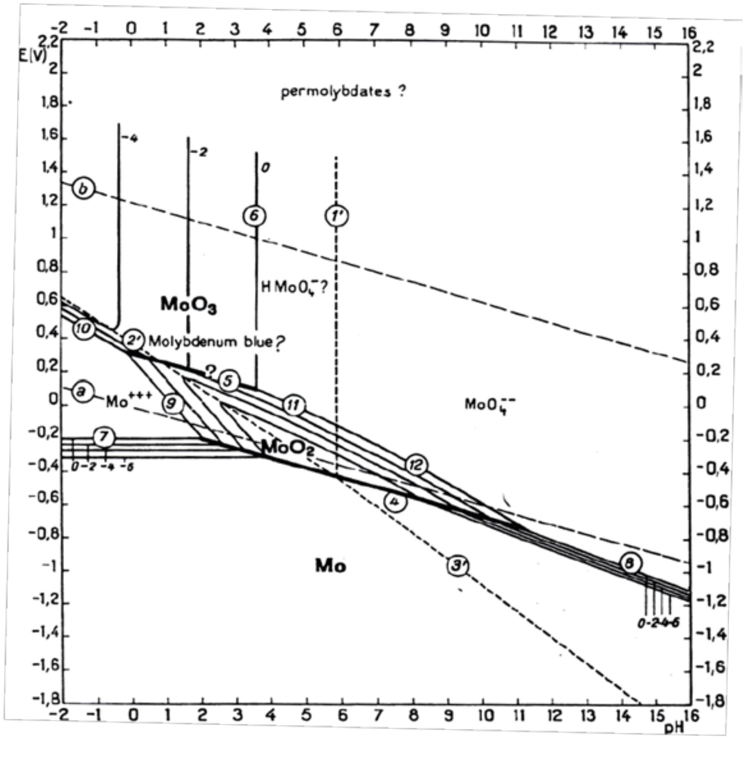

a: Molybdenum and nickel in water [16].

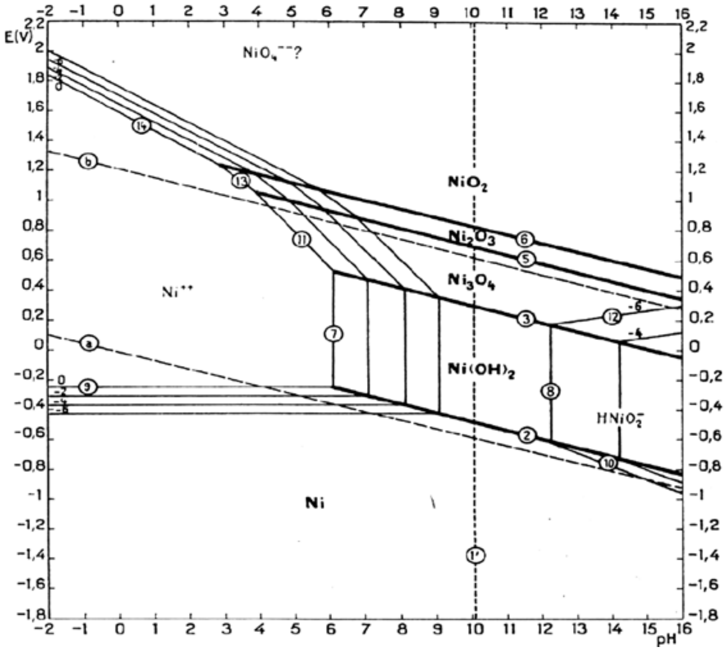

b: Nickel in water [16].

Figure 4.9: M. Pourbaix pH-potential diagrams

Molybdenum is most stable in the form of a metal oxide with various oxidation states and under a range of pH values. When molybdenum alloys are exposed in water and aqueous solutions, they form several oxidation states of molybdenum oxide in the passive film. Molybdenum in a hexavalent state can form in both cationic and anionic states, known as molybdenum trioxide and ferrous molybdate, respectively. Molybdenum can also form in a quadrivalent state as molybdenum dixoide and oxyhydroxide. Most studies agree that Mo(IV) exists in the inner region of the passive film, whereas Mo(VI) is present in the outer layer [14, 15]. The outer layer is defined as the salt precipitated layer or an extension of the barrier layer. However, molybdenum in the passive oxide layers may dissolve at a high rate when exposed to strongly acidic electrolytes, resulting in the dissolution of the free metal in the form of Mo(III).

R. C. Newman (1985) reported that 2.7% molybdenum in the steel FeCrNi alloy lowered the current density as compared to the alloy without molybdenum when polarized in a chloride media [14-15]. Molybdenum was found to influence the corrosion behavior of the alloy through ennoblement of the anodic dissolution reaction in the pit area [14-15]. The pitting dissolution was exhibited as the anodic polarized current [14-15]. Additionally, molybdenum is able to recover from pitting or decrease the dissolution rate by forming and retaining molybdenum oxyhydroxide or molybdate (MoO_2) at the active surface sites [12, 24]. The increase in molybdenum addition to stainless steel impressively reduced pitting corrosion in the presence of chromium [12, 17-20]. It was shown that molybdenum in the form of molybdate was enriched at the surface of the active region instead of the inner layer of the passive film [12,14,15]. Molybdate acts as an adsorbing agent on the surface blocking active sites in the active dissolution area [14-15]. Consequently, molybdenum ennobles the pitting dissolution kinetics while decreasing the pit current density of anodic polarization [14,15,18,19,20,24]. MoO_2 is the most common molybdenum species in the passive region according to the Pourbaix diagram (Figure 4.9a). Molybdenum directly migrated to the passive region, increasing stability and extending passive film thickness [14,15].

4.4 Corrosion Measurements

4.4.1 Tafel Polarization

Corrosion phenomenon is an electrochemical reaction which can be determined by electrochemical techniques. The measurements of the current in relation to the electrode potential give the information to predict a corrosion rate of the coatings within a specific environment. Metal film electrode is polarized by applying an external potential away from equilibrium to monitor corrosion potential and current potential. At the corrosion potential, the rate of metal dissolution is identical to the rate of hydrogen evolution. The deviation from an equilibrium potential is called polarization [3]. The polarization resistance (R_p) is experimentally observed between the electrochemical current density and applied potential for the corroding electrode within a few millivolts of the polarization from the open circuit potential (E_{ocp}) [3]. The Tafel constants including anodic beta coefficient (β_a) and cathodic beta coefficient (β_c) are obtained from the anodic and cathodic slope, respectively [3]. The E_{corr} and i_{corr} were determined from the intercepts by Tafel's extrapolation method as shown in figure 4.10. R_p value is obtained by substituting the β_a, β_c and i_{corr} values into a simplified rearranged Stern and Geary equation. The corrosion rate is inversely proportional to the polarization resistance [3].

$$R_p = \frac{(\beta_a \beta_c)}{2.303\ i_{Corr}(\beta_a + \beta_c)} \qquad \text{Eq. (3.15)}$$

where

R_p is the polarization resistance,
i_{corr} is the corrosion current,
β_a and β_c are the anodic and cathodic Tafel slopes, respectively.

An EG&G PAR Potentiostat/Galvanostat Model 273A was used for corrosion studies. Corrosion behavior was studied by electrochemical techniques. A three- electrode electrochemical cell was used [27]. The corrosion testing system was comprised of the working electrode of the alloy film, two graphite rods (counter electrodes), and a saturated calomel electrode (SCE, reference electrode) The Tafel plot and potentiodynamic polarization measurements were performed in a 3.5% sodium chloride solution. A potential was applied to the cell without stirring the solution and the resulting current density was measured. For Tafel polarization, each scan started from open circuit potential (E_{ocp}) to the cathodic potential and anodic potential, respectively, in range of ±150 mV/SCE with a scan rate of 1 mV/s. In each scan for the potentiodynamic polarization to obtain the passivation region of the nickel-layered and nickel-molybdenum-layered silicate, the run started from open circuit potential (E_{ocp}) to the anodic potential of 0.5 V/SCE with a scan rate of 1 mV/s.

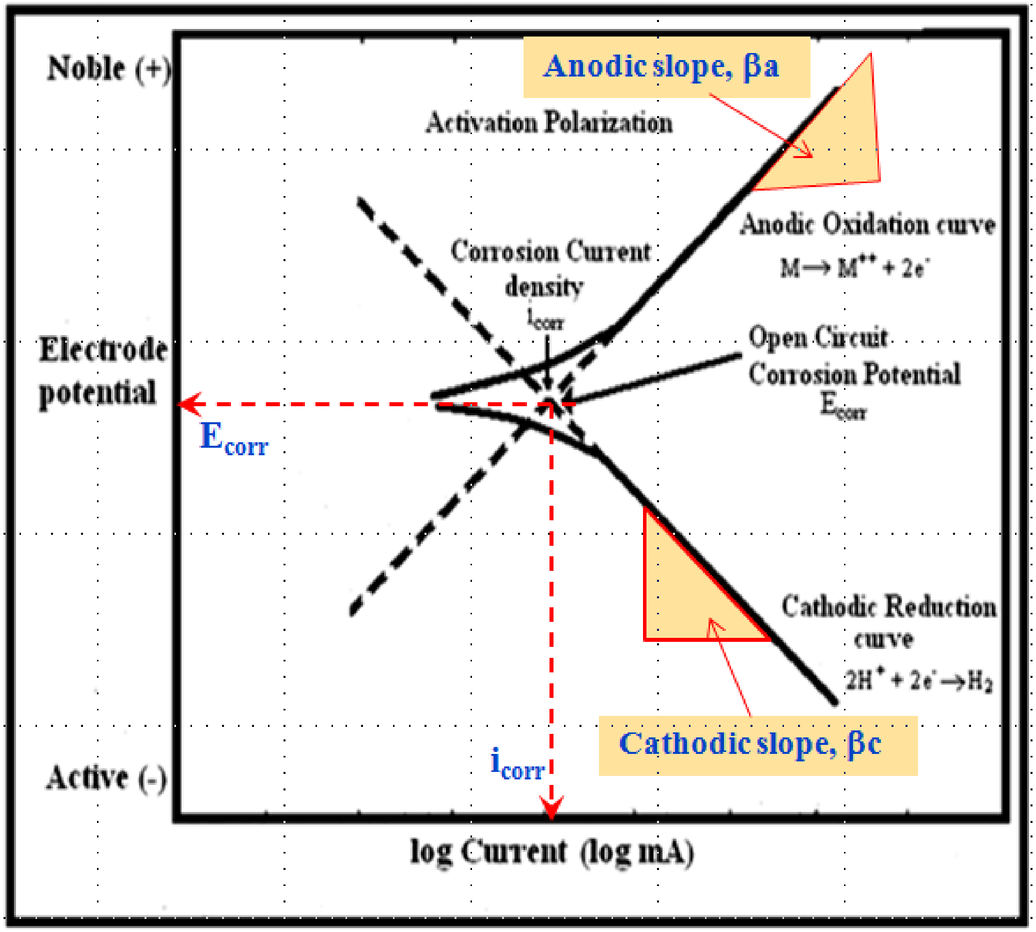

Figure 4.10: Tafel extrapolation plots.

Corrosion tests of the electrodeposited samples from Watt’s bath were performed using Gamry 600 potentiostat/galvanostat. The potentiodynamic polarization studies have been configured into a three-electrode cell consisting of the coating as a working electrode, Pt gauze as a counter electrode and SCE as a reference electrode. The potentiodynamic scan was carried out in the range –250 mV to + 250 mV versus the open-circuit potential with a scan rate of 1 mV s^{-1} in naturally aerated solutions at room temperature 293K. The electrochemical impedance spectroscopy (EIS) investigations were carried out using input signal 10 mV peak to peak in the frequency domain 0.1-10^5 Hz. Corrosion tests of nickel and nickel-layered siliate nanocomposite coatings were carried out in simulated sea water with composition of Burkhoder’s formulation B [28].

4.4.2 Electrochemical Impedance Spectroscopy (EIS)

Electrochemical impedance is usually measured by applying an AC potential to an electrochemical cell and measuring the current through the cell [3]. Equivalent circuit modeling of EIS is used to explain the experimental impedances in terms of mathematical functions to obtain good fit between the calculated impedance and experimental impedance [3]. A value of resistance and capacitance for the coating can be elucidated through modeling of electrochemical data. The modeling procedure uses electrical circuits built from components such as resistors (R), capacitors (C), and inductors (L) to represent the electrochemical behavior of the coating. The resistors represent the bulk resistance of material to charge transport such as the resistance of the solution to ion transport or the resistance of a conductor to electron transport [3]. They are also used to represent the resistance to the charge transfer process at the electrode surface. Capacitors are related to space-charge polarization regions such as the electrochemical double layer [3]. Inductors are associated with the adsorption-desorption processes at the electrode. The specialized circuit elements which used to represent the response of real-world systems include constant phase element (CPE) and Warburg element (Zw) [3]. The Warburg elements are typically used to describe the diffusion and mass transport impedance of the electrode. Many different conditions involved with electrode parameters such as porous electrodes, nonlinear diffusion, or nonhomogeneous materials can be represented as CPE [3]. The most common model is Randles cell model including solution resistance, a double layer capacitor and a charge transfer or polarization resistance. The Nyquist plot for common Randles cell model is basically a semicircle

[3]. The solution resistance can be found by reading the real axis value at the high frequency intercept. This is the intercept near the origin of the plot. The real axis value at the other (low frequency) intercept is the sum of the polarization resistance and the solution resistance [3]. The diameter of the semicircle is therefore equal to the polarization resistance.

In general, when a small potential is applied, electrochemical impedance spectroscopy (EIS) uses the impedance frequency response of a corroding system, to generate a plot of magnitude of the real impedance against the imaginary impedance component [3]. This is known as the complex plane plot or Nyquist plot. The impedance is generated in real and imaginary format according to the equation [3]:

$$Z = R - jX \qquad \text{..Eq. (3.16)}$$

where

Z is the impedance response,
R is the real impedance,
X is the magnitude of the imaginary component, and
j is a complex number equivalent to the square root of (-1).

Data from the Nyquist plots are fitted by the EIS software to generate the equivalent electrical circuits (EEC) which approximates the physical phenomena occurring on the working electrode surface during corrosion.

All the electrochemical impedance technique was performed by using Bio-Logic Potentiostat/Galvanostat equipped with a software EC-Lab version 10.2. Tests were carried out into three-electrode cell (where the coating layer acts as working electrode). The electrodes were immersed in 3.5% NaCl solution at a constant temperature of 293k. For the impedance measurements, an input signal of 10 mV peak to peak was applied in the frequency domain of 0.1-10^5 Hz.

4.5 Chapter References

[1] J.C. Scully, *The Fundamentals of Corrosion*, 2nd Ed., Pergamon Press Ltd.: New York, 1975.

[2] S.Shah, *Surface and Interface Characterizattion in Corrosion*, NACE International: Texas, 1994.

[3] N Ekekwe, *Electrochemical Impedance Spectroscopy: Corrosion Behavior Application: Theory, Modeling, and Experimentation*, Ed., VDM Verlag Dr. Muller Aktiengesellschaft & Co. KG : Germany:, 2009.

[4] M. Nunez, *Prevention of Metal Corrosion: New Research*, Ed., Navo Science Publishers, Inc.: New York, 2007.

[5] A.J. Sedriks, *Corrosion of Stainless Steels*, 2nd Ed., 1996.

[6] G.S. Frankel, *Journal of the Electrochemical Society*, **1998**, 145, 2186-2198.

[7] J.C. Scully, *The Fundamentals of Corrosion*, 2nd Ed., Pergamon Press, Oxford: New York, 1975.

[8] W.Z. Friend, *Corrosion of nickel and nickel-base alloys*. Willey-Interscience.: New York:

1980.

[9] Haubold, T., Bohn, R., Birringer, R., Gleiter, H, *Materials Science and Engineering: A*, **1992**, 153(1–2), 679–683.

[10] K. Orgass, H.W. Schock, J.H. Warner, *Thin Solid Films*. **2003**, 431-432

[11] H. Khatri, S. Marsillac, *J. Phys. Condens. Matter*. **2008**, 20, 0555206, 1-5.

[12] Y.C. Lu, M.B. Ives, C.R. Clayton, *Corrosion Science*, 35(1-4), 1993, 89-96.

[13] News Letter, International Molybdenum Association, London, UK. July 2000, 1-9.

[14] R.C. Newman, *Corrosion Science*. **1985**, 25(5), 331–339.

[15] R.C. Newman, *Corrosion Science*. **1985**, 25(5), 341–350.

[16] M. Pourbaix, *Atlas of Electrochemical Equilibria in Aqueous Solutions, NACE International Cebelcor*, National Association of Corrosion Engineers, 2nd Ed., Texas, 1974.

[17] B.E. Clark, Thorpe, S.J., Aust, K.T., *Corrosion Science*. **1990**, 31, 551–556.

[18 A. P. Bond, E.A., *J. Electrochem. Soc*. **1968**, 115(11), 1130-1135

[19] W. R. Cieslak, D. J. Duquette, *J. Electrochem. Soc*. **1985,** 132(3), 533-537.

[20] G. S. Frankel, *Journal of the Electrochemical Society*. **1998**, 145, 2186-2198.

[21] M. Nunez, *Prevention of Metal Corrosion: New Research*, Nova Science Publishers, Inc.: New York: 2007.

[22] A.J. Sedriks, *Corrosion of Stainless Steels*, 2nd Ed., John Wiley & Sons, Inc.: New York: 1996.

[23] M. Nunez, *Metal Electrodeposition*, NewYork: Nova Science Publishers, Inc., 2005.

[24] G.O. Ilevbare, G.T. Burstein, *Corrosion Science*. **2001**, 43(3), 485-513.

[25] C. Donik, A. Kocijan, D. Mandrno, I. Paulin,, M. Jenko, B. Pihlar, *Applied Surface Science*. **2009**, 255(15), 7056-7061.

[26] I. Olefjord, B. Brox, U. Jelvestam, *Journal of the Electrochemical Society*. **1985**, 132(12), 2854-2861.

[27] Designation: G59-97, Standard test method for conducting potentiodynamic polarization resistance measurements, *ASTM International*, 2009, 1-4, http://enterprise1.astm.org/download/G59.1090230-1.pdf

[28] P. J. Bidwell,, S. Spotte, *Simulated Seawaters: Formulas and Methods*. Jones and Bartlett Publishers: Boston, 1985.

CHAPTER 5

NICKEL AND NICKEL/LAYERED SILICATE NANOCOMPOSITE COATINGS

5.1 Influence of Acidic pH on Electrodeposition of Nickel-Layered Silicate Nanocomposites for Corrosion Protection

5.1.1 Introduction

A steady demand for enhanced coatings at a reduced cost has been the main focus in the area of corrosion for many years. Degradation of the coatings takes place because of unfavorable environmental conditions that lead to many types of corrosion [1–4]. Since it is difficult to completely stop corrosion, the best economical idea is to simply reduce the rate at which it occurs [5]. Low cost, convenience, and the ability to work at low temperatures have made electrodeposition one of the more favorable techniques to synthesize coatings [6]. The applied potential, pH, temperature, and current all play a role in determining the morphology, structure, and composition of the coatings [7-9]. One metal commonly used to enhance corrosion resistance is nickel because of its high abundance and capability to protect against common corrosion [1–4]. Nevertheless, corrosion resistance from metal coatings tends to be unsuccessful because of reduced mechanical properties. Forming alloys, with metals such as zinc, is one possibility to increase corrosion resistance [8]. Alloyed coatings tend to enhance the corrosion resistance properties but possess mechanical properties that are comparable to the individual metals. Ceramic fortification into the metal coatings can improve mechanical properties. To increase the hardness and life of nickel coatings, different nanoparticles such as TiO_2, CeO_2, SiC, andAl_2O_3 have been integrated into the matrix of the coating [10-15]. The ceramic compounds that are being investigated for this study are layered silicates, which possess many advantageous properties such as a high surface area, good chemical resistance, resistance to extreme temperatures, and resistance to pH. In previous studies, the incorporation of the layered silicates into polymers [6, 16, 17] and ceramics

[3, 18] to form composites resulted in enhanced mechanical properties. In the case of conductive polymer composite coatings, scientists have shown that layered silicates increased the resistance to corrosion in the films [19, 20]. The incorporation of the layered silicates into the metal matrix should prove to be fruitful for enhanced resistance to corrosion and hardness in the nanocomposite coating.

In this work, nickel-layered silicate nanocomposite films were electrochemically deposited using pulsed potentiostatic conditions from an acidic plating bath containing exfoliated layered silicate to enhance adhesion to the substrate, corrosion resistance, and mechanical properties. Scanning electron microscopy (SEM) was chosen to analyze the morphology of the electrodeposited films. X-ray diffraction (XRD) was used to analyze the crystal structure of the films. The corrosion resistance and hardness of the nanocomposite films were compared with each bath condition using Tafel polarization, immersion tests, and nanoindentation. The pH of the plating solution was varied by adding different amounts of sodium citrate and citric acid. The citrate ligand was used to stabilize nickel ions in the plating solution. Viscosity, conductivity, zeta potential, and particle size were all measured for the effect of the addition of montmorillonite to the plating solution.

5.1.2 Experimental

5.1.3 Materials

Nickel-layered silicates were electrochemically deposited from acidic plating baths at pH 1.6, 2.5, and 3.0 at 25^{o}C. The montmorillonite (MMT) (5 g/L) aqueous solution from Southern Clay Products was mechanically agitated using a magnetic stirrer over 24 hours to obtain exfoliated layered silicate platelets. Citric acid anhydrous ($H_3C_6H_5O_7$) and/or sodium citrate dehydrate ($Na_3C_6H_5O_7 \cdot 2H_2O$) was utilized as a ligand to stabilize nickel (II) ions. The composition of nickel-citrate plating baths at different pHs was prepared from $NiSO_4 \cdot 6H_2O$ (Alfa Aesar) and $Na_3C_6H_5O_7 \cdot 2H_2O$ (Fisher Scientific) or $H_3C_6H_5O_7$ (Fisher Scientific) as shown in table 5.1. The nickel and citrate salts were added to the exfoliated MMT solution and then stirred with a magnetic stirrer until dissolved. The pH of the plating solution was measured with a Corning pH meter and Pasco Scientific pH electrode. The electrochemical cell was comprised of three electrodes: stainless steel disc (working electrode), chromel wire (counter electrode), and saturated calomel (reference electrode). Stainless steel discs with an area of 1.8 cm^2 were polished mechanically with 600, 800, and 1000 grit silicon carbide paper and then with 3 and 1 μm diamond solution on felt cloth. After the electrode was polished to a mirror-like finish, it was sonicated in deionized water for 10 minutes.

Table 5.1: Values of the acidic plating bath composition for nickel, citrate, and citric acid.

Chemical	**pH 1.6**	**pH 2.5**	**pH 3.0**
$NiSO_4 \cdot 6H_2O$	77.8 g/L	77.8 g/L	77.8 g/L
$Na_3C_6H_5O_7 \cdot 2H_2O$	-	35.3 g/L	52.9 g/L
$H_3C_6H_5O_7$	57.6 g/L	34.6 g/L	23.0 g/L

5.1.4 Results and Discussion

5.1.4.1 Kinematic Viscosity

The layered silicate was stirred over 24 hours resulting in exfoliated montmorillonite (MMT) platelets. A certain amount of anionic exfoliated MMT was able to suspend in the aqueous solution forming an equilibrium of the individual particle repulsions. If the MMT concentration is too high, agglomeration and precipitation occur, resulting in an increase of viscosity. The optimum amount of MMT is chosen from viscosity based on the kinematic viscosity curve (Figure 5.1).

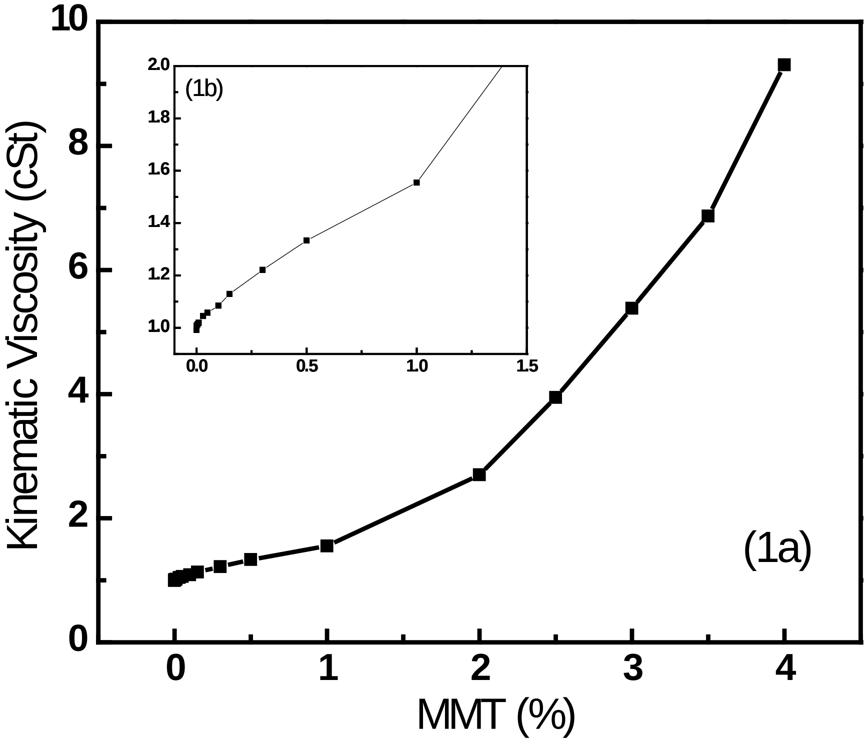

Figure 5.1: Kinematic viscosity of montmorillonite (MMT) solutions.

The exfoliated MMT are nonspherical particles; thus, the rotary Brownian motion may lead to non-Newtonian effect even in a diluted solution. The addition of more MMT particles changes the magnitude of the kinematic viscosity because of its platelet shape and charged surface, which results in a deviation of Newtonian behavior [21]. According to figure 5.1(b), the viscosity of the MMT solution gradually increased until 0.5%MMT. Then the viscosity started to dramatically increase when MMT was higher than 1% as seen from the steep increase of the slope. The viscosity increase is linear at very low concentration ranges. The kinematic viscosity values for the concentrations of 0.5% MMT was 1.33 cSt at 25°C. The MMT concentration of 0.5% is selected to be used in the nickel plating solution because the viscosity stays stable at about this concentration. When introducing an exfoliated MMT into the nickel solution, it becomes a thickened fluid because the opposite charge of nickel ions are electrostatically adsorbed onto the clay surface (negatively-charged) leading to agglomeration of the particles. Once citrate ions are added into the nickel-MMT solution, the viscosity decreases because citrate ligands help stabilize nickel ions in the solution. However, the viscosity of Ni-citrate in MMT solution is still higher than that of only Ni-citrate solution because free nickel cations are able to be adsorbed onto the MMT surface.

5.1.4.2 Zeta Potential and Particle Size

As shown previously, typically the surface forces can be the key factor for incorporation of particles into a metal matrix during electrodeposition [22]. The zeta potential of layered silicate nanoparticles were measured at three different pHs (1.6, 2.5, and 3.0). In order to investigate the influence of the bath composition and pH, the zeta potential of each condition was analyzed for particle stability (Table 5.2). The zeta potential of the charged particles helps predict colloidal stability and electrostatic interaction of the particles. The zeta potential represents the repulsive forces between particles. Because most aqueous colloidal systems are stabilized by electrostatic repulsion, the larger repulsive forces between particles resulted in the particles being stabilized in solution, which reduces the possibility for the particles to aggregate. The exfoliated MMT is known to have a negative charge on its surface [23]. The exfoliated MMT (0.5%) solution has a zeta potential of −43.2mV. It is stable and able to suspend in the aqueous solution while the nonexfoliated MMT precipitates. Based on the results from the zeta-potential analysis of the nickel-citrate-MMT plating solution, pH 2.5 (−22.2mV) and pH 3.0 (−21.9mV) solutions are more stable than pH 1.6 (−10.1mV) solution (Table 5.2).

Table 5.2: Plating solution measurements of conductivity, viscosity, zeta potential, and particle size for various pHs (1.6, 2.5, 3.0) of the plating bath.

Plating solution pH	**Conductivity (n=3) (mS/cm)**	**Viscosity (n=3) (cSt)**	**Particle size (nm)**	**Zeta potential (n=3) (mV)**
pH 1.6	24.3 ± 0.1	2.86 ± 0.03	3120	-10.1 ± 0.3
pH 2.5	28.1 ± 0.2	2.64 ± 0.006	2756	-22.2 ± 0.9
pH 3.0	33.7 ± 0.3	2.21 ± 0.008	2517	-21.9 ± 0.4
0.5% MMT	0.502 ± 0.008	1.33 ± 0.003	591	-43.2 ± 0.8

The adsorption of the nickel and citrate at the MMT surface shifted the zeta potential toward positive values dropping the electrostatic stabilization of the dispersion. However, the particles at pH 2.5, and pH 3.0 are much more stable than that at pH 1.6. This was also confirmed by allowing the solution to sit stagnant for 24 hours in which time the pH 1.6 solution precipitated out, whereas the pH 2.5 and 3.0 stayed stable in solution for 3-4 more days. In addition, the particle's size decreased as pH increased (Table 5.2). The particle size of 0.5% MMT in water is 591 nm. When the MMT concentration is introduced to the nickel plating bath, the particle size becomes larger than the native MMT particles. A slight change was observed from 3120 to 2517 nm as the pH increased, which follows the decrease in viscosity as pH increases (Table 5.2). At pH 1.6, mostly free Ni^{2+} ions are present to adsorb to the surface of the MMT, whereas at the higher pH values of 2.5 and 3.0 a nickel-citrate complex (NiHCit) is formed removing some of the free Ni^{2+} ions that could bind to MMT [24]. This follows the result where the particle size and viscosity decrease as the pH is increased from 1.6 to 3.0.4.1.3.3 Cyclic Voltammetry

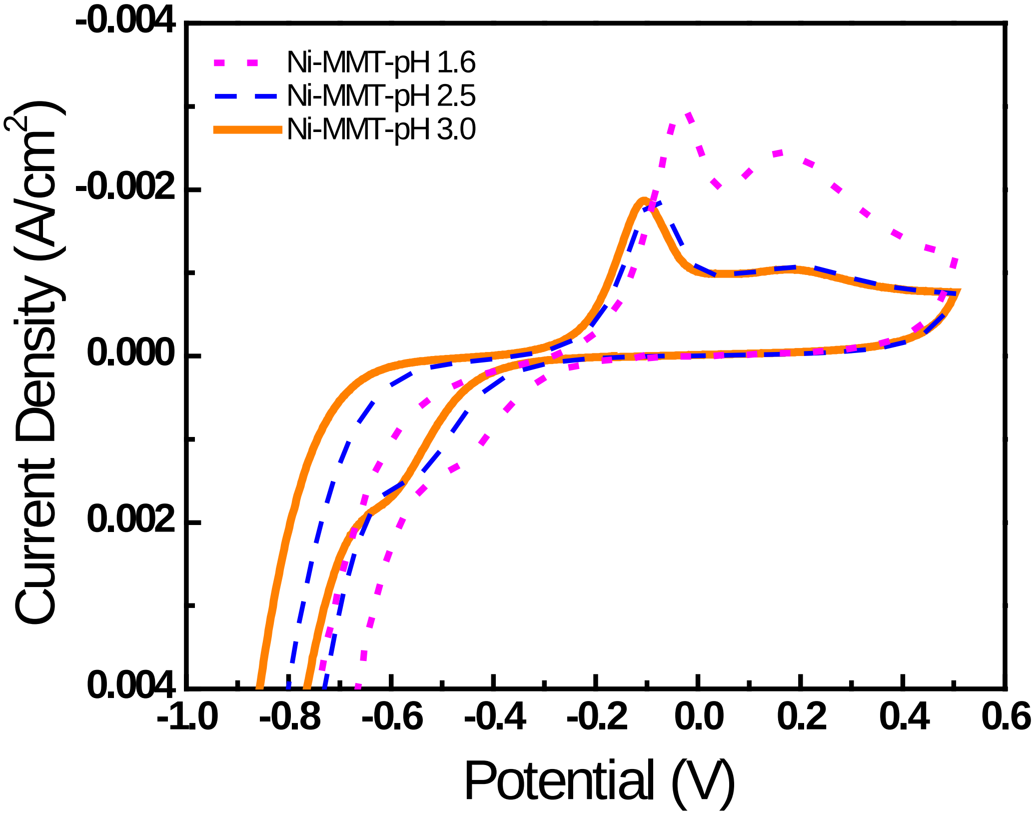

Figure 5.2: Cyclic voltammograms of nickel-layered silicate (0.5% MMT) plating solution for various pHs (1.6, 2.5, and 3.0).

Cyclic voltammetry (CV) was run for the nickel-layered silicate plating solutions at pHs of 1.6, 2.5, and 3.0 and shown in figure 5.2. The pH influences the electrodeposition of Ni-MMT. The reduction peak for Ni-MMT at pH 3.0 is shifted to a more cathodic potential (−0.6V). Also the working window of the electrodeposition was expanded at pH 3.0, pushing the hydrogen evolution further cathodic and resulting in smoother films (Figure 5.2) [25]. The nickel-citrate species varied with respect to pH values [25]. For a nickel-citrate bath at pH less than 4, the predominant species is NiCitH with trace amount of NiH_2Cit^+ (less than 2%). At pH lower than 2, most of the nickel exists as free nickel ions; as the pH increases from 2 to 3, the nickel-citrate species are mostly represented as NiCitH and NiH_2Cit^+, with less free nickel ions [25-27]. MMT improves adhesion and provides for a smoother film because the nonelectroactive platelets slow down the reduction reaction and push hydrogen evolution more cathodic (as seen in the cyclic voltammetry, figure 5.2). Also the nickel films without MMT at these pHs tended to have poor adhesion. The pH 3 nanocomposite film was the optimal coating giving the best results of overall properties for adhesion, corrosion protection and mechanical properties.

5.1.4.3 Film Characterization

The pH also affects nickel crystalline growth as shown by SEM (figure 5.3) and XRD (figure 5.4). At very low pH there is more hydrogen formation and the plating rate is faster resulting in a non-uniform film and larger grain size. At pH of 2.5 and 3.0 the rate of electrodeposition is slower and hydrogen evolution decreases resulting in smoother uniform films and longer deposition time for the same accumulated charges. Pulse electrodeposition is applied for depositing the nickel-MMT films at low pH (1.6–3.0). Through experiments, it was determined that the electrodeposition of nickel at pH values greater than 3.5 tended to have poor adhesion that required other pretreatment of the stainless steel substrate or a different plating bath for adhesion of the coating. By pulsing, there is an increase in the replenishment of nickel cations in the diffusion layer and diffusion of hydrogen away from the electrode surface [4, 8]. Also, the pulse deposition method provided a uniform, smooth film with good adhesion. A direct potential method was attempted but it was found that the films deposited in a non-uniform manner and had poor adhesion. SEM micrographs of the deposits show microstructures with grain sizes in the micrometer range.

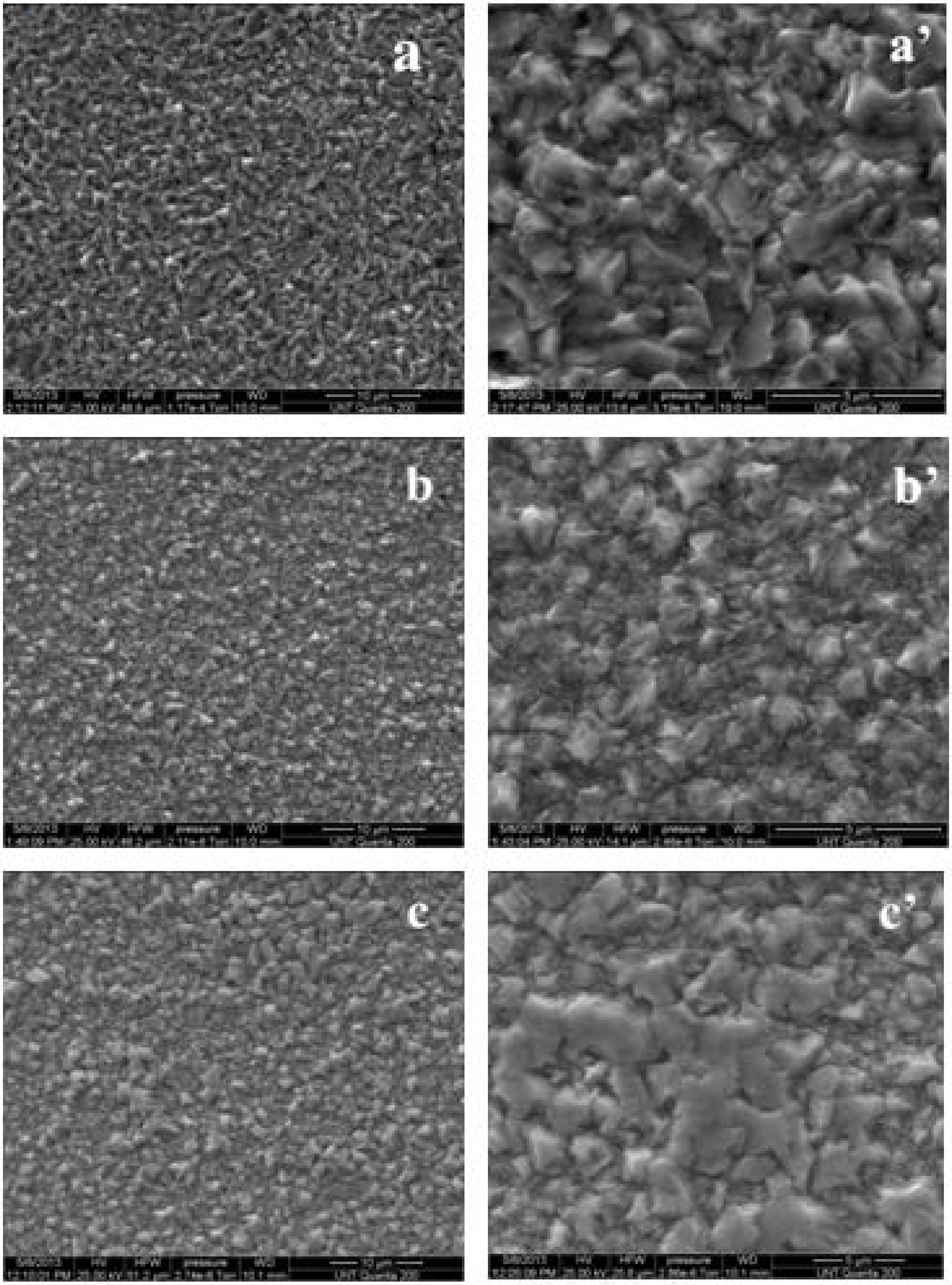

Figure 5.3: Scanning electron microscopy (SEM) images of Ni-MMT (0.5%) films electrodeposited from plating baths at pHs 1.6 ((a) and (a’)), 2.5 ((b) and (b’)), and 3.0 ((c) and (c’)).

However, it is clear from Figure 5.3 that at pH 3.0 there is a progressive change in the crystal orientation from an almost random texture to a stronger (200) texture. This may be due to the stronger nickel-citrate chelate NiHCit formation at pH 3.0, which stabilizes the nickel in solution and allows for slower dissolution at the electrode surface. This truncation of the pyramidal grains (observed for pH 1.6 and 2.5) occurs for pH 3.0 (Figure 5.3) which would support the enhanced (200) texture of the pH 3.0 deposits. The Ni-MMT films fabricated at pH 1.6 are crystalline and give a random XRD pattern that matches the PDF no. 00-004-0850 for nickel (Figure 5.4). When pH of the plating bath is increased to 2.5 and 3.0, Ni-MMT films start to show an orientation preference for (200) growth. An electrostatic stabilization of dispersion of the nickel-citrate-MMT particles benefits insertion of MMT into the nickel electrodeposited films. The nanoindentation results also support that the hardness is highest for coatings deposited at pH 3.0 (234 GPa) over that of coatings deposited at pH 1.6 and 2.5 (Table 5.3).

Table 5.3: Nanoindentation hardness and young modulus of the Ni-MMT (0.5%) nanocomposite films electrodeposited at various pHs (1.6, 2.5, and 3.0).

Ni-MMT coatings pHs	**Young modulus (GPa ± SD, n=25)**	**Nanoindentation hardness (GPa ± SD, n=25)**
pH 1.6	147.2 ± 50.4	4.1 ± 1.5
pH 2.5	173.5 ± 52.3	3.3 ± 1.2
pH 3.0	233.9 ± 56.5	5.3 ± 1.6

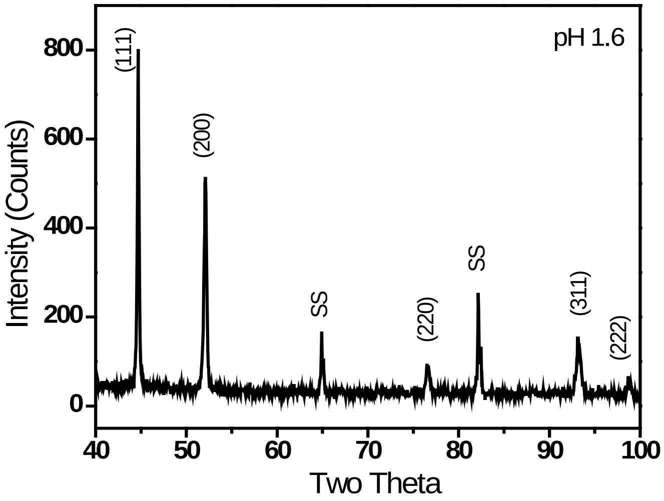

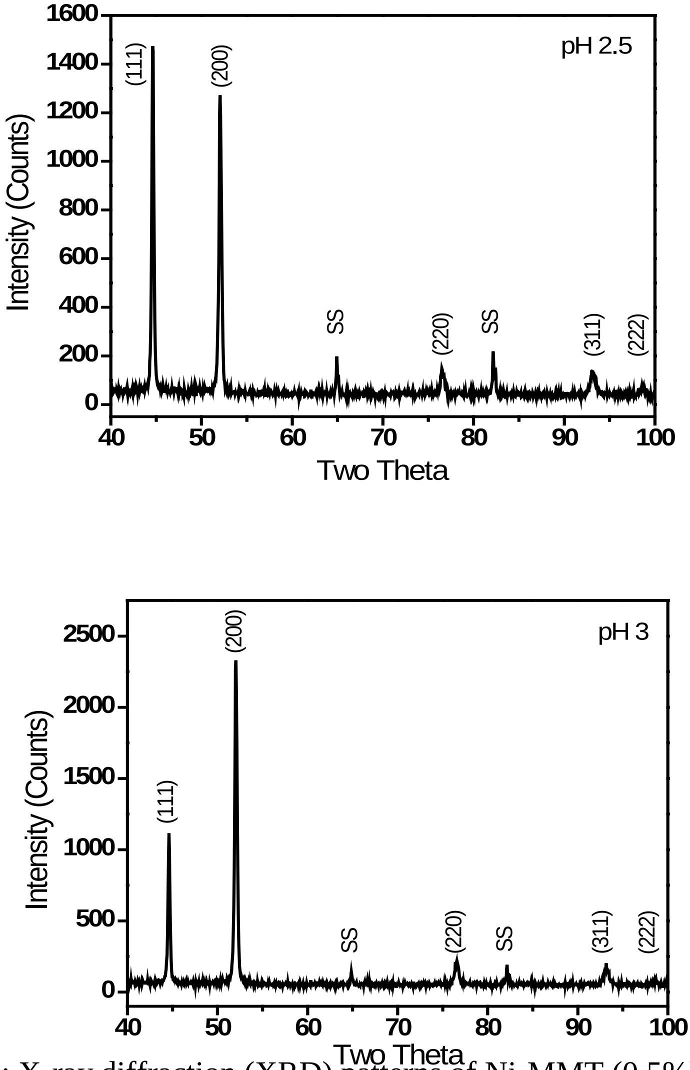

Figure 5.4: X-ray diffraction (XRD) patterns of Ni-MMT (0.5%) films electrodeposited at various pHs (a) 1.6, (b) 2.5 and (c) 3.0 (SS: substrate stainless steel peaks).

5.1.4.4 Corrosion Studies.

The electrochemical corrosion parameters from the Tafel data (Figure 5.5) are summarized in table 5.4. However, the film fabricated from pH 3 exhibited a passive region (plateau region) with a higher anodic potential of the polarization (Figure 5.5). The corrosion parameters, (R_p, E_{corr}, and i_{corr}), are all within the same range for pH 1.6, 2.5, and 3.0 (Table 5.4). The corrosion potential of the films decreases from −0.32, −0.34, and −0.39V for different pHs of 1.6, 2.5, and 3.0, respectively, while the corrosion rate improves for the pH 3.0 coating.

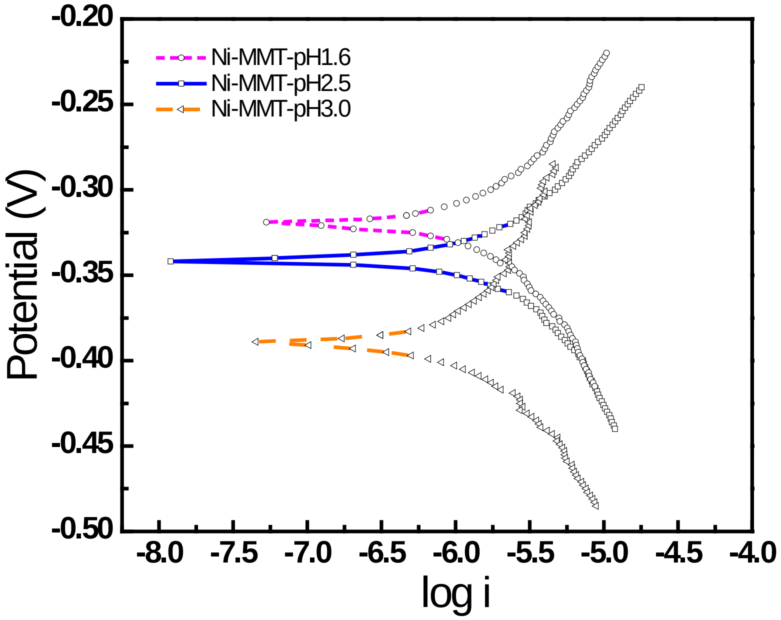

Figure 5.5: Tafel plot of Ni-MMT (0.5%) films measured in 3.5% NaCl solution at 25°C. Coatings were electrodeposited from a plating solution at various pHs (1.6, 2.5, and 3.0) onto stainless steel substrates.

Table 5.4: E_{corr}, i_{corr} and polarization resistance (R_p) of the Ni-MMT (0.5%) nanocomposite film electrodeposited at various pHs (1.6 to 3.0) of the plating bath.

Ni-MMT coating deposited at	**E_{corr} (V) ± SD (n=3)**	**i_{corr} (A·cm^{-2}) ± SD (n=3)**	**Rp (kΩ·cm^2) ± SD (n=3)**
pH 1.6	-0.32 ± 0.02	9.02 ± 3 x 10^{-7}	147
pH 2.5	-0.34 ± 0.02	9.48 ± 3 x 10^{-7}	184
pH 3.0	-0.39 ± 0.02	7.34 ± 2 x 10^{-7}	116

The immersion corrosion tests were conducted at ambient temperature to monitor OCP values for 30 days (Figure 5.6). The films deposited at pH 3 showed the greatest improvement in corrosion protection taking 13 days to reach the OCP of stainless steel. The coatings deposited at pH 1.6 began to corrode within a day based on the immersion OCP values matching stainless steel. The immersion test was run three times for each of the pHs and the average was taken to create figure 5.6 with an overall standard deviation of ±0.02. Figure 5.7 shows the coatings at pH 1.6, 2.5, and 3.0 before and after 30 days of immersion in 3.5% NaCl. At pH 1.6, corrosion is visible for the coating (Figure 5.7(d)), whereas pH 2.5 just starts to show corrosion effects at the edges of the substrate (Figure 5.7(e)). The coating at pH 3.0 still shows no visible corrosion at 30 days and is the most stable of the coatings.

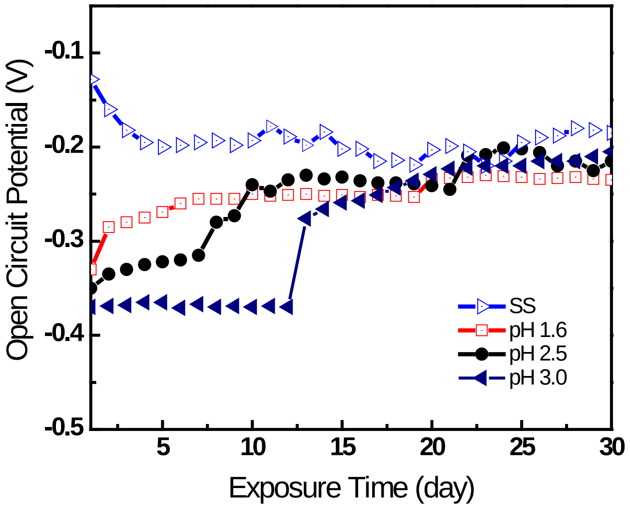

Figure 5.6: Open circuit potential (OCP) versus immersion time in 3.5% NaCl for nickel-layered silicate films electrodeposited from various pHs (1.6, 2.5, and 3.0). Values are an average of three runs with a standard deviation of ±0.02.

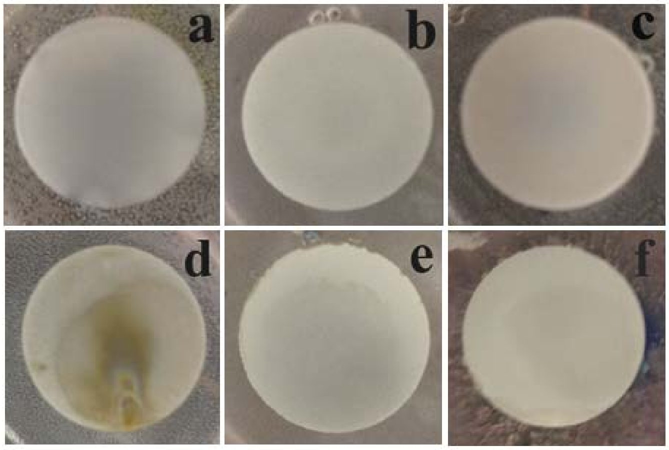

Figure 5.7: Sample images of Ni-MMT coatings electrodeposited from plating baths at various pHs of 1.6, 2.5, and 3.0 before immersion in 3.5% NaCl (a)–(c), and after (d)-(f), respectively.

5.1.5 Conclusion

The optimal bath composition was developed to improve film adhesion to stainless steel, corrosion protection, and mechanical properties. To obtain the stable layered silicate particles for the codeposition with nickel, the viscosity, conductivity, zeta potential, and particle size were analyzed. The particles at pH 2.5 (−22.2 mV) and pH 3.0 (−21.9 mV) were more stable than that at pH 1.6 (−10.1 mV). Corrosion was investigated by Tafel polarization and open circuit potential measurements versus time. XRD determined that the (111)/(200) ratio changed with deposition pH. The SEM and hardness results also supported that the nickel-MMT nanocomposites at pH 2.5 (174 GPa) and 3.0 (234 GPa) were better than at pH 1.6 (147 GPa). From all the combined data, the pH 3.0 coating with incorporated MMT gave the best adherence, hardness, and corrosion protection for the nanocomposite coatings.

5.2 Salt Water Corrosion Resistance of Electrodeposited Nickel-Layered Silicate Nanocomposite Coatings from Watts' Type Solution at Acidic Condition (pH~4-5).

5.2.1 Introduction

For industry, the properties of the materials used should satisfy many requirements. The materials should be light, cheap, and corrosion-resistant and have good mechanical properties including hardness, heat resistance and wear resistance. In most cases these requirements are not fulfilled by a monolithic material, hence the demand for composites in order to cope with severe environments and stresses encountered during operation. Composites have found a large range of applications such as high pressure valves, microelectronics and medical devices in addition to applications in many fields i.e. marine, mining, agriculture and nuclear [28-33].

Many techniques can be used to fabricate composites such as thermal, plasma spraying, physical and chemical vapor deposition [34]. Compared to these methods, electrodeposition has many advantages including low cost, uniform deposition, ease of control, good reproducibility and capability to coat complex geometries [35].

Metal-matrix composites have been produced by modifying the metallic matrix with different types of materials including organic, inorganic and polymers. Recently, the production of metal-ceramic composite coatings has received great interest; especially nickel-based composites due to improved mechanical properties and good wear and corrosion resistance [29, 36-38].

Montmorillonites are layered-silicates that have a smectite structure (2:1 layered structure with a single layer of aluminum octahedral between two layers of silicon tetrahedral). They are hydrated sodium calcium aluminum magnesium silicate hydroxide and can be represented by the formula $(Na,Ca)\ (Al,Mg)_6(Si_4O_{10})_3(OH)_6.nH_2O$. Montmorillonite (MMT) clays have been extensively utilized in many applications including catalytic processes, pharmaceutical preparations, drilling fluids oil recovery and binding formulation as they can impart hardness to materials [39-42].

In the present study, the electrodeposition of nickel-montmorillonite nanocomposite (Ni-MMT) coatings from Watt's type solution using pulse electroplating technique was investigated. Watt bath has been utilized for commercial nickel coatings due to the inexpensive salt of nickel sulfate. Additionally, the deposits produced from Watt solution provide various coating purpose offering both bright and semi-bright nickel [52]. The bright nickel film is typically used for decorative purposes and corrosion protection. Semi-bright deposits are used for engineering nickel where a high shine is not required. The large amount of nickel sulfate (225-400 g/L) used in Watts bath not only raises the limiting cathode current density, but also lowers the resistivity resulting in improving plating distribution. The metal distribution or throwing power is affected by the cathode polarization, cathode efficiency –current density relationship, and electrical conductivity of the plating solution. These factors do not significantly influence the metal distribution of acid nickel plating solutions composed of the simple metal salts such as Watt bath. A small amount of nickel chloride (30-60 g/L) is also used in Watt bath to minimize anode passivity especially at high current densities. The boric acid (30-45 g/L) serves as a weak buffer used to control bath pH, smooth film with low pitted, and produce whiter deposits. The pH in Watts baths range from 0.5 to 5.9 [52]. Sulfuric acid is used to adjust the solution pH. The amount of nickel sulfate or nickel chloride is adjusted corresponding to purposed nickel film. Nickel sulfate salt enhances engineering properties such as hardness while nickel chloride increase current density of the solution and improve film's brightness [52]. The research aims to study the effect of concentration of MMT in the plating bath on the mechanical properties and morphology of the composite coatings. Also, the corrosion behavior of Ni-MMT was compared to that of pure Ni using Tafel polarization and electrochemical impedance spectroscopy.

5.2.2 Experimental

Pure Ni and Ni-MMT composite coatings were electrodeposited from an additive-free Watt's type bath. The electrodeposition experiments were performed under pulse current conditions. The bath composition and electrolysis parameters for the electrodeposition processes are listed in table 5.5. The electrolytic bath was composed of 300 g/l of $NiSO_4.6H_2O$ (BDH), 35 g/l $NiCl_2.6H_2O$ (BDH), 40 g/l H_3BO_3 (Merck) and varying amount of montmorillonite powder swy-1 (Southern Clay Products, Wyoming). All of the electrolytic solutions were prepared using deionized water. Solutions containing MMT were vigorously stirred for 24 hours prior to electrodeposition experiments in order to exfoliate the clay into individual platelets.

Analytical grade copper discs were used as the cathode (area 0.7 cm^2) which were mechanically polished, sonicated for 10 minutes in water and dried in air before immersion in the test solution. During electrodeposition the bath temperature was kept at 50 °C and the initial pH was adjusted to 4.3 by addition of 10% ammonia solution. A nickel sheet of 99.9 % purity (BDH) was used as the anode and a saturated calomel electrode was used as the reference electrode. Electrodeposition of pure Ni and Ni-MMT nanocomposites was carried out under pulse current conditions at a current density of 10 A dm^{-2} using Bio-Logic EC-Lab potentiostat/galvanostat version 10.2.

Table 5.5: The electrodeposition parameters for preparation of pure Ni and Ni-MMT composite coatings.

Solution composition (Electrolyte (Watts' type)	
$NiSO_4.6H_2O$	300 g/L
$NiCl_2.6H_2O$	35 g/L
H_3BO_3	40 g/L
Sodium-rich montmorillonite	1-50 g/L
Electrodeposition conditions	
pH	4.3
Temperature	50 °C
Electrolyte agitation	Magnetic stirring 250 rpm
Cathode	Cu disc (area 0.7 cm^2)
Anode	Ni foil (area 16 cm^2)
Current density	10 A dm^{-2}
Current type	Pulse current (PC)
Duty cycle	25%
Pulse frequency	0.25 Hz

5.2.3 Results and Discussion

5.2.3.1 Effect of MMT concentration on the electrodeposition of Ni-MMT composite

The influence of MMT concentration in the plating bath on the chemical composition of Ni–MMT coating is shown in table 5.6. The incorporated weight percentage of MMT in the composite coating was found to increase in the bath concentration, reaching a maximum at a particle concentration of 30 g/l and then decreased. At higher concentrations than 30 g/l the viscosity of the plating bath greatly increases (Table 5.7) resulting in a decrease in the rate of transfer of MMT particles to the cathode surface and consequently the weight percentage of MMT in the composite coatings decreased.

Table 5.6: The elemental composition of Ni-MMT coating surface at various concentrations of MMT in the plating bath.

MMT concentration in the plating bath (g L^{-1})	**Elemental composition (at %)**		
	Al	**Si**	**Ni**
0.5	0.20	0.43	99.36
5	1.17	1.93	96.44
10	2.19	3.08	94.63
30	2.92	3.62	92.13
50	2.64	3.97	93.61

The embedding of MMT particles in the coating can be attributed to the adsorption of the positively charged suspended particles on the cathode surface during the discharge of Ni^{2+} ions resulting in encapsulating of MMT particles in the growing Ni film on the cathode surface.

The influence of the MMT concentration in the plating solution and the solution stability was studied with conductivity and viscosity measurements as well as particle size and zeta potential analysis (Table 5.7). The MMT particle sizes were determined to be around 517–526 nm in the suspension (1–5 g/l) after pretreatment and exfoliation. There is agglomeration of the platelets in solution however, as the concentration increases; the high concentration samples such as 30 g/l have a particle size of ~1835 nm. The MMT solutions exhibited the same tendency with the viscosity as with particle size, where the higher concentration of 30 g/l gives much higher viscosities, 1299 cSt, than the lower concentrations (1–3 cSt). The exfoliated MMT is known to have a negative charge on its surface. Hence, when the MMT solution is incorporated into the nickel–borate bath, the conductivity of the electrolyte bath slightly decreases since the negative charge starts to neutralize the positive charge of the nickel. The exfoliated MMT at each concentration had a zeta potential of about −41 mV, for 1–30 g/l and then drops to −26 mV at higher concentrations. This decrease in zeta potential for higher concentration MMT solution shows instability of the solution resulting in flocculation. In the presence of the nickel salts, the nickel cations adsorbed onto the surface of the montmorillonite resulting in a positive shift of the zeta potential, which leads to a drop in the electrostatic stabilization of the dispersion. The zeta potential of nickel–borate with montmorillonite (−18.3 mV) at the 5 g/L concentration was the most stabile of the particles in suspension compared to those at the lower (−13.5 mV) and higher concentrations (−1.9 mV).

Table 5.7: Plating solution measurements of conductivity, viscosity, zeta potential, and particle size for various concentrations of MMT.

MMT (g/L)	**Measured solution**	**Viscosity (cSt) (n=5)**	**Conductivity (mS/cm)**	**Particle size (nm)**	**Zeta potential (mV) (n=3)**
1	MMT	0.65 ± 0.01	0.114	517	−41.3 ± 0.3
	MMT + $NiSO_4$ + $NiCl_2$ + H_3BO_3	1.20 ± 0.01	51.8	>7000	−13.5 ± 0.7
5	MMT	0.85 ± 0.01	0.50	527	−41.4 ± 0.5
	MMT + $NiSO_4$ + $NiCl_2$ + H_3BO_3	2.77 ± 0.05	50.2	>7000	−18.3 ± 0.6
10	MMT	1.03 ± 0.01	1.48	674	−41.4 ± 0.9
	MMT + $NiSO_4$ + $NiCl_2$ + H_3BO_3	17.8 ± 0.8	50.0	>7000	−17.4 ± 0.6
30	MMT	1.16 ± 0.01	2.59	1835	−41.9 ± 0.8
	MMT + $NiSO_4$ + $NiCl_2$ + H_3BO_3	1299 ± 12	46.2	>7000	−9.5 ± 0.7
50	MMT	18.4 ± 0.1	5.59	4079	−26.3 ± 1.4
	MMT + $NiSO_4$ + $NiCl_2$ + H_3BO_3	>3000	43.5	>7000	−1.9 ± 0.7

5.2.3.2 Vickers Microhardness Measurement

The hardness value of a metal-composite coating is influenced by two essential factors, the microstructure of the metal matrix and the amount of the clay into the metal matrix. The microstructure of the metal matrix is defined by the electrodeposition process, the interaction between nucleation and crystal growth which are affected by the bath composition, pH, current density and type of current [43].

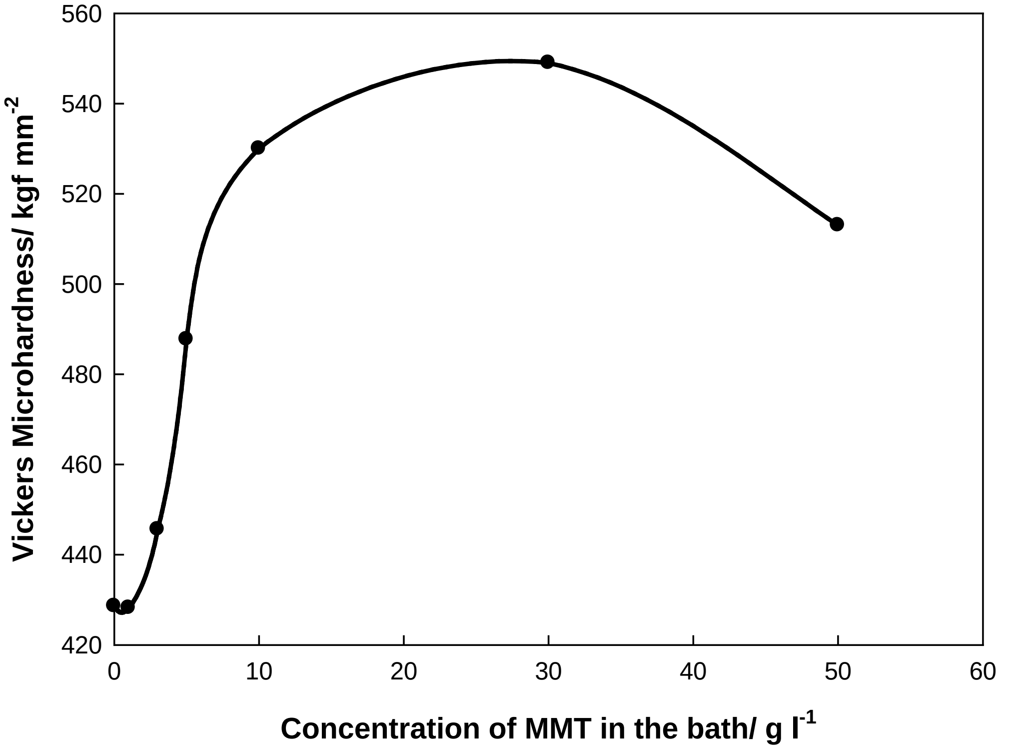

Figure 5.8: Effect of MMT concentration in the plating bath on Vickers microhardness of Ni-MMT composite coating.

Figure 5.8 shows the influence of MMT concentration in the plating bath on the microhardness of the composite coating. An increase in the microhardness value of Ni-MMT composite coatings was observed with increase in the MMT concentration in the plating bath reaching a maximum at 30 g/L. This confirms that the incorporation of MMT particles leads to an increase in the composite microhardness when compared to pure Ni. The increased hardness of Ni-MMT can be attributed to grain refining [30, 44] which is related to the nucleation of small grains on the surface of the incorporated particles, resulting in structural refinement. The presence of smaller grains impedes dislocation motion resulting in an increase in the microhardness [45].

5.2.3.3 Crystalline Orientation

Figure 5.9 shows the XRD patterns of pure Ni and Ni–MMT composite coatings. The XRD diagrams of pure Ni and Ni–MMT composites showed a higher (200) reflection for the coatings compared to the random powder pattern for synthetic nickel (PDF #004-0850). These results show that the crystalline growth is in the [100] direction giving a preferred orientation for the coatings. Incorporation of MMT particles into the Ni matrix leads to decreasing of the [100] texture as compared to pure Ni coating (see Table 5.8). This decrease was accompanied by reinforcement of [211] crystalline orientation (indicated by relative increasing of (311) and (111) intensities) [46]. The value of RTC(111) changed from 8.1% in pure Ni to 31.1% in Ni–MMT whereas, RTC(200) changed from 81.3% in pure Ni to 42.0% in the composite (Figure 5.10), this observation confirms that embedding of MMT particles into the Ni matrix modifies the [100] texture to a mixed orientation of Ni crystallites through [100] and [211] axes.

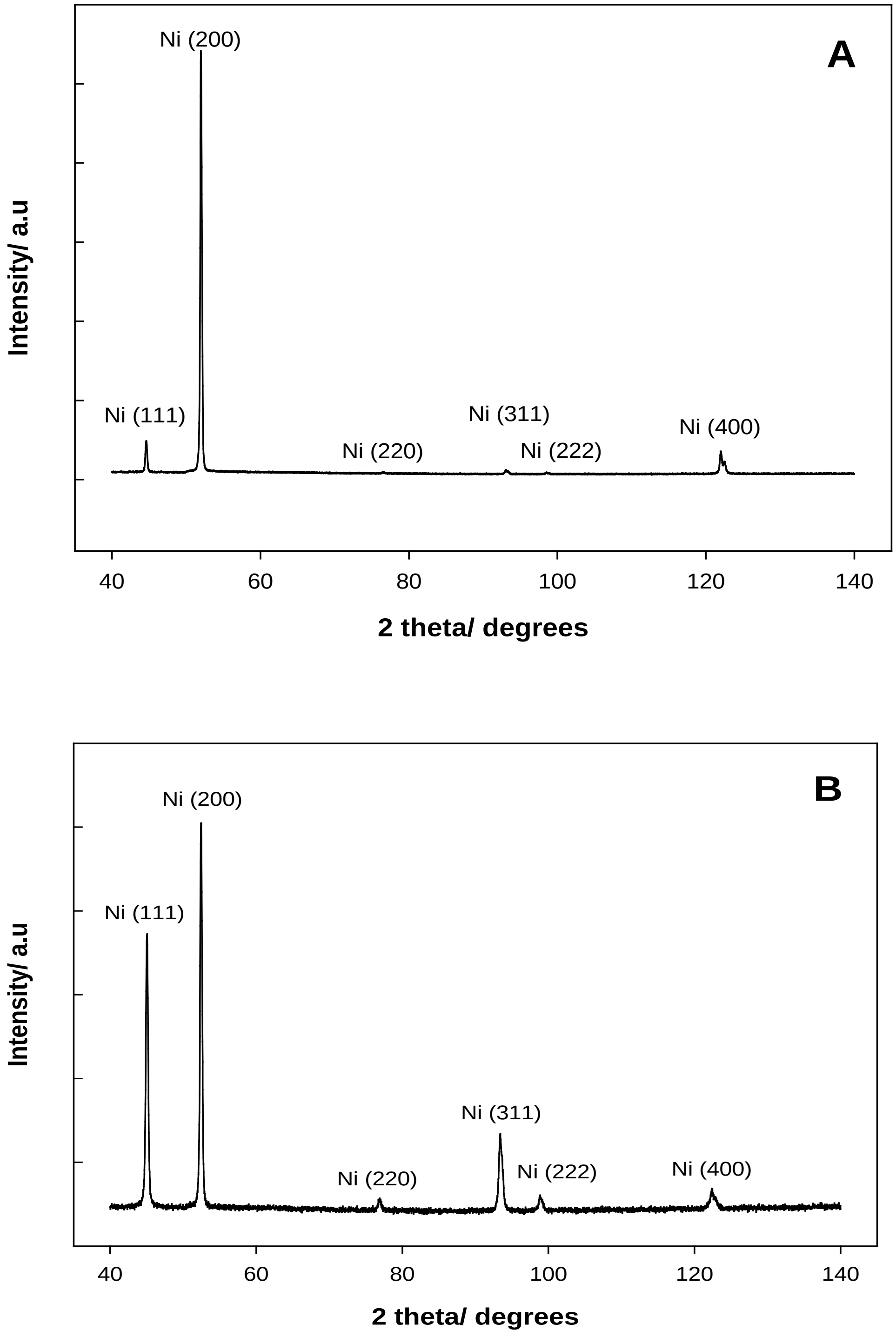

Figure 5.9: XRD patterns of (A) pure Ni and (B) Ni-MMT composite coatings prepared at the same pulse current conditions.

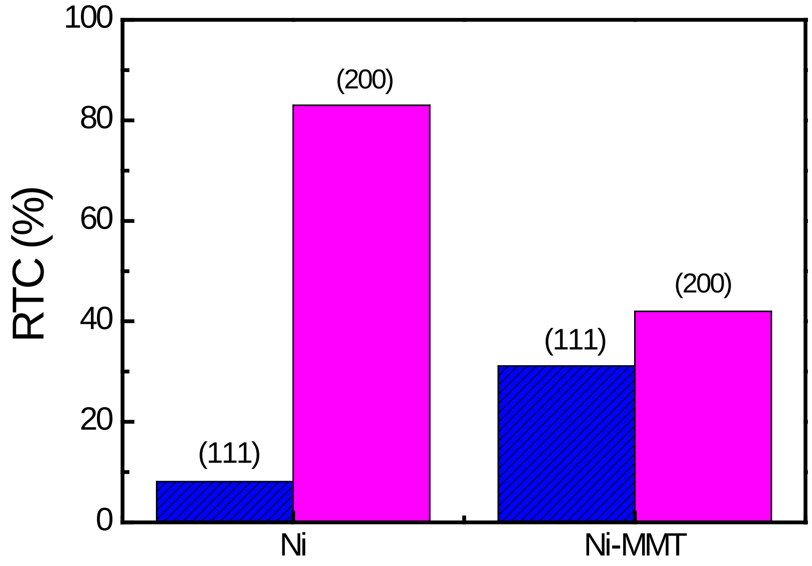

Figure 5.10: Quality of (111) and (200) orientations for pure Ni and Ni-MMT composite coatings.

Table 5.8: XRD reflections for Ni and Ni-MMT composite coatings.

(hkl)	**Ni**		**Ni-MMT**	
	d (Å)	**$[I/I_0]_{hkl}$**	**d (Å)**	**$[I/I_0]_{hkl}$**
111	2.0291	10	2.0111	74
200	1.7571	100	1.7428	100
220	1.2430	2	1.2387	12
311	1.0605	3	1.0579	26
222	1.0156	2	1.0134	12
400	0.8805	7	0.8791	14

5.2.3.4 Corrosion Behavior of Ni and Ni-MMT Composite Coatings

5.2.3.4.1 Potentiodynamic Polarization Measurements

Figure 5.11 illustrates the potentiodynamic polarization curves of pure Ni and Ni-MMT composite coatings in simulated sea water. The calculated corrosion parameters are summarized in table 5.9. The obtained data indicates the improvement of the corrosion resistance of Ni-MMT composites as compared to pure Ni. The corrosion potential of Ni-MMT (-318 mV vs SCE) is more cathodic compared to that of pure Ni (-283 mV) (Table 5.9). The corrosion current density, i_{corr} of Ni (4.27 µA cm^{-2}) is significantly reduced to 1.46 µA cm^{-2} for Ni-MMT which affirms the fact that the incorporation of MMT particles into the Ni matrix improves its corrosion resistance.

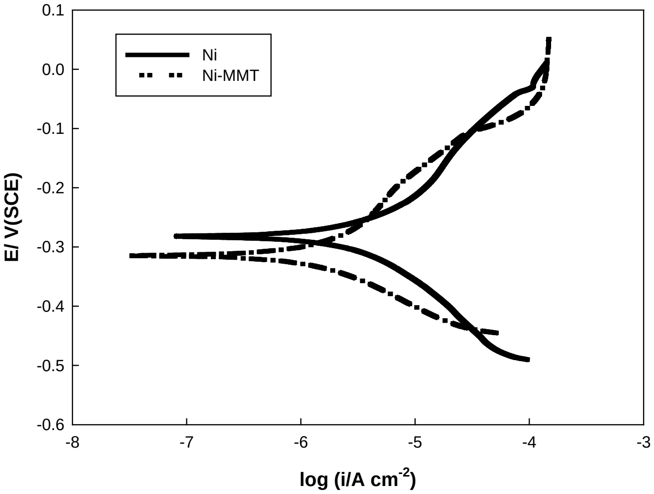

Figure 5.11: Tafel polarization curves of Ni and Ni-MMT composite coatings after 24h immersion in simulated seawater.

Table 5.9: The corrosion parameters of Ni and Ni-MMT composite coatings after 24h immersion in simulated seawater.

	E_{Corr} (mV)	**I_{Corr} (µA cm^{-2})**	**β_a (V decade^{-1})**	**β_c (V decade^{-1})**
Ni	-283	4.27	0.235	0.217
Ni-MMT	-316	1.46	0.197	0.119

The improvement in the corrosion resistance due to embedding of MMT particles into Ni can be attributed to the following reasons [47-49]: (1) MMT particles act as inert physical barriers that impede initiation and propagating of defect corrosion, (2) the dispersion of MMT particles into the Ni matrix forms micro corrosion cells that facilitate anodic polarization inhibiting localized corrosion and (3) corrosion must proceed via a circuitous path due to grain refinement caused by insertion of MMT particles i.e. the length of the bath is longer in Ni-MMT composite due to smaller crystallite size [49].

5.2.3.4.2 EIS Measurements

Figure 5.12a represents Bode impedance plots of pure Ni and Ni-MMT composite coatings in simulated sea water. The impedance data display two time constants.

Nyquist plots of Ni and Ni-MMT are represented in figure 5.12b. The diameter of the semicircle has higher value in case of Ni-MMT when compared to that of pure Ni which confirms higher resistance for the passive barrier film of Ni-MMT coatings.

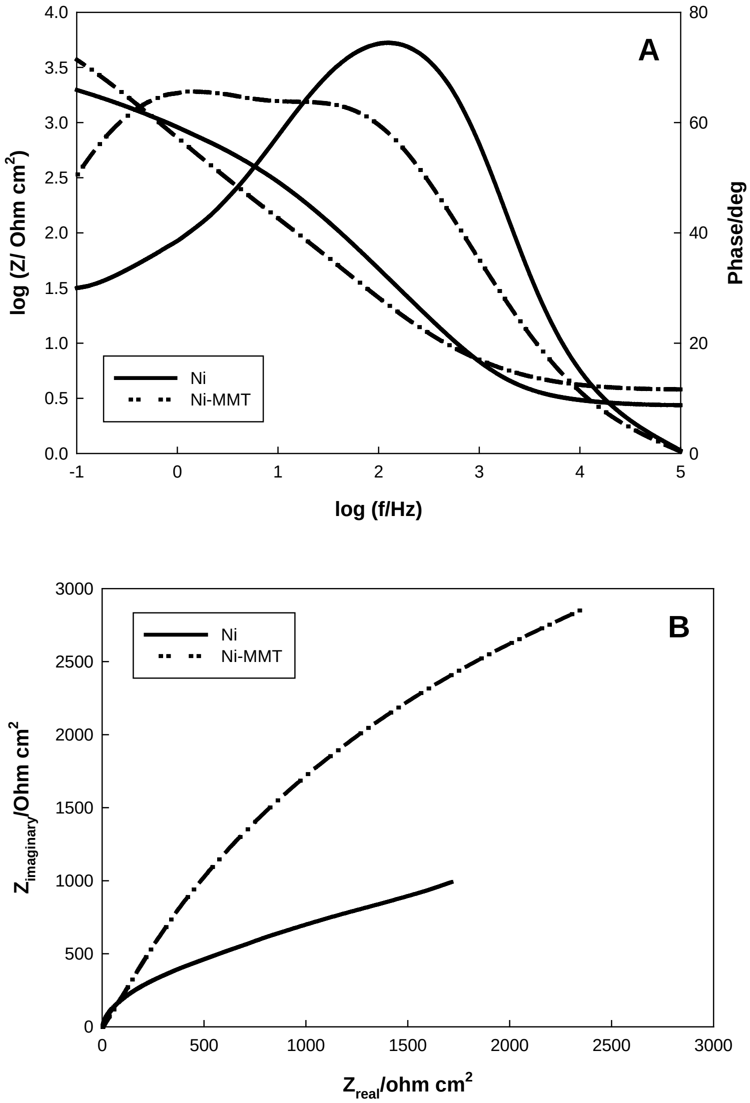

Figure 5.12: Impedance plots of pure Ni and Ni-MMT composite coatings after 24h immersion in simulated seawater expressed as: (A) Bode plots and (B) Nyquist plots.

The experimental impedance data was fitted to theoretical data according to different models and the best fitting was the equivalent circuit model shown in figure 5.13. Fitting procedures showed good agreement between theoretical and experimental data when a frequency dependent constant phase element (Q) was used instead of pure capacitor. The equivalent circuit model used to fit the obtained impedance data consists of two circuits in series R_1Q_1 and R_2Q_2 with the solution resistance, R_s. R_1 and Q_1 represent the resistance and capacitance of the outer barrier layer, respectively, whereas R_2 and Q_2 represent the resistance and capacitance of the inner barrier layer, respectively [51]. For this model the capacitance of the film is given as:

$$C^{-1} = Q_1^{-1} + Q_2^{-1} \qquad \text{Eq. (4.1)}$$

This model has several structures; one of them is the Voight model where its impedance value is expressed as [52]:

$$Z(\omega) = R_s + \frac{R_1}{1+R_1Q_1(j\omega)^{\alpha_1}} + \frac{R_2}{+R_2Q_2(j\omega)^{\alpha_2}} \qquad \text{Eq. (4.2)}$$

The equivalent circuit parameters are presented in table 5.10. These parameters show that the total resistance value (R_1+R_2) is greater for the Ni-MMT composite coating than of pure Ni which indicates improved corrosion resistance of Ni-MMT and confirmed the results obtained from polarization measurements.

Table 5.10: The equivalent circuit parameters of Ni and Ni-MMT composite coatings after 24h immersion in simulated seawater.

	R_s (Ω cm^2)	R_1 (kΩ cm^2)	Q_1 (Ω^{-1} s$^{\alpha}$ cm^{-2})	α_1	R_2 (kΩ cm^2)	Q_2 (Ω^{-1} s$^{\alpha}$ cm^{-2})	α_2
Ni	3.920	3.29	314.7	0.81	0.716	61.8	0.91
Ni-MMT	5.33	0.218	1091	0.64	12.55	226	0.83

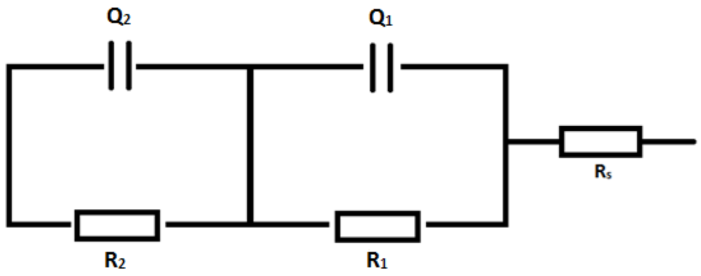

Figure 5.13: Equivalent circuit model representing electrode/electrolyte interface.

5.2.3.5 Surface Morphology and Topography

Figure 5.14 shows the surface morphology of pure Ni compared to Ni-MMT composite coatings. It can be observed that embedding MMT particles in Ni resulted in production of smaller crystallite sizes than those obtained for pure Ni (prepared under the same conditions).

The 3D surface morphology changes in the Ni and Ni-MMT samples were obtained by AFM at scan rate 1.00 Hz and scan size of 1.00 µm, as shown in figure 5.15. The surface roughness of samples was expressed by an average deviation parameter (Ra). The Ra value represents the average height of irregularities in the direction perpendicular to the sample surface. The surface of the Ni samples was a relatively smooth, which was confirmed by the relatively low Ra value, only 5.7 nm (Figure 5.15A). On the other hand, modification of Ni by MMT led to the significant increase of the surface roughness, when the Ra value increased to 21.0 nm (Figure 5.15B). This fact was probably caused by a very rough surface structure of pure MMT.

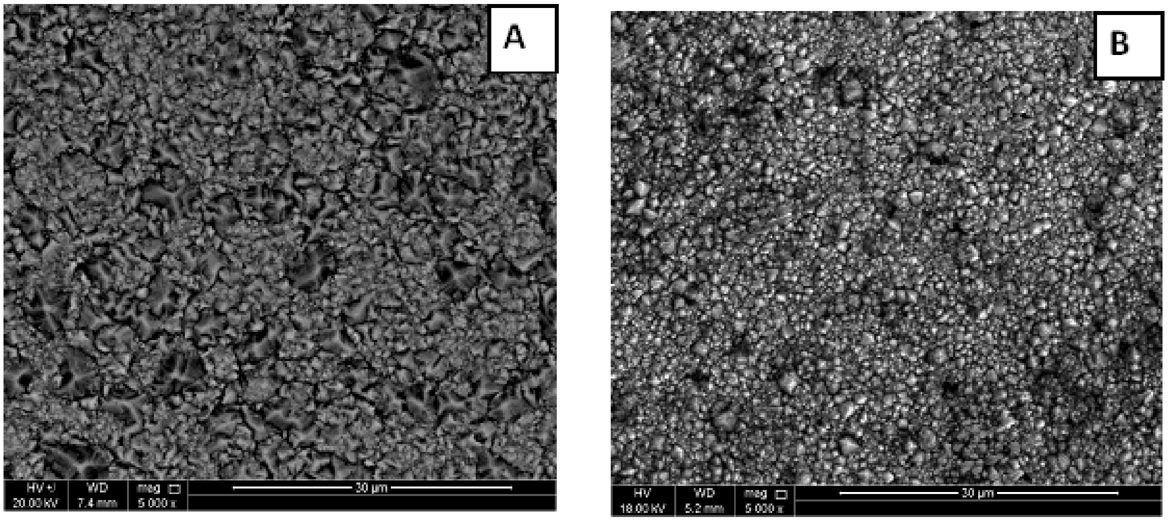

Figure 5.14: SEM micrographs of: (A) pure Ni and (B) Ni-MMT composite coatings prepared at the same pulse current conditions.

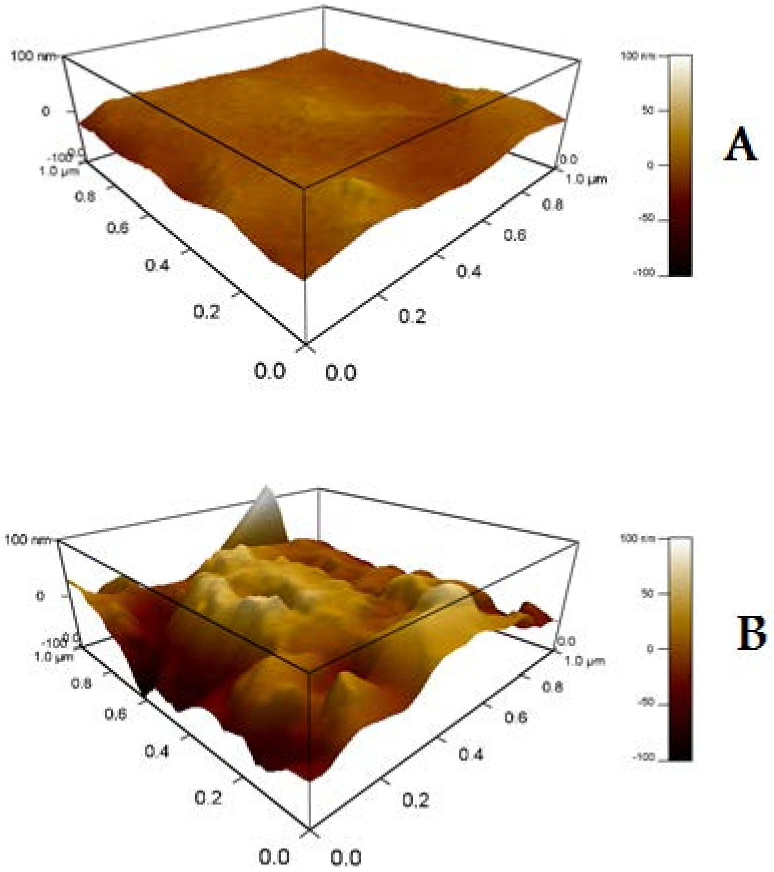

Figure 5.15: AFM micrographs of: (A) pure Ni and (B) Ni-MMT composite coatings prepared at the same pulse current conditions.

5.2.4 Conclusions

1. The amount of incorporated MMT into the Ni matrix increases with increasing concentration in the plating bath up to a maximum of 30 g/l.

2. Vickers microhardness of Ni–MMT composite coating increases with increasing the amount of MMT embedded into the film.

3. Incorporation of MMT into Ni modifies [100] texture to a mixed orientation through [100] and [211].

4. The corrosion resistance of Ni–MMT composite coating is higher than pure Ni as revealed from polarization and impedance measurements.

5. The crystalline size of Ni in the composite is smaller than pure Ni and Ni–MMT film shows higher surface roughness than pure Ni film.

6. Ni–MMT film of low silicate content showed smaller friction coefficient than pure Ni but films of high percentage of MMT showed higher friction coefficient.

5.3 Improved Mechanical and Corrosion Properties of Nickel Composite Coatings by Incorporation of Layered Silicates in Basic Solution (pH 9.5)

5.3.1 Introduction

Nickel and nickel alloys with dull or matte finishes from Watt’s bath are electrodeposited to improve corrosion and wear resistance [52]. The operating parameters, such as pH, temperature, chloride content, and current density influence the properties of the coatings [52]. Although Watts baths are operated in acidic solution pH (0.5-5.9), it was suggested that hardness, tensile strength, and internal stress of nickel film increased when depositing above pH 5 [52]. Additionally, nickel alloys particularly NiMo and NiW are mostly operated in alkaline solutions at pH ranging from 7 to 10 whereas in acidic baths is not attractive due to a low molybdenum or tungsten content codeposited in the nickel alloys [53-62]. It is consequently of interest to electrodeposit nickel/layered silicate in alkaline solution to increase more possibility to improve the corporation of layered silicate into the film to enhance its mechanical strength and corrosion resistance. Additionally, the electrodeposition of nickel/layered silicate film is supposed to pave a way to improve the Ni/Mo/layered silicate deposition which mostly electrodeposited from alkaline citrate bath.

In this work, nickel-layered silicate nanocomposite films were electrochemically deposited using pulsed potentiostatic conditions from an alkaline plating bath containing exfoliated clay nanoparticles. Alkaline electrodeposition gives a more uniform deposit for some nickel alloys, which results in better corrosion protection of the underlying metal [8]. Scanning electron microscopy (SEM) was used to determine the morphology of the electrodeposited films. X-ray diffraction (XRD) was used to confirm the crystal structure of the films. The corrosion resistance and hardness of the nanocomposite films were compared with that of the pure nickel deposits using Tafel polarization, immersion tests, electrochemical impedance spectroscopy and nanoindentation.

5.3.2 Experimental

5.3.2.1 Materials

All of the solutions were prepared from analytical-grade chemicals dissolved in deionized water. Nickel and nickel-layered silicate films were electrodeposited from a citrate bath at ambient temperature. The plating bath contained 0.1 M $NiSO_4 \cdot 6H_2O$, (Alfa Aesar) and 0.1 M $Na_3C_6H_5O_7 \cdot 2H_2O$ (Fisher Scientific Company) adjusted to pH 9 with 1 M ammonium hydroxide. Montmorillonite concentrations ranging from 0.05 to 5.0% were vigorously stirred for 24 hours by a mechanical stirrer to exfoliate the clay into the individual clay platelets (~1 nm thick) prior to introduction into the plating solution. The layered silicate solution was used as the makeup solution instead of deionized water for the plating bath. The working electrode was polished mechanically with 600, 800, and 1000 grit silicon carbide paper, then with 3 and 1 μm diamond solution on felt cloth. After the electrode was polished to a mirror-like finish, it was sonicated in deionized water for 10 minutes. The electrochemical cell was comprised of three electrodes; stainless steel (working electrode), chromel wire (counter electrode), and saturated calomel (reference electrode).

5.3.3 Results and Discussion

Montmorillonite (MMT) is a layered-silicate clay which has the formula $(Na, Ca)(Al_{1.66}Mg_{0.33})_3(Si_4O_{10})_3(OH)_6 \cdot n(H_2O)$ [64]. MMT needs to be exfoliated in aqueous solution to obtain the individual layered silicate platelets which also increases its total interfacial area in solution. The exfoliated platelets have an approximate thickness of 1 nm and effective diameter of 2000 nm. The length-to-thickness ratio of the exfoliated silicates when introduced into matrices (such as polymers) has shown enhanced mechanical properties of the resulting composite [65]. Montmorillonite is not electroactive and thus has no redox couple for electrodeposition. When introduced in solution, the clay swells and shears apart. With increasing concentration, a gel like state is obtained called the “house of cards”. Addition of MMT results in a new partially exfoliated structure (with platelet stacking corresponding to 2-5 individual plates). In electrolytes, up to ~4% of exfoliated MMT can be suspended in the aqueous solution. Once the negatively charged layered silicate is introduced into the plating solution, the platelets are countered with positive nickel ions. These platelets are believed to electrostatically adsorb onto the substrate during deposition. They may reorient on the film surface to give the most stable arrangement. The planar shape of MMT can produce a tight contact with the oppositely-charged surface, and its adsorption is influenced strongly by the shape of particle surface [63]. The nickel ion is eventually reduced to nickel metal, electrodepositing onto the substrate.

The optimum clay concentration was chosen based on the kinematic viscosity of the plating solutions. As seen in Figure 1a, MMT solutions exhibited linearity at low concentration ranges (0-0.5%) in the solution. The kinematic viscosity values for the concentrations of 0.01 to 0.05% MMT was ~ 1.008 to 1.057 mm^2/s or cSt at 19.5^{o}C, which is similar to that of water (0.996 mm^2/s or cSt at 19.5^{o}C). For these dilute concentrations, the charged MMT are solvated by water which has a higher ionic strength, resulting in a stabilized aqueous suspension. However, the MMT plates are non-spherical, thus the rotary Brownian motion may lead to a non-Newtonian effect even in dilute solutions. At higher concentrations of the MMT (above 1% MMT), the viscosity deviates from linearity as illustrated in figure 5.16a.

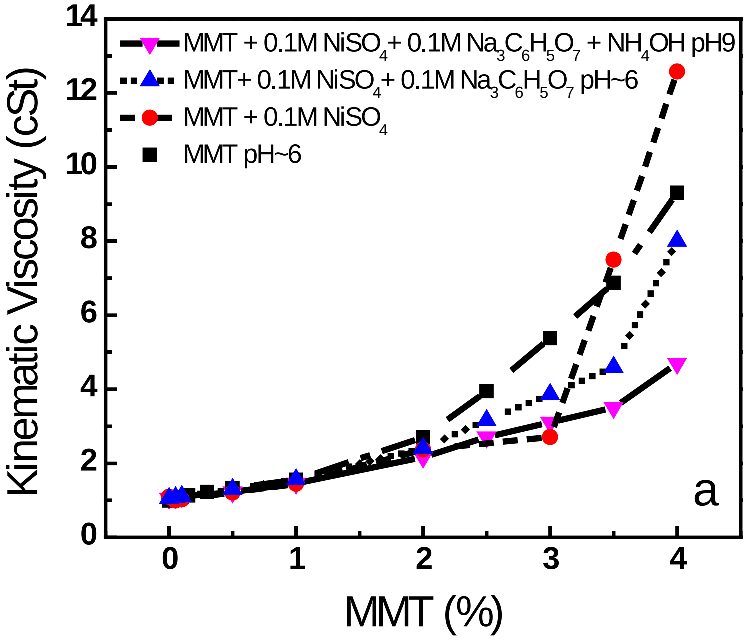

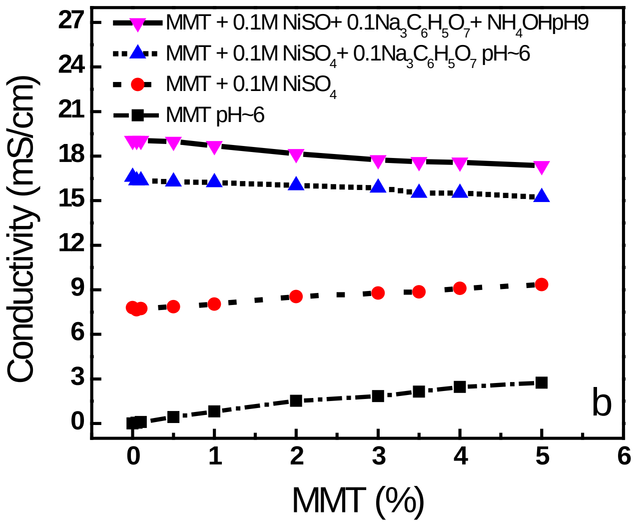

Figure 5.16: The influence of plating components on kinematic viscosity (a) and conductivity (b) of various MMT suspensions.

The higher MMT concentration does not simply change the magnitude of kinematic viscosity, but because of its platelet shape and charge results in a deviation of Newtonian behavior [66]. The viscosity of the nickel-clay has the same trend as that of the clay solution until the concentration reaches ~ 2% MMT. When the exfoliated MMT is added to a solution of nickel ions, the viscosity steeply increases for concentrations of MMT greater than 3%, resulting in thickening of the fluid or semi-gelation. This agglomeration at higher concentrations of MMT in the nickel sulfate solution is also evident by the much larger particle size (>7000 nm) measured by light scattering (Table 5.11) compared to MMT alone (452-781 nm). Once citrate ions are introduced into the nickel-clay solution, the viscosity decreases for MMT concentrations above 3%, since the nickel ions which previously adsorbed onto the clay surface are now bound by the citrate ligand. With increasing pH, citrate in alkaline solution is fully dissociated to form a tridentate ligand containing carboxylates which strongly bind to nickel ions resulting in an effective stabilization of nickel. Therefore, when the solution is adjusted to pH 9, the nickel is bound strongly to the citrate ligand resulting in even less free nickel to neutralize the clay platelets [67]. The Ni-citrate complex formed at pH 9 is $[Ni(C_6H_4O_7)]^{2-}$. In this solution, the viscosity stays low even for increasing concentrations of MMT (Figure 5.16a). The clay platelets and nickel complex repel each other in solution resulting in a stable MMT suspension. The measured conductivity (Figure 5.16b) for the solutions follows the viscosity results. MMT only solutions have lower conductivity since the Na^+ and negative charged platelets give an essentially neutral solution. However, the conductivity increases with the addition of nickel-citrate and is even higher for the solution at pH 9 where the complex has an overall -2 charge. The size of the particles in the various solutions is shown in table 5.11. The size increases with increasing concentration of MMT for the solutions. The stability of MMT-Ni-Cit-pH 9 decreases corresponding to the decreased zeta potential values (-41.2, -36.7, and -32.8 mV) with increasing concentration of MMT (0.05, 0.5, and 2 %, respectively). Exfoliation methods for the clay also affect the size of the MMT platelets. For a 0.5% MMT solution prepared by stirring for 24 hours, the particle size is ~591 nm. However, if that solution is treated for an additional hour of ultrasonication or heating, the particle size decreases to 231 nm (Table 5.11). Tuning of the charges and surface forces between the clay platelets and the electrode surface are critical for the incorporation of particles into a metal matrix during electrodeposition [22]. Further studies are needed to elucidate the complete mechanism for these nanocomposite films.

Table 5.11: Particle sizes of MMT in various solutions measured by particle size analyzer.

%MMT	Zeta potential (mV)	Diameter (nm)				
	MMT-Ni-Cit-pH9	MMT-Ni-Cit-pH9	MMT-Cit-pH9	MMT-Ni-pH9	MMT-pH6	MMT-pH6 (sonicated)
0.05	-41.2 ± 0.4	986	781	>7000	452	210
0.50	-36.7 ± 0.3	1358	1544	>7000	591	231
2.00	-32.8 ± 0.5	1504	3326	>7000	781	303

Cyclic voltammograms (CV) for nickel and nickel-layer silicate nanocomposite baths are shown in figure 5.17. Each CV shows that the nickel reduction potential for both the Ni-citrate bath and Ni-MMT-citrate bath are the same at -0.76 V. This indicates that the layered silicate does not affect the reduction potential of Ni (II) ion. However, one advantage of the addition of MMT to the plating solution is it helps increase the electrochemical working range by pushing hydrogen evolution slightly more cathodic. Thus, the deposition behavior is not expected to be adversely affected by the addition of the non-electrolytic layered silicates. The trisodium citrate used as the complexing ligand for the Ni effectively stabilized the nickel (II) ions in the plating solution without precipitating out $Ni(OH)_2$. The citrate in the Ni bath functions as a brightening and leveling agent [24, 67] without the need to add other plating additives.

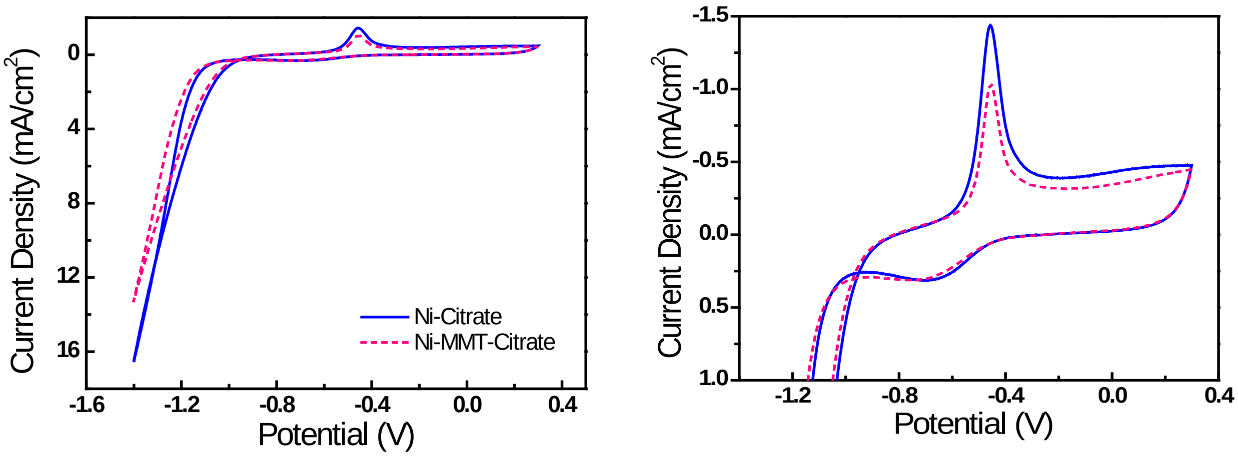

Figure 5.17: Cyclic voltammograms of nickel and nickel-layered silicate (0.5% MMT) plating solutions at pH 9.

The surface morphologies of electrodeposited nickel-layered silicates had fine grains and smooth surfaces as shown by SEM in figure 5.18. The composite film is compact and uniform like the nickel film, so the MMT does not disrupt the morphology. EDX of the nanocomposite films show the presence of Mg, Al, and Si as well as Ni (Table 5.12). As expected there is an increase in concentration of Mg, Al, and Si with increasing concentrations of MMT in the plating solution (Table 5.12).

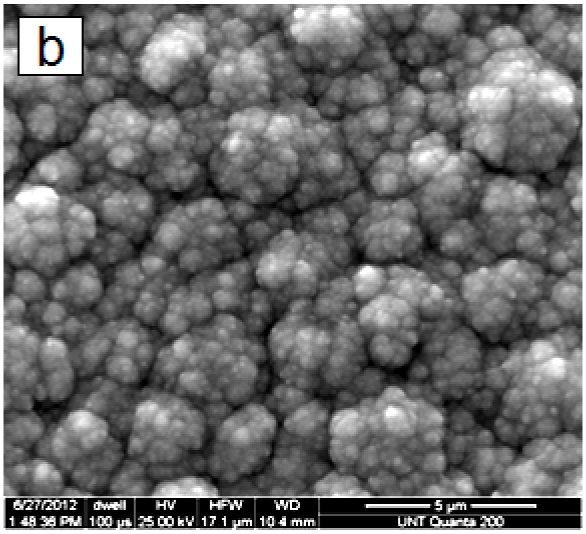

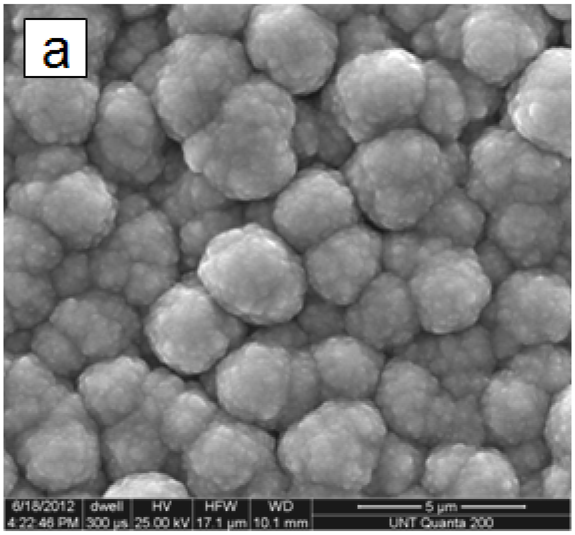

Figure 5.18: SEM images of (a) Ni deposit and (b) Ni-MMT (0.5%) nanocomposite.

Table 5.12: Elemental composition determined from EDX results of nickel-layer silicate coating surface at various MMT concentrations in the plating bath.

MMT (%) in bath	**Element composition (at %)**			
	Mg	**Al**	**Si**	**Ni**
0.05	0.70±0.27	0.95±0.15	0.87±0.20	94.85±0.68
0.50	0.85±0.40	1.44±0.43	2.43±0.84	91.71±0.90
2.00	1.46 ±0.64	2.11±0.26	3.96±0.71	87.67±2.14

The incorporation of the clay platelets into the Ni matrix does not affect the nickel crystal structure as confirmed with XRD (Figure 5.19). The nickel (Figure 5.19a) and nickel-layered silicate (Figure 5.19b) films are both crystalline with a slight preferred (111) orientation. Also, the exfoliation of the MMT platelets is indicated by the absence of x-ray reflections at lower 2θ values (2-30°) in figure 5.19b.

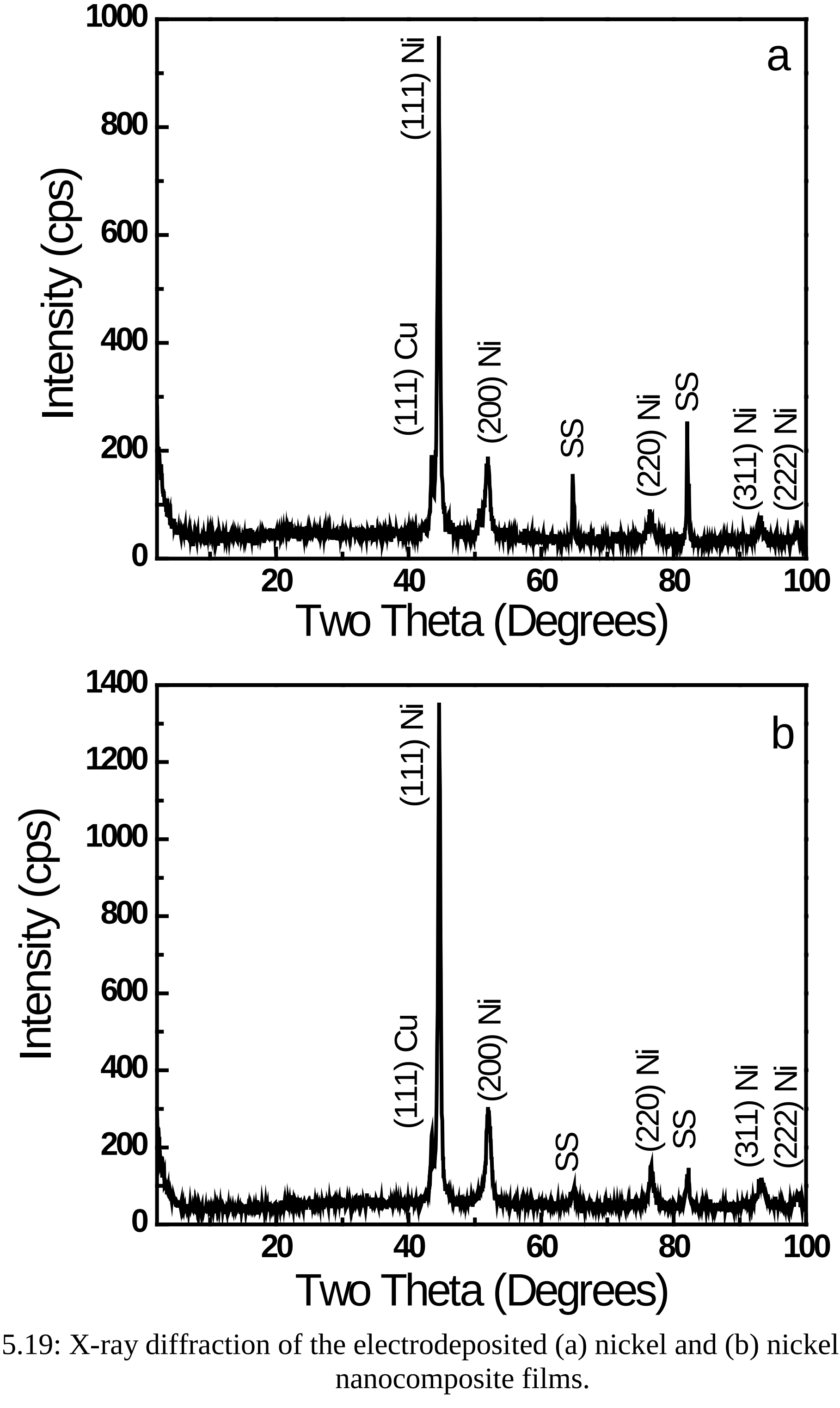

Figure 5.19: X-ray diffraction of the electrodeposited (a) nickel and (b) nickel-MMT (0.5%) nanocomposite films.

Tafel polarizationwas run in a 3.5% NaCl solution for pure nickel and nanocomposite films to investigate the effect of the clay platelets on the corrosion behavior of the films, as shown in figure 5.20. It can be seen that, the addition of the layered silicate platelets into the nickel film increased the corrosion resistance of the films. The corrosion currents and potentials are listed in able 4.13. Over time, the nickel-layered silicate film begins to self-passivate. When the Ni films are newly deposited (0 h), the Ecorr is around -0.59 V and slowly increases to -0.32 V after 30 h. The i_{corr} values for Ni-MMT (5.75 x 10^{-7} A/cm^2) are lower than for Ni (1.87 x 10^{-6} A/cm^2) indicating an improved corrosion rate.

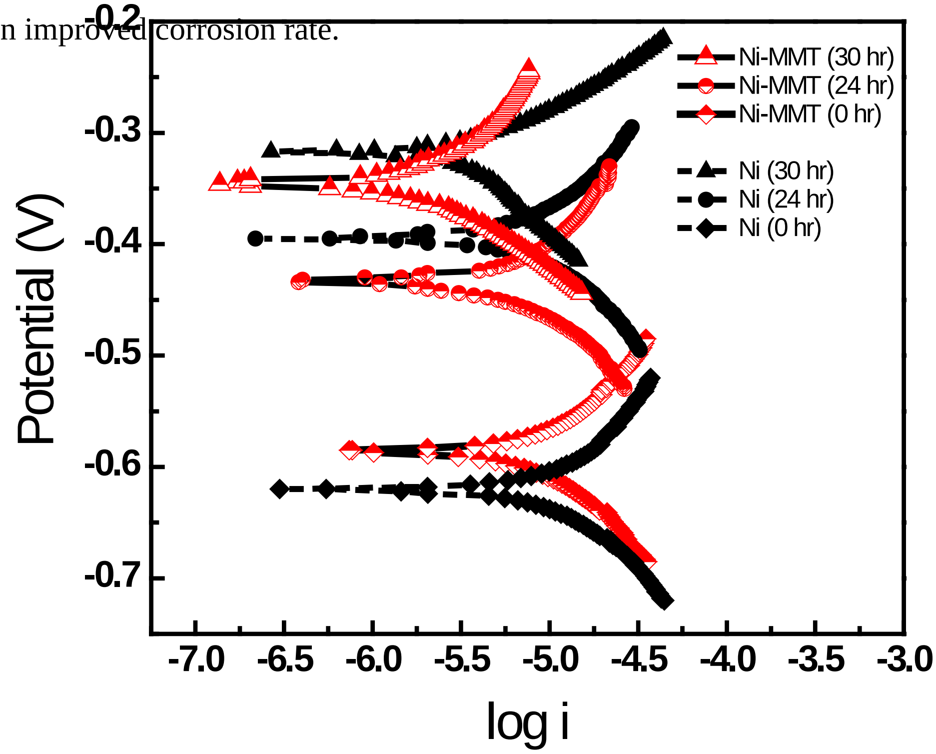

Figure 5.20: Tafel plots for Ni and Ni-MMT (0.5%) nanocomposite coatings measured by immersion in 3.5% NaCl solution at ambient temperature for various time of 0, 24, and 30 hours.

Table 5.13: Corrosion potentials and current for pure nickel and Ni-MMT films at 0, 24, and 30 hours from Tafel's extrapolation and calculated polarization resistance.

Immersion time (hr) for Ni and Ni-MMT coating	**E_{corr} (V)**	**I_{corr} (A/cm^2)**	**R_p (kΩ cm^2)**
0 (Ni-MMT)	-0.45	3.31×10^{-6}	39.2
24 (Ni-MMT)	-0.29	1.23×10^{-6}	210
30 (Ni-MMT)	-0.26	5.75×10^{-7}	237
0 (Ni)	-0.59	3.51×10^{-6}	52.7
24 (Ni)	-0.37	3.24×10^{-6}	131
30 (Ni)	-0.32	1.87×10^{-6}	86.9

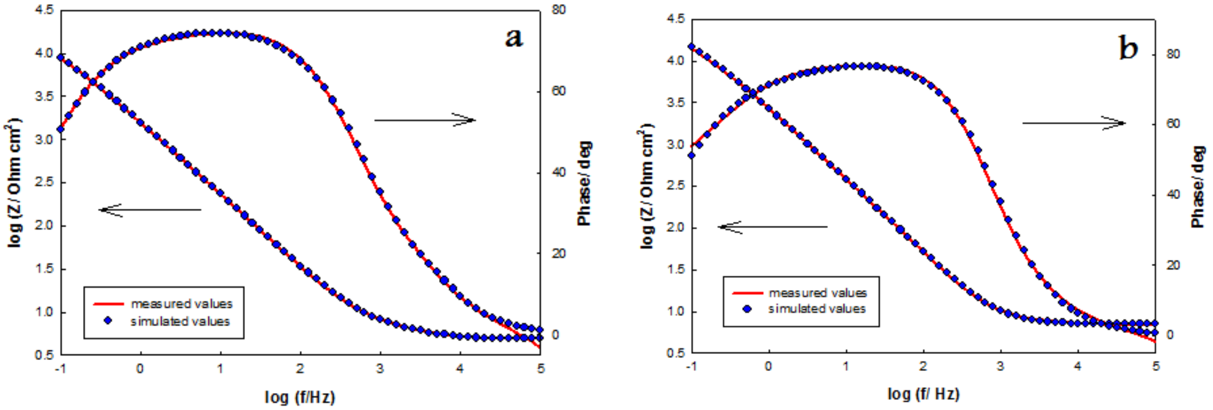

Figure 5.21: Bode impedance plots of (a) Ni and (b) Ni-MMT coatings after 24h immersion in 3.5% NaCl solution.

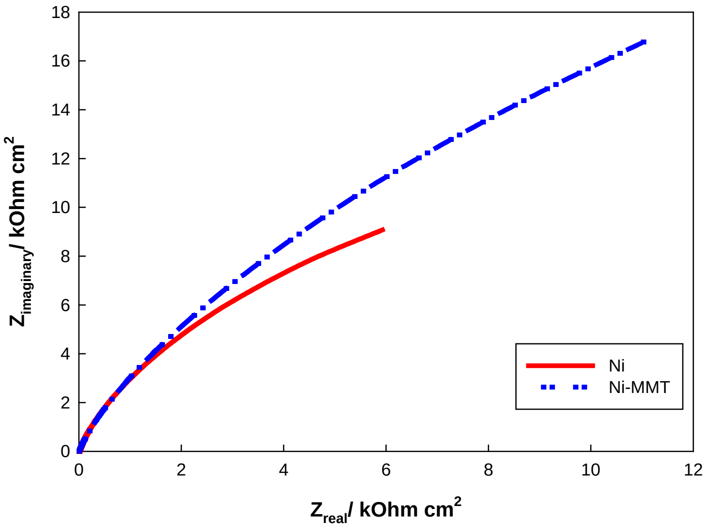

Figure 5.22: Nyquist impedance plots of Ni and Ni-MMT coatings after 24h immersion in 3.5% NaCl solution.

Figures 4.21 and 4.22 represent Bode and Nyquist impedance plots of Ni and Ni-MMT after immersion in 3.5% NaCl solution for 24 h, respectively. It can be observed that, the |Z| values for the Ni-MMT composites are higher compared to the values of pure Ni at all frequencies which confirms the enhancement in corrosion resistance of Ni-MMT over Ni coatings.

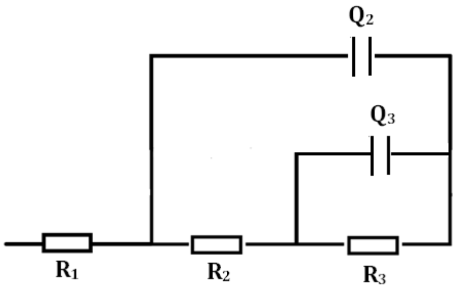

Figure 5.23: The equivalent circuit model used to fit the experimental impedance data of Ni and Ni-MMT coatings in 3.5% NaCl solution.

The impedance data was analyzed using software (Model Editor Version 6.03) provided with the electrochemical workstation and fitted to the equivalent circuit model, as shown in Figure 5.23. The appropriate equivalent model includes a solution resistance (R_1), R_2Q_2 couple which represents the resistance and capacitance of the outer layer, and R_3Q_3 which refers to the resistance and capacitance of the inner layer of the passive film. Fitting procedures have shown that good agreement between the theoretical and experimental data is obtained if a frequency-dependent constant phase element (Q) is introduced in the equivalent circuit model instead of a pure capacitor. The impedance associated with the capacitance of the constant phase element is a combination of properties related to both the surface and the electroactive species and is described by the following expression:

$$Z_{CPE} = Y_0^{-1}(j\omega)^{-\alpha} \qquad \text{Eq. (4.3)}$$

where Y_0 is the frequency independent real constant of the constant phase element which is identical to the idealized capacitance at $\omega=1$, ω being the angular frequency ($\omega=2\pi f$), $j=\sqrt{-1}$, and α is an adjustable empirical exponent which varies between 1.0 for a purely capacitive behavior associated with a perfectly smooth surface and 0.5 for a porous electrode.

It can be seen from the results in table 5.14 that the resistance of the inner and outer layer for the Ni-MMT composite is higher than the corresponding values for pure Ni which indicates improvement of the corrosion resistance of the protective coatings as a result of incorporation of MMT into the Ni films. Also, the capacitance of the inner and outer passive film is lower for Ni-MMT than pure Ni due to a decrease in the local dielectric constant.

Table 5.14: Equivalent circuit parameters of Ni and Ni-MMT coatings after 24 hours immersion in 3.5 % NaCl solution.

Coating type	R_1 (Ω cm^2)	R_2 (Ω cm^2)	Q_2 (μF cm^{-2})	α_2	R_3 (kΩ cm^2)	Q_3 (μF cm^{-2})	α_3
Ni	4.93	3.80	17.17	0.99	20.7	118	0.80
Ni-MMT	7.3	8.41	16.0	0.98	61.92	45.5	0.75

Immersion tests at ambient temperature in 3.5% NaCl solution were run to measure the corrosion resistance and stability of the deposits. Open circuit potential (OCP) versus time (hours) is shown in figure 5.24. The pure nickel film began cracking after one day and within 5 days started to peel from the substrate when immersed in the 3.5% salt solution, which indicates brittleness. The nanocomposite films however exhibit self-passivation over time as the OCP value increased to ~ -0.15 V after 50 hours. After 15 days, the OCP value remained stable and the film was smooth in appearance. Photos showing the appearance of the immersed films with time are shown in figure 5.25.

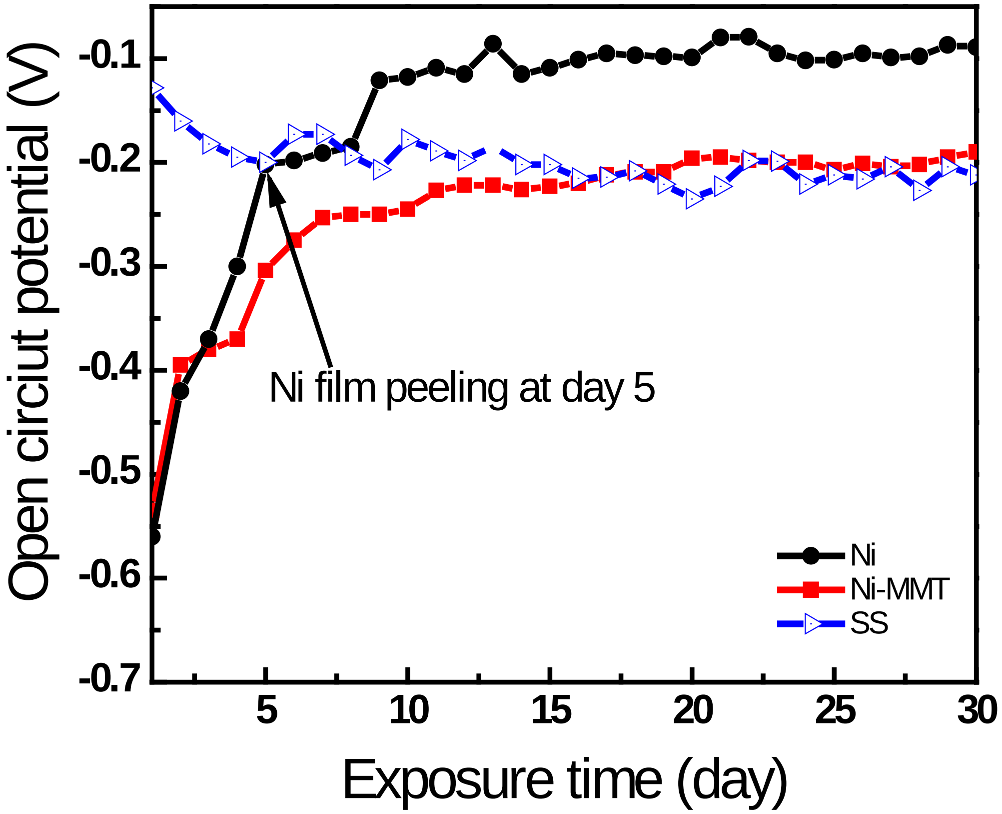

Figure 5.24: OCP versus immersion time for stainless steel, pure nickel and nickel-layered silicate films in 3.5% NaCl.

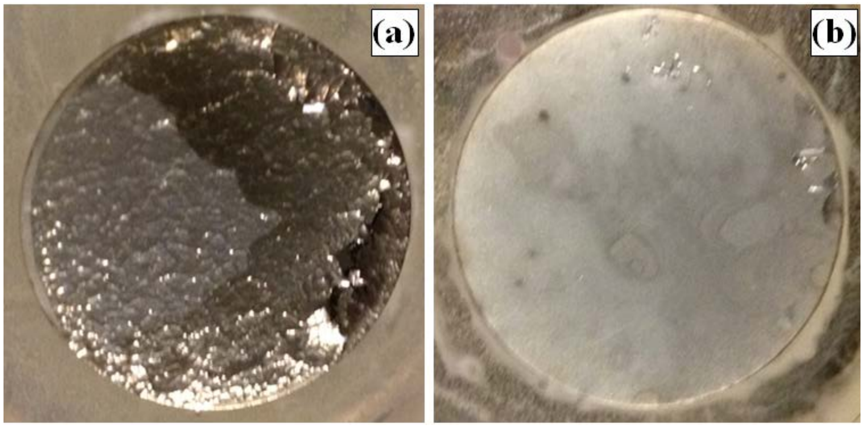

Figure 5.25: Appearance of the immersed films of (a) Ni and (b) Ni-MMT in 3.5% NaCl for 30 days.

Table 5.15: Nanoindentation hardness and young modulus at various displacement depths (nm) of the Ni-MMT nanocomposite film compared with the nickel film.

Displacement Depth (nm)	**Young Modulus (GPa ± SD, n)**		**Nanoindentation hardness (GPa ± SD, n)**	
	Ni	**Ni-MMT**	**Ni**	**Ni-MMT**
200	151.22±9.16 (5)	180.91±22.15 (4)	4.06±0.24 (5)	3.09±0.96 (4)
300	163.07±53.57 (20)	224.26±21.65 (21)	3.80±1.65 (20)	5.89±0.78 (20)
400	173.88±44.77 (4)	217.05±24.09 (4)	3.92±1.49 (4)	4.96±0.89 (4)
1200	169.19±46.58 (17)	201.0 ±19.08 (23)	3.70±1.74 (17)	4.74±0.75 (17)

The hardness of the deposits was measured using a nanoindentation tester with a load of 100 g applied for 20 s. The average hardness values for each deposit are listed in Table 5.15. Young's modulus and hardness values increased for the coatings with the addition of the layered silicates into the nickel film showing improved mechanical properties. Young's modulus improved from 164 for Ni to 206 GPa for Ni-MMT (25% increase), while hardness increased from 3.87 for the nickel films to 4.67 GPa for the nanocomposite Ni-MMT films (20% increase).

5.3.4 Conclusions

The dispersion of layered silicates into nickel plating solutions was studied at various concentrations of MMT. An MMT concentration of 0.5% was optimal, since the viscosity was low at this concentration and the platelets dispersed well in the electrolyte solution. Adhesion of the films was better at 0.5% MMT than at 2% MMT. The incorporated layered silicates showed eventual passivation of the coating leading to better stability and adhesion of the film on the stainless steel substrates. SEM images showed the nanocomposite films were smooth and uniform. The crystal structure of the nickel films was not disrupted and remained fcc with the addition of the clay platelets. Incorporation of exfoliated montmorillonite as a layered silicate into nickel films by electrodeposition, enhanced both corrosion resistance and hardness.

5.4 Chapter References

[1] Friend, W. Z., *Corrosion of Nickel and Nickel-Base Alloys*. Willey-Interscience: New York, 1980.

[2] Chang, Y.-Y.; Wang, D.-Y., *Surface and Coatings Technology*. **2005**, *200* (7), 2187-2191.

[3] Wang, A. Q.; D'Souza, N.; Golden, T. D., *Journal of Materials Chemistry*. **2006**, *16* (5), 481-488.

[4] Xuetao, Y.; Yu, W.; Dongbai, S.; Hongying, Y., *Surface and Coatings Technology*. **2008**, *202* (9), 1895-1903.

[5] Brondel, D., Edwards, R., Hayman, A., Hill, D., Mehta, S., Semerad, T., *Oilfield Review*. **1994**, *6* (2), 4-18.

[6] Richardson, M. C.; Kim, J.; Ho, D.; Snyder, C. R.; D’Souza, N. A.; Holmes, G. A., *Polymer Composites*. **2011**, 32(1), 67–78.

[7] Horch, R. A., Golden, D. T., D’Souza A. N., Riester, L., *Chemistry of Materials*. **2002**, *14* (2), 3531-3538.

[8] Conrad, A. H., Corbett, R. J., Golden, D. T., *Journal of the Electrochemical Society* **2012**, *159* (1), 29-32.

[9] DeLeon, V., Golden, D. T., *ECS Transitions*. **2011**, *33* (21), 43-50.

[10] Camargo, H. C. P., Satyanarayana G. K., Wypych, F., *Materials Research*. **2009**, *12* (1), 1-39.

[11] Chen, W., He, Y., Gao, W., *Journal of the Electrochemical Society*. **2010**, *157* (8), 122-128.

[12] Benea, L., *J Appl Electrochem*. **2009**, *39* (10), 1671-1681.

[13] Corni, I.; Chater, R.; Boccaccini, A.; Ryan, M., *J Mater Sci. 2012*, *47* (14), 5361-5373.

[14] Ben Temam, H.; Zeroual, L.; Chala, A.; Rahmane, S.; Nouveau, C., *Plasma Processes and Polymers*. **2007**, *4* (S1), S618-S621.

[15] Sen, R.; Das, S.; Das, K., *Materials Research Bulletin*. **2012**, *47* (2), 478-485.

[16] Sahu, L., D’Souza, A. D., *The Open Macromolecules Journal*. **2012**, *6*, 28-32.

[17] Ogunsona, E., Ogbomo, S., Nar, M., D'Souza, N.A., *Cellular polymers*. **2011**, *3* (2), 79-93.

[18] Wang, A. Q.; D'Souza, N.; Golden, T. D., *Applied Clay Science*. **2008**, *42* (1–2), 310-317.

[19] Zaarei, D.; Sarabi, A.; Sharif, F.; Kassiriha, S., *J Coat Technol Res*. **2008**, *5* (2), 241-249.

[20] Olad, A.; Amini, M.; Rashidzadeh, A., *Fibers Polym.* **2012**, *13* (4), 475-480.

[21] Macosko, C. W., *Rheology: Principles, measurements and applications*. John Wiley & Sons: New York, 1993.

[22] Dedeloudis, C., ransaer, J., Celis, J-P., *Journal of Physical Chemistry.* **2000**, *104* (9), 2060-2066.

[23] Kraepiel, A. M. L.; Keller, K.; Morel, F. M. M., *Journal of Colloid and Interface Science.* **1999**, *210* (1), 43-54.

[24] Green, T. A., Russell, A. E., Roy, S., *Journal of the Electrochemical Society* . **1998**, *145* (3), 875-881.

[25] Li, C.-q.; Li, X.-h.; Wang, Z.-x.; Guo, H.-j., *Transactions of Nonferrous Metals Society of China.* **2007,** *17* (6), 1300-1306.

[26] Zelenin, O. Y., *Russ J Coord Chem.* **2007**, *33* (5), 346-350.

[27] Rode, S., Henninot, C., Matlosz, M., *Journal of the Electrochemical Society.* **2005**, *152*(4), 248-254.

[28] Surender, M.; Basu, B.; Balasubramaniam, R., *Tribology international.* **2004**, *37* (9), 743-749.

[29] Szczygieł, B.; Kołodziej, M., *Electrochimica Acta.* **2005**, *50* (20), 4188-4195.

[30] Lampke, T.; Wielage, B.; Dietrich, D.; Leopold, A., *Applied Surface Science.* **2006**, *253* (5), 2399-2408.

[31] Ger, M.-D., *Materials Chemistry and Physics.* **2004**, *87* (1), 67-74.

[32] Hu, F.; Chan, K. C., *Materials Chemistry and Physics.* **2006**, *99* (2–3), 424-430.

[33] Aal, A. A.; Zaki, Z. I.; Hamid, Z. A., *Materials Science and Engineering: A* 2007, *447* (1-2), 87-94.

[34] Low, C. T. J.; Wills, R. G. A.; Walsh, F. C., *Surface and Coatings Technology.* **2006**, *201*(1-2), 371-383.

[35] Stojak, L. J., Fransaer, J., Talbot, B. J., in: R.C. Alkire, D.M. Kolb *Advances in Electrochemical Science and Engineering*. Wiley-VCH Verlag: Weinheim, 2002.

[36] Ciubotariu, A. C.; Benea, L.; Lakatos–Varsanyi, M.; Dragan, V., *Electrochimica Acta.* **2008**, *53*(13), 4557-4563.

[37] Staia, M.; Conzono, A.; Cruz, M.; Roman, A.; Lesage, J.; Chicot, D.; Mesmacque, G., *Surface engineering.* **2002**, *18* (4), 265-269.

[38] Singh, V. B.; Pandey, P., *Surface and Coatings Technology*. **2006**, *200* (14–15), 4511-4514.

[39] Danowska, M.; Piszczyk, L.; Strankowski, M.; Gazda, M.; Haponiuk, J., *Journal of Applied Polymer Science*. **2013**, *130* (4), 2272-2281.

[40] Peng, S.; Fan, X.; Zhang, J.; Wang, F., *Applied Catalysis B: Environmental*. **2013**, *140-141*, 115-124.

[41] Praus, P.; Turicová, M.; Karlíková, M.; Kvítek, L.; Dvorský, R., *Materials Chemistry and Physics*. **2013**, *140* (2-3), 493-498.

[42] Bodman, S. D.; McWhinnie, W. R.; Begon, V.; Millan, M.; Suelves, I.; Lazaro, M. J.; Herod, A. A.; Kandiyoti, R., *Fuel*. **2003**, *82*(18), 2309-2321.

[43] Budevski, B. E., taikov, E. F., Lorenz G. T., J. W., *Electrochemical Phase Formation and Growth. An Introduction to the Initial Stages of Metal Deposition*. 2nd Ed., Wiley-VCH: Weinheim, 1996.

[44] Feng, Q.; Li, T.; Yue, H.; Qi, K.; Bai, F.; Jin, J., *Applied Surface Science*. **2008**, *254* (8), 2262-2268.

[45] Gül, H.; Kılıç, F.; Aslan, S.; Alp, A.; Akbulut, H., *Wear*. **2009**, *267* (5–8), 976-990.

[46] Gomes, A., Pereira, I.,Fernandez, B., Pereiro, R., *Electrodeposition of metal matrix nanocomposites: improvement of the chemical characterization techniques*. InTech: 2011.

[47] Feng, Q.; Li, T.; Teng, H.; Zhang, X.; Zhang, Y.; Liu, C.; Jin, J., *Surface and Coatings Technology*. **2008**, *202* (17), 4137-4144.

[48] Chen, X. H.; Chen, C. S.; Xiao, H. N.; Cheng, F. Q.; Zhang, G.; Yi, G. J., *Surface and Coatings Technology*. **2005**, *191* (2-3), 351-356.

[49] Xue, Y.-J., Shen, C., Li, J.-S., Li, H., Si, D.-H., *Advanced Materials Research*. **2010**, *97*, 1235-1238.

[50] Ameer, M. A.; Fekry, A. M., *Progress in Organic Coatings*. **2011**, *71* (4), 343-349.

[51] Patrito, E. M.; Macagno, V. A., *Journal of Electroanalytical Chemistry*. **1994**, *375* (1–2), 203-211.

[52] Bari, G.A.D., *Chapter 3: Electrodeposition of Nickel, Modern Electroplating*, Ed., John Wiley and Sons, Inc.: New York, 2010.

[53] Abner Brenner, *Electrodeposition of Alloys: Principles and Practice*, Ed., Academic Press, 1963.

[54] E.J. Podhala and D. Landolt, *J. Electrochem. Soc.* **1997**, 144, 1672-1680.

[55] T. Ohgai, R. Washio, Y. Tanaka, *Journal of Electrochemical Socciety*. **2012**, 159(10), H800-H804.

[56] E.J. Podhala and D. Landolt, *J. Electrochem. Soc.* **1996**, 143, 885-892.

[57] S. Sun, E. J. Podlaha, *Journal of Electrochemical Society*. **2012**, 159(2), D97-D102.

[58] E. J. Podlaha, D Landolt, *J. Electrochem. Soc*. **1996**, 143(3), 893-899.

[59] M. Donten, H. Cesiulis, Z. Stojek, *Electrochimica Acta*. **2005**, 50, 1405–1412.

[60] E. Chassaing, M. P. Roumegas, M. F. Trichet, *Journal of Applied Electrochemistry*, **1995**, 25(7), 667-670.

[61] D. Landolt, A. Marlot, *Surface and Coatings Technology*. **2003**, 169-170, 8–13.

[62] A Marlot, P Kern, D Landolt, *Electrochimica Acta*. **2002**, 48(1), 29–36.

[63] K. Ariga, Y. I. LvovIchinose, T. Kunitake, *Applied Clay Science* **1999**, *15*(1–2), 137-152.

[64] D. M. Moore, R. C. Reynolds, *X-ray diffraction and the identification and analysis of clay minerals*. 2nd Ed.; Oxford: New York, 1997.

[65] O.Y. Golubeva, V.V. Gusarov*Glass Phys Chem.* **2007**, *33* (3), 237-241.

[66] W.C. Macosko, *Principles, Measurements and Applications*. John Wiley & Sons: New York, 1993.

[67] E. Beltowska-Lehman,; P. Indyka, *Thin Solid Films.* **2012**, *520* (6), 2046-2051.

CHAPTER 6

ELECTRODEPOSITION OF NICKEL-MOLYBDENUM ALLOYS

6.1 Nickel-Molybdenum Alloys

Stainless steels are corrosion resistant in a wide range of environments due to formation of a passivating film on their surfaces. Despite passivity, extensive localized corrosion commonly occurs on stainless steels when exposed to harsh environments containing chloride ions, such as seawater. Chloride ions dislocate the passivating species at various sites within the passive film resulting in the initiation of pitting nuclei. Once the passivity has been destroyed, the reactions inside the growing pits propagate through an anodic process leading to a loss of strength in the overall structure [1-5]. Molybdenum, having been used as one of the fundamental metals incorporated in stainless steels, is of interest to alloy with nickel to enhance the repassivation behavior and deactivate pit growth in aggressive chloride media [6-10]. Additionally, the presence of molybdenum improves mechanical properties of the alloys [11]. Electrodeposition techniques have been used to synthesize several surface engineering materials including metals, ceramics, polymers, or composite coatings [12]. The coatings fabricated by electrodeposition techniques provide a superior nanocrystalline structure improving corrosion protection and hardness properties of the materials [13-20]. Due to the coating stability, nickel is commonly used to alloy with other metals to protect substrate materials under severe operating conditions such as corrosive environments, high temperatures and high stresses. Pure nickel offers high ductile ability and toughness to hold its face-centered cubic structure until its melting point (1455^{o}C), therefore, nickel provides an important base for developing specialized alloys. Nickel can form intermetallic phases with some metals commonly used in nickel alloys leading to high strength for both low and high-temperature services [20, 22]. Molybdenum, in the same group as chromium and tungsten, has a melting point of 2620 ^{o}C. Molybdenum offers similar heat stability as tungsten but is less expensive therefore is used to alloy with nickel leading to improved corrosion resistance, mechanical properties and heat stability. The nanocrystalline thin films of nickel-molybdenum alloys, having been developed through electrochemical deposition processes, have been used for various applications including catalysts for the hydro processing of aromatic oils and hydrogenation of benzene in the gas phase [19]. Nickel- based alloys containing 9-16 weight percent molybdenum offer high corrosion resistance against chloride attack [22, 23]. In addition, molybdenum is another alternative component to alloy with nickel to replace toxic components such as chromium which have been previously used for improved mechanical properties of the nickel-based alloys.

In this research, nickel-molybdenum alloy is electrochemically deposited onto stainless steel to improve corrosion resistance and strength. Citrate and boric acid were utilized in the electrolyte to electrodeposit nickel-molybdenum alloys from molybdate (MoO_4^{2-}) and nickel (II) ions in an alkaline bath. Alkaline conditions were found optimal for deposition of molybdenum based on the Pourbaix diagram of molybdenum plating parameters.

6.2 Experimental

6.2.1 Materials

All of the solutions were prepared from analytical-grade chemicals dissolved in de-ionized water. Nickel-molybdenum films were electrodeposited from a citrate-borate bath at ambient temperature. Electroplating solutions were composed of nickel sulfate, $NiSO_4 \cdot 6H_2O$ (Alfa Aesar); sodium molybdate, $Na_2MoO_4 \cdot 2H_2O$ (Alfa Aesar); sodium citrate, $C_3H_4(OH)(COONa)_3 \cdot 2H_2O$ (Fisher Scientific Company); and boric acid, H_3BO_3 (Alfa Aesar). The solution pH was adjusted to 9.5 using ammonium hydroxide, NH_4OH (Fisher Scientific Company). The solutions were deaerated with nitrogen for 10 minutes before deposition. The nitrogen was slowly puffed through the solution to maintain $N_{2(g)}$ presence during the deposition. A stainless steel type 304 (1.8 cm^2) disc was used as working electrode and platinum mesh was used as counter electrode, while a saturated calomel electrode was used as the reference electrode. The stainless steel discs were polished mechanically with 600, 800, and 1000 grit silicon carbide paper, followed by 3 and 1 μm diamond solution on felt cloth. After the electrode was polished to a mirror-like finish, it was sonicated in deionized water for 10 minutes and degreased with ethyl alcohol then rinsed water. Before deposition the working electrode surface was activated by soaking in 1-5% HCl solution for 10 minutes followed by rinsing with DI water.

6.2.2 Electrodeposition Procedure

An EG&G PAR Potentiostat/Galvanostat Model 273A was used for all depositions, cyclic voltammetry, and corrosion studies. Cyclic voltammetry was used to investigate the electrodeposition potential of the nickel-molybdenum alloy from different molybdate [MoO_4^{2-}] to nickel [Ni^{2+}] molar ratios of 0.1, 1, and 5 compared to nickel plating solutions. The current densities were measured on the mirror-like polished stainless steel discs over the potential range from open circuit potential (OCP) to -1.6 V. Nickel-molybdenum alloy was prepared by an electrochemical deposition technique using pulsed potential modification. Nickel-molybdenum alloys are electrodeposited onto stainless steel with different accumulative charges, 20-100 Coulombs (C), to obtain an optimal thickness for characterization of the film. The cycle of the pulsed potential deposition was started with a cathodic potential at E1: -1.35 V and held for 10 seconds then pulsed to an anodic potential at E2: -0.7 V, held for 3 seconds then pulsed back to the initial potential at E1: -1.35 V.

6.3 Results and Discussion

6.3.1 Electrodeposition of Nickel-Molybdenum Alloys

According to Abner Brenner [25] and other previous works [26-41], molybdenum is not able to be electrodeposited alone in an aqueous electrolyte. Hence, nickel-molybdenum alloy was electrochemically deposited onto stainless steel substrates from alkaline ammonium-citrate-borate bath (pH 9.5). In the induced co-deposition of nickel-molybdenum, the behavior of each component and its mechanism is not immediately clear due to a complicated mechanism of the alloy formation. However, the mechanism of electrodeposition was postulated by a group of authors [26-31]. The induced co-deposition of molybdenum with nickel in citrate bath is believed to occur by a 2-step reduction of molybdenum via a species of $[NiCitMoO_2]_{ads}$ as shown in the reactions (ii and iii). Water molecules will be discharged simultaneously with molybdenum from the aqueous solutions. At alkaline pH, most of the citrate ligands are present as Cit^{3-} ions [33-36].

(i) $NiCit^- + 2e^- \rightarrow Ni(s) + Cit^{3-}$ Eq. (5.1)

(ii) $MoO_4^{2-} + NiCit^- + 2H_2O + 2e^- \rightarrow [NiCitMoO_2]^-_{ads} + 4OH^-$ Eq. (5.2)

(iii) $[NiCitMoO_2]^-_{ads} + 2H_2O + 4e^- \rightarrow Mo(s) + NiCit^- + 4OH^-$ Eq. (5.3)

(iv) $2H_2O + 2e^- \rightarrow H_2 + 2OH^-$ Eq. (5.4)

In this work, nickel-molybdenum is codeposited not only in citrate electrolyte but also introducing boric acid in to control pH resulting in improving adhesion of the deposits. The different concentration of molybdate ions are introduced into nickel plating solution to determine the influence of MoO_4^{2-} concentration on the induced co-depositing behavior of nickel-molybdenum alloys. The polarization curves of nickel-molybdenum electrodeposition were compared to the polarization curves of pure nickel deposition as shown in figure 6.1.

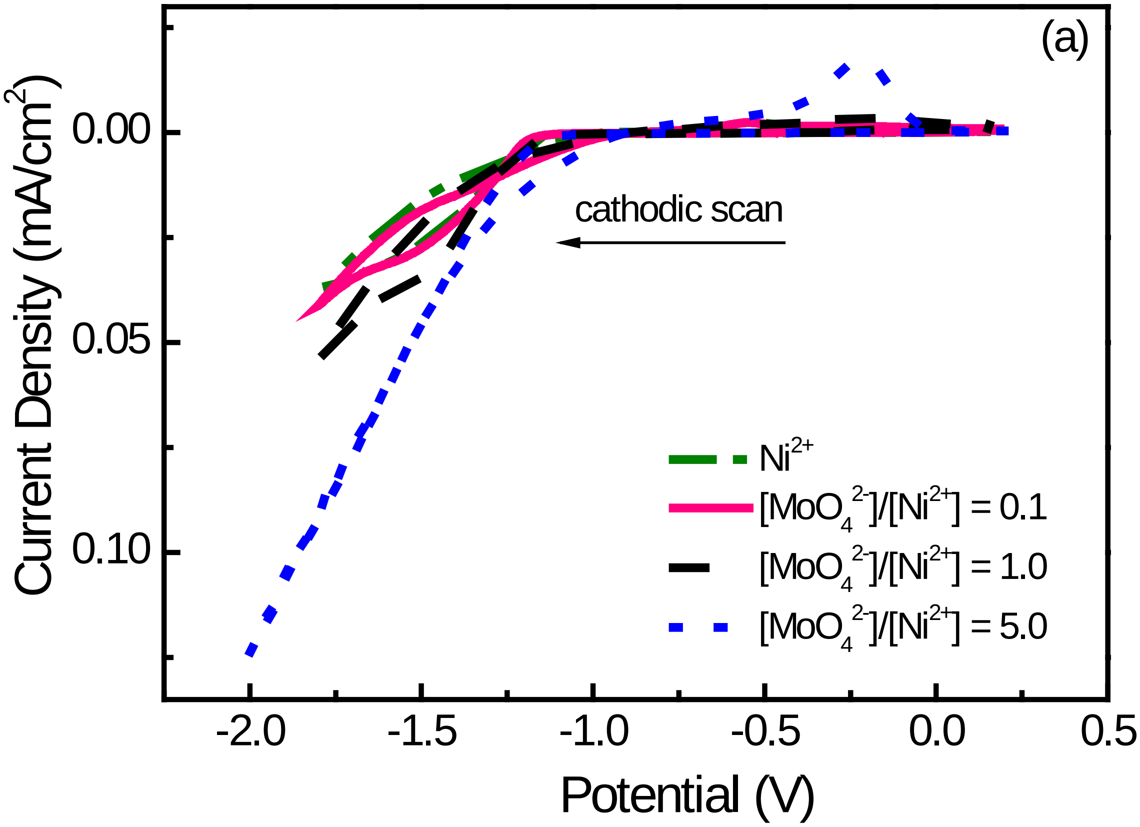

Figure 6.1: Cyclic voltammograms of different [MoO$_4^{2-}$]/[Ni^{2+}] molar ratio (0.1, 1.0, and 5.0) compared to Ni^{2+} from citrate-borate plating solutions at pH 9.5.

The cathodic scans of pure nickel and nickel with molybdate show the reduction peak between -0.7 to -0.9 V/SCE (Figure 6.2). The pure nickel film when deposited at the potential of -0.9 to -1.2 V/SCE gives a thick film, but at a low potential of -0.7 V/SCE no film is formed. Nickel-molybdenum can be deposited at the potential of -1.3 to -1.5 V/SCE where Ni^{2+}, MoO$_4^{2-}$ ions, and water are discharged at the same time gaining both nickel-molybdenum film and hydrogen evolution.

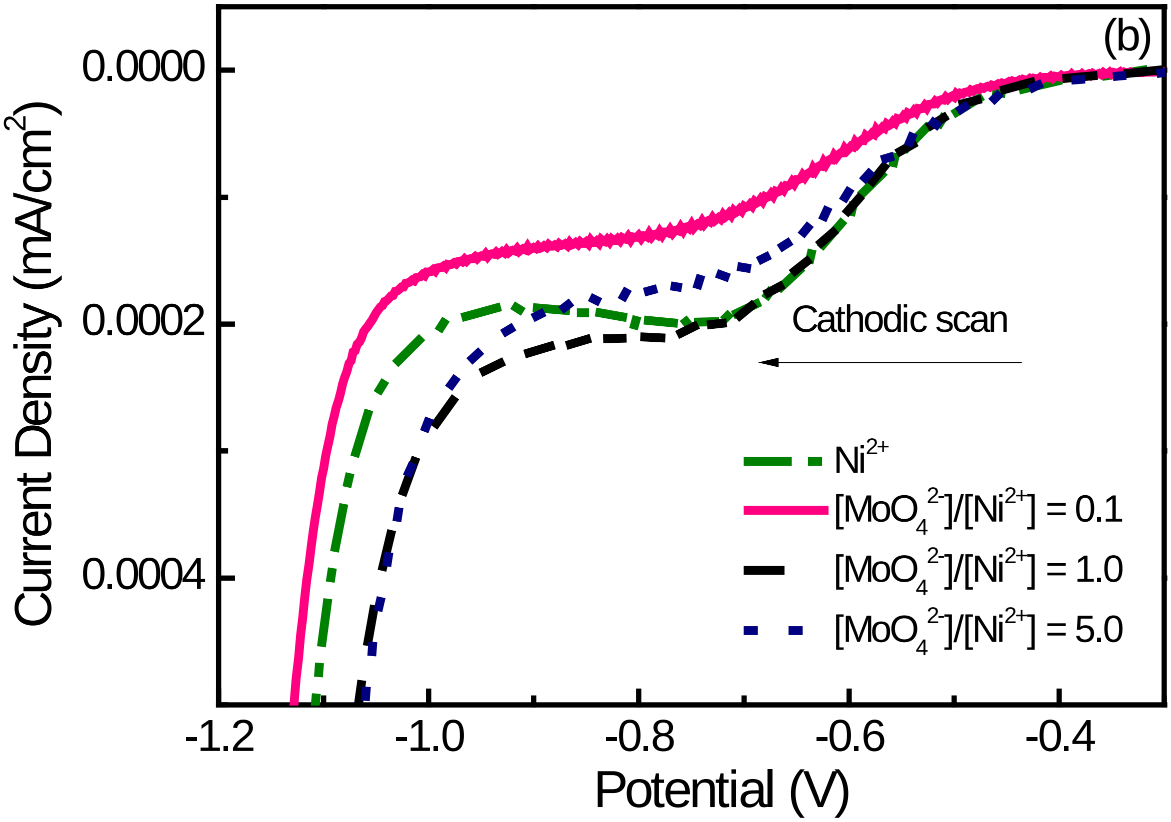

Figure 6.2: Cathodic scan of different [MoO$_4^{2-}$]/[Ni^{2+}] molar ratio (0.1, 1.0, and 5.0) compared to Ni^{2+} from citrate-borate plating solutions at pH 9.5.

The anodic polarization scan in figure 6.3 illustrates that nickel begins to oxidize around -0.7 to -0.5 V/SCE, explaining why it is not possible to deposit a nickel film at the potential of -0.7 V/SCE. A large anodic peak observed in the nickel-molybdate solution ([MoO$_4^{2-}$]/[Ni^{2+}]= 5) at -0.2 V/SCE, is due to the oxidation of molybdenum.

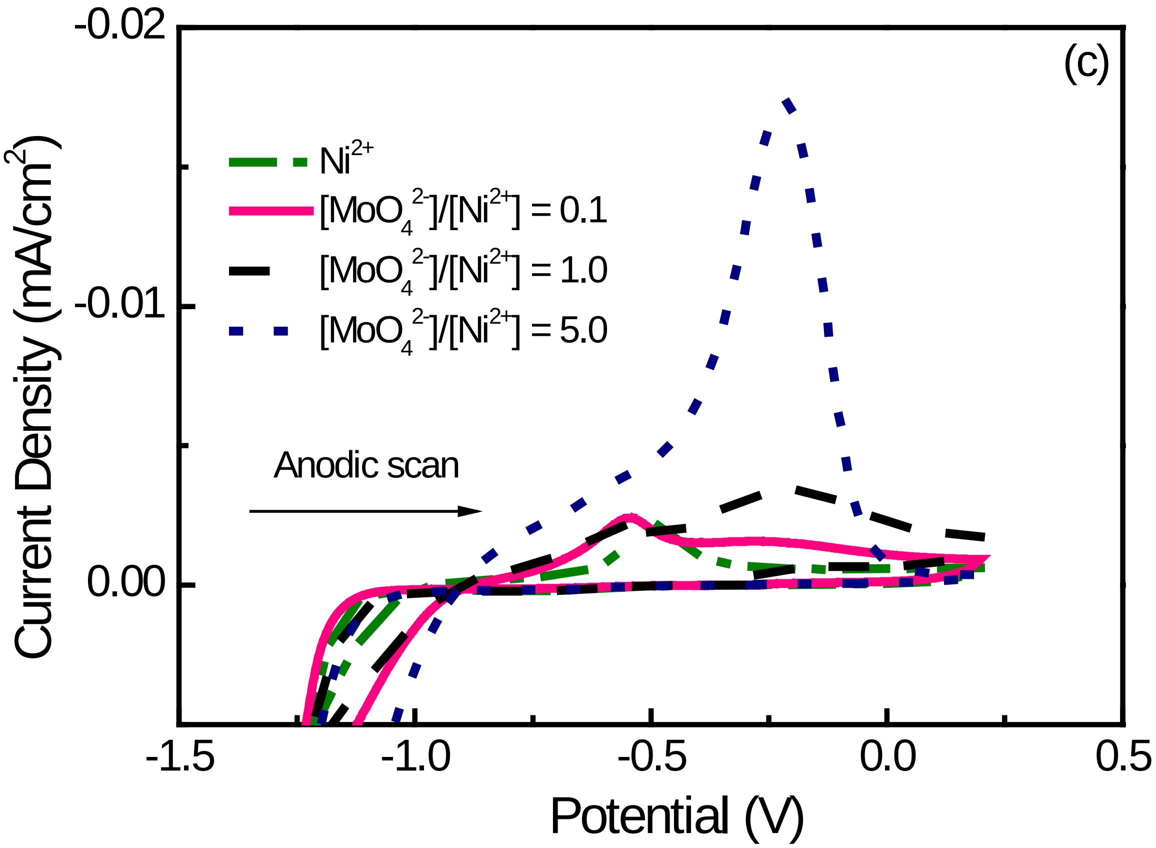

Figure 6.3: Cyclic voltammograms (zoom in on the anodic scan) of different [MoO_4^{2-}]/[Ni^{2+}] molar ratio (0.1, 1.0, and 5.0) compared to Ni^{2+} from citrate-borate plating solutions at pH 9.5.

Nickel and molybdenum were electrochemically co-deposited onto the steel cathode from the optimal solution of 0.1 M $NiSO_4{\cdot}7H_2O$, 0.1 M $Na_3C_3H_4(OH)(COO)_3$, 0.05 M H_3BO_3 and 0.01 M $Na_2MoO_4{\cdot}2H_2O$ by an alternating pulsed potential of -1.35 V/SCE and -0.7 V/SCE. The pulsed deposition enhanced the co-deposition process leading to smooth uniform nanocrystalline nickel-molybdenum alloy with less bubble occlusion in the film [40]. During pulsing back to the potential of -0.7 V, MoO_4^{2-} ions were increasingly induced co-deposited with Ni^{2+} ions due to increasing nickel ions concentration at the electrode/solution interface enhanced forming the nickel-molybdenum alloy at the potential of -1.35 V. It was found that only the [MoO_4^{2-}]/[Ni^{2+}] molar ratio of 0.1 and 0.2 were electrodeposited Ni-Mo alloys as film. When increasing [MoO_4^{2-}]/[Ni^{2+}]

molar ratio to 1 and 5, Ni-Mo alloys did not form as deposited films. Hence, the optimum solution of [MoO_4^{2-}]/[Ni^{2+}] molar ratio at 0.1 and 0.2 were used to elucidate film properties.

6.3.2 Film Characterization

The SEM image of a pure nickel deposit (Figure 5.4) was used to compare to the nickel-molybdenum alloy film. The morphology of nickel-molybdenum alloys deposited from the plating solution of [MoO_4^{2-}]/[Ni^{2+}] molar ratio of 0.1 and 0.2 are shown in Figure 5.5 and 5.6, respectively. They exhibited a crack-free nodular morphology composed of compact nanocrystalline grains.

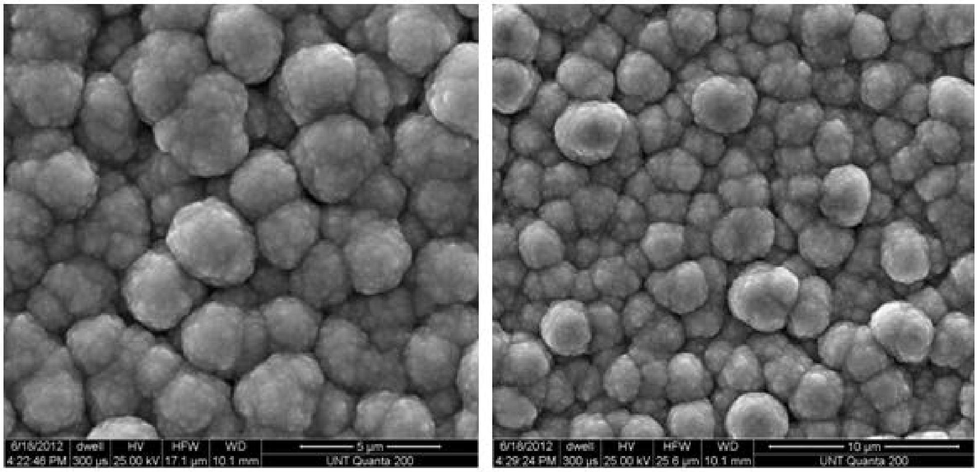

Figure 6.4: SEM images of pure nickel film at different magnifications (5 and 10 µm) deposited from nickel citrate-borate plating solution at pH 9.5.

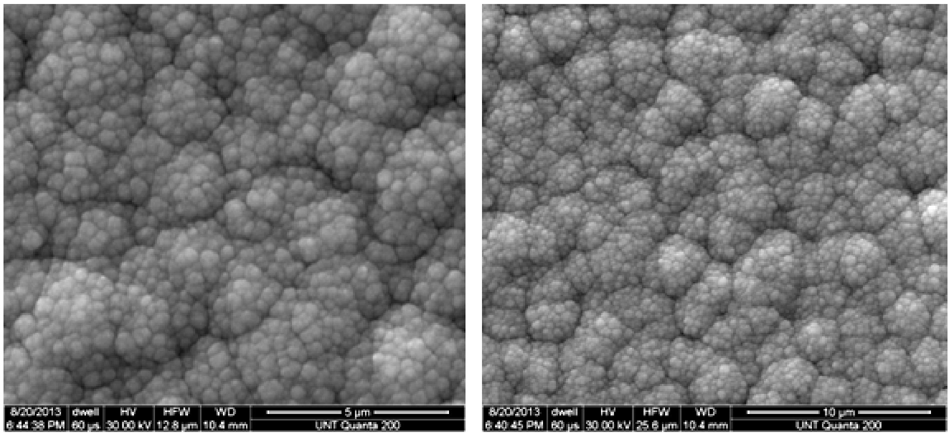

Figure 6.5: SEM images of nickel-molybdenum alloys at different magnifications (5 and 10 µm) deposited from citrate-borate electrolyte (pH 9.5) plating solution of the [MoO_4^{2-}]/[Ni^{2+}] molar ratio of 0.1.

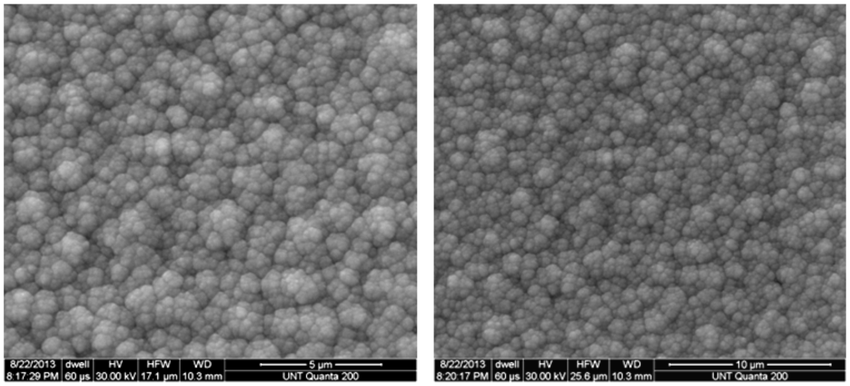

Figure 6.6: SEM images of nickel-molybdenum alloys at different magnifications (5 and 10 µm) deposited from citrate-borate electrolyte (pH 9.5) plating solution of the [MoO_4^{2-}]/[Ni^{2+}] molar ratio of 0.2.

The correlation between the molybdate-to-nickel molar ratio in the solution and chemical composition of the nickel-molybdenum film was determined by EDX (Figure 6.7 and 5.8) and AAS (Table 5.1). When increasing of molybdate/nickel molar ratio from 0.1 to 0.2 in the plating solution, the molybdenum content incorporated in nickel film increased from 15.5 to 28.5 % resulting in nickel relatively decreasing from 84.5 to 71.5 % (Figure 6.7 and 5.8 and Table 6.1). The elemental composition of the films measured by AAS are higher than that by EDX, which are 19.5% and 34.1 % for molybdenum in the films deposited from molybdate/nickel ratio of 0.1 and 0.2, respectively. Nickel contents in the films are relatively decreased from 80.5 to 65.9 % for those which electrodeposited from molybdate/nickel ratio of 0.1 and 0.2, respectively.

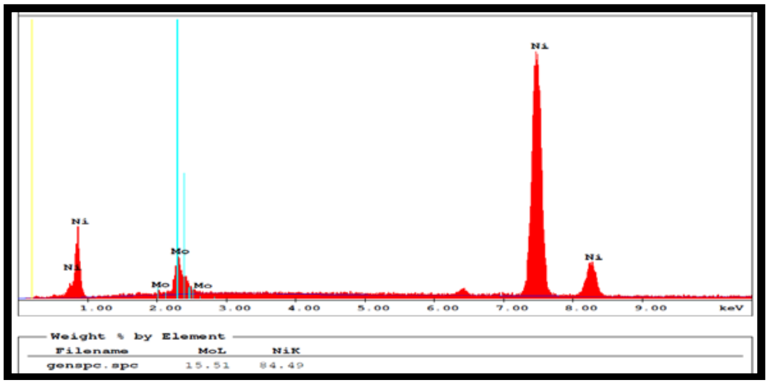

Weight % by Element

Filename	MoL	NiK
genspc.spc	15.51	84.49

Figure 6.7: EDX image of nickel-molybdenum alloys deposited from citrate-borate electrolyte (pH 9.5) plating solution of the [MoO_4^{2-}]/[Ni^{2+}] molar ratio of 0.1.

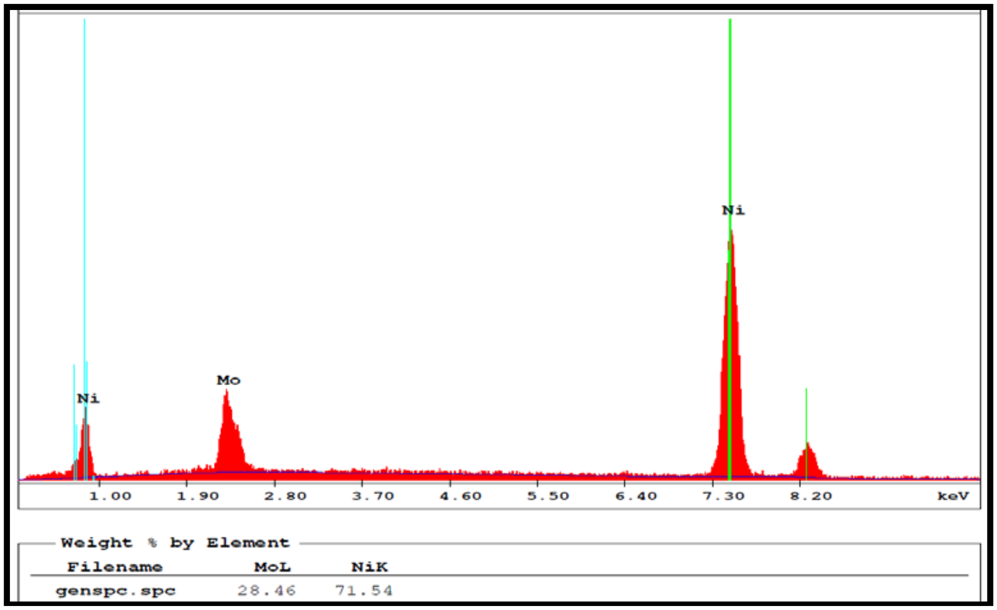

Weight % by Element

Filename	MoL	NiK
genspc.spc	28.46	71.54

Figure 6.8: EDX image of nickel-molybdenum alloys deposited from citrate-borate electrolyte (pH 9.5) plating solution of the $[MoO_4^{2-}]/[Ni^{2+}]$ molar ratio of 0.2.

Table 6.1: The elemental composition of the alloy films, deposited from different $[MoO_4^{2-}]/[Ni^{2+}]$ molar ratio of 0.1 and 0.2 plating solution (pH9.5), measured by AAS and EDAX

$[MoO_4^{2-}]/[Ni^{2+}]$ molar ratio	**Weight (%) by AAS (Avg. ± SD, n=3)**		**Weight (%) by EDX (Avg. ± SD, n=3)**		**Atomic (%) by EDX (Avg. ± SD, n=3)**	
	Ni	**Mo**	**Ni**	**Mo**	**Ni**	**Mo**
Pure Ni	100	–	100	–	100	–
0.1	80.5 ± 1.2	19.5 ± 1.1	85 ± 5	15 ± 3	90 ± 3	10 ± 2
0.2	65.9 ± 1.4	34.1 ± 0.9	72 ± 3	29 ± 2	80 ± 3	20 ± 3

The influences of the molybdate concentration in the nickel plating solution for electrodeposition of nickel-molybdenum alloys onto stainless steel substrates were evaluated by XRD for an optimal alloy structure. Nickel-molybdate alloys first deposited from a citrate bath at pH 9.5 are shown in figure 6.9. The scan represents the XRD patterns at different accumulative charges (20, 30 and 100 coulombs (C) onto stainless steel (SS). SS peaks appear in the XRD patterns at the low charges (20 C and 30 C), due to thin films, but disappeared at a higher charge of 100 C. The obtained coatings are uniform and adhered to the SS at low accumulated charges (20 C and 30 C).

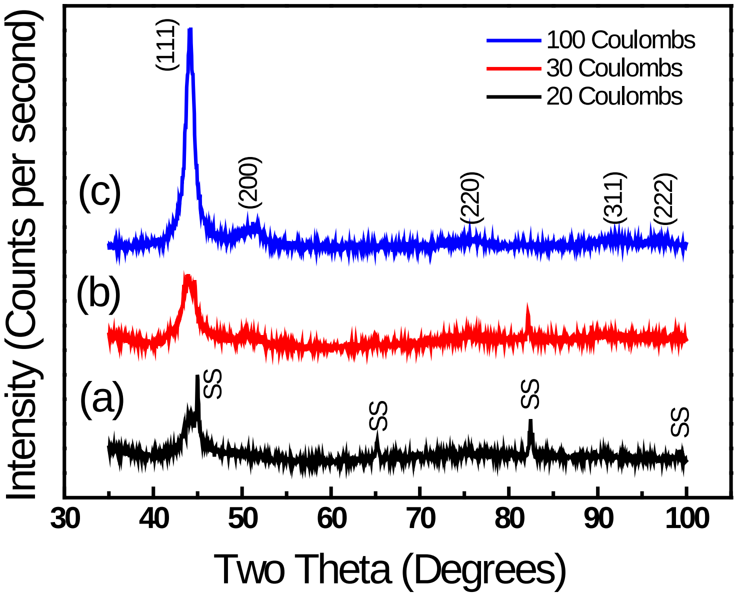

Figure 6.9: XRD patterns of nickel-molybdenum alloys deposited at different accumulation charges of (a) 20 (b) 30, and (c) 100 coulombs from plating solution of the [MoO_4^{2-}]/[Ni^{2+}] molar ratio of 0.1 in citrate electrolyte at pH 9.5.

The film coated at a higher accumulative charge (100 C) represented a thickness of around 10 microns (Figure 6.10) but had poor adhesion resulting in the coating peeling off by the tape test. Boric acid (0.05 M) was introduced into the nickel-molybdate citrate plating solution (pH 9.5) to enhance the adhesion of the coatings. Addition of 0.05 M boric acid into the nickel-molybdate-citrate plating solution exhibited the same XRD patterns of the saturated FCC alloy structure when compared to that without boric acid. The XRD patterns of nickel-molybdenum alloys from different [MoO_4^{2-}]/[Ni^{2+}] molar ratios (0.1 and 0.2) in the borate-citrate electrolyte were compared to the pure nickel deposit (Figure 6.11).

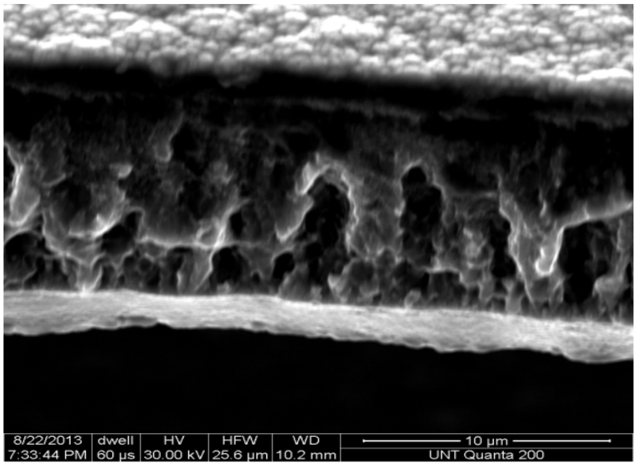

Figure 6.10: Film thickness of nickel-molybdenum alloys deposited at accumulation charges of 100 coulombs from plating solution of the $[MoO_4^{2-}]/[Ni^{2+}]$ molar ratio of 0.1 in citrate electrolyte at pH 9.5.

X-ray diffraction was used to examine the phase structure and crystallite size of the nickel-molybdenum alloy films obtained from $[MoO_4^{2-}]/[Ni^{2+}]$ molar ratios of 0.1 and 0.2 in borate-citrate solution. Figure 6.11 shows a typical XRD pattern of the electrodeposited nickel-molybdenum alloy films compared to a Ni film. The five characteristic peaks for nickel 44.45^o, 51.71^o, 76.41^o, 92.96^o, and 98.46^o (two theta), corresponding to Miller indices (111), (200), (220), (311), and (222), respectively, were observed, indicating that the resulting films are face-centered cubic (fcc). After comparing the experimental pattern to the JCPDS database (PDF #04-0850), the pattern matches that for randomly oriented nickel. The characteristic diffraction peaks of the face-centered-cubic nickel-molybdenum solid solution phase are at 43–44^o, 51^o, 74–75^o, 92–93^o, and 97–98^o (two theta), corresponding to Miller indices (111), (200), (220), (311) and (222), respectively. The XRD pattern of the nickel-molybdenum alloys deposited from different $[MoO_4^{2-}]/[Ni^{2+}]$ molar ratios of 0.1 and 0.2, shown in figure 6.11b and 5.11c, revealed that the peaks of 43–44°, 51°, and 74–75° (two theta) corresponding to the (111), (200), and (220) planes respectively, are broadened. This indicates that the electrodeposited nickel-molybdenum films were a single phase nickel-molybdenum crystal with a face-centered-cubic structure, where molybdenum replaced some nickel atoms in the fcc structure. Additionally, the increase of molybdenum content to [MoO_4^{2-}]/[Ni^{2+}] molar ratio of 0.2 in the plating solution resulted in peak intensity reduction and peak broadening. The coating structure with 0.2 molar ratio became amorphous with preferred (111) orientation. The (111) peak remained broadened while the other peaks begin to flatten.

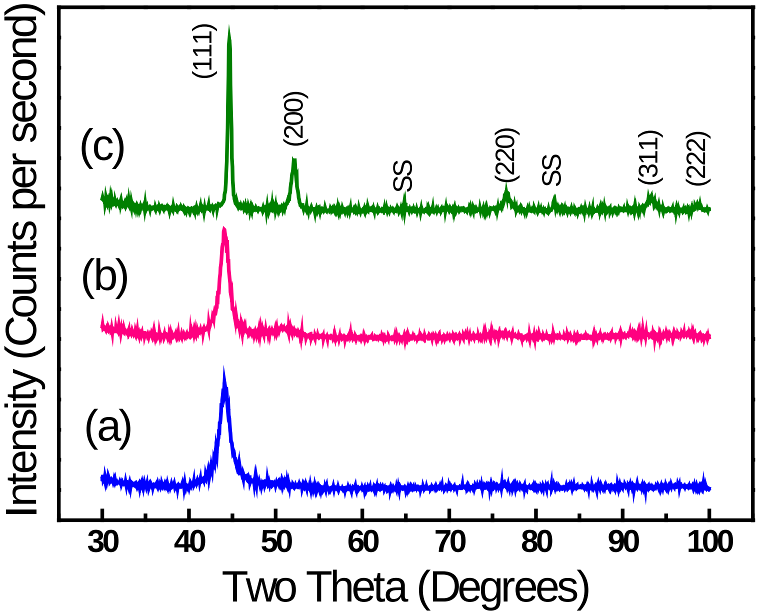

Figure 6.11: XRD patterns of nickel-molybdenum alloys electrodeposited from citrate-borate plating solution at different [MoO_4^{2-}]/[Ni^{2+}] molar ratios of (a) 0.1 (b) 0.2, and (c) pure nickel deposit.

The increase of the molar ratio from 0.1 to 0.2 increased the molybdenum content in the alloys from 15 to 29 percent (Table 6.1) based on analysis by EDAX. Nickel crystallite size shown in table 6.2 was calculated from Williamson-Hall plot shown in figure 6.12, a plot of $\beta_r \cos\theta$ versus $\sin\theta$ which yielded a straight line with a slope of η and intercept of $k\lambda/L$ [48, 49], while the nickel-molybdenum particle size was calculated by the Scherrer formula. As can be seen from the plot (Figure 6.11b and 5.11c), the only reflection (111) is the highest intensity peak for the nickel-molybdenum alloy. The synthesized nickel-molybdenum alloy particle size was compared to that of the nickel film. The calculating results shown in table 6.2 revealed that the particle size decreased with increase in the molybdate content in the plating solution. The increase of [MoO_4^{2-}]/[Ni^{2+}] molar ratio further enhanced the dissolution of molybdenum into the nickel grains resulting in reducing the particles to nanocrystalline or amorphous structure.

Table 6.2: The crystallite size measured by using the Williamson-Hall analysis from the XRD data of alloys obtained from plating solution of different [MoO_4^{2-}]/[Ni^{2+}] molar ratio of 0.1 and 0.2.

[MoO_4^{2-}]/[Ni^{2+}] molar ratio	Average particle size, nm
Pure Ni	19.8
0.1	6.4
0.2	5.6

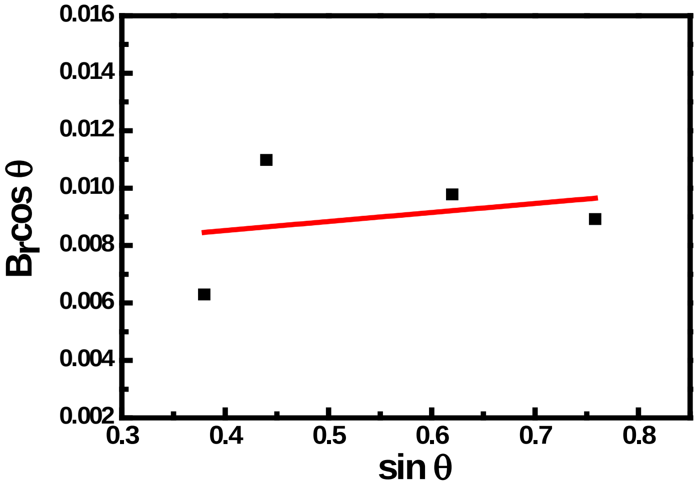

Figure 6.12: Williamson-Hall plot for XRD data of Ni film.

6.3.3 Corrosion Behavior

The potentiodynamic polarization curves of the electrodeposited nickel and nickel-molybdenum alloys in 3.5% NaCl solution are illustrated in figure 6.13. The electrochemical parameters including corrosion potentials, corrosion current, and the polarization resistance obtained from the Tafel plots are summarized in table 6.3. The molybdenum influence on the passive behavior of the nickel-molybdenum alloy (Figure 6.13) indicates that a wide passive region (-0.15-0.1 V/SCE) is exhibited on the alloy film as compared to the nickel film (-0.1-0.0 V/SCE).

The alloy containing molybdenum tends to retard corrosion better than the plain nickel film exhibited by the lower current density in the passive region. The beneficial effect of molybdenum incorporated into the nickel film is that the corrosion current density is lowered. Moreover, molybdenum in the alloy influences the anodic dissolution reaction by enhancing the growth of passive oxide film leading to a wider passivation region with higher molybdenum content [40-43]. The corrosion potential (E_{corr}) of the nickel-molybdenum alloy electrodeposited from the [MoO_4^{2-}]/[Ni^{2+}] molar ratio of 0.1 exhibited a more noble potential, shifted toward more positive values, compared to that of 0.2. Even though nickel film exhibited E_{corr} of -0.29 V, it showed the highest corrosion current density (i_{corr}) value of 0.316 μA cm^{-2} while nickel-molybdenum alloys give the corrosion potentials range from –0.33 to –0.47 V . Corrosion current density is the primary parameter used for evaluating the kinetics of the corrosion reaction. Lower corrosion current density leads to better corrosion protection. The corrosion current density for the nickel-molybdenum nanocrystalline coatings ranged from 0.100 to 0.040 μA cm^{-2}. The corrosion current density of the synthesized alloy was very low which shows better corrosion resistance. The alloy fabricated from the [MoO_4^{2-}]/[Ni^{2+}] molar ratio of 0.1 provides the highest polarization resistance (R_p) value of 1092 kΩ cm^2, implying a better corrosion resistance. In addition, the anodic polarization for the alloys fabricated from the 0.1 [MoO_4^{2-}]/[Ni^{2+}] molar ratio plating bath revealed a longer passivation region with lower current plateau than that obtained from the molar ratio of 0.15 and 0.2. Additionally, the R_p of the film that coated from the molar ratio of 0.15 showed lower value around 27 kΩ·cm^2 than that from the molar ratio of 0.1 and 0.2 bath. The R_p of the molar ratio of 0.15 is low due to much different values of β_a (5 V dec^{-1}) and β_c. (-24 V dec^{-1}) resulting in low value of R_p. The nickel-molybdenum alloy obtained from the ratio of 0.1 offers a better corrosion resistance based on to the lower current density and longer passivation region.

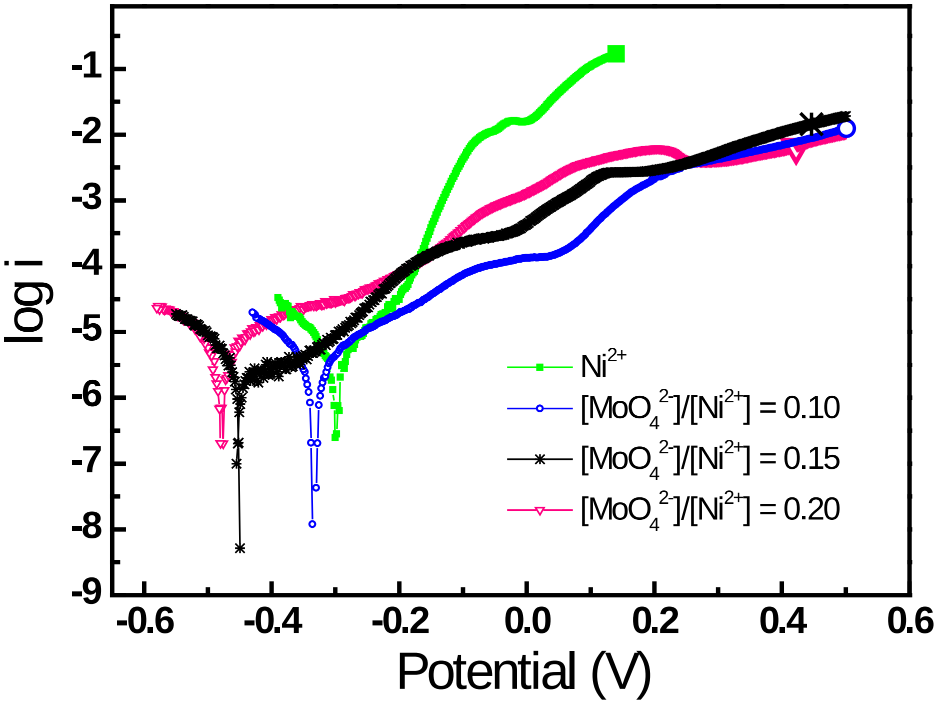

Figure 6.13: Tafel plot and anodic polarization of nickel-molybdenum alloy in 3.5% NaCl solution. The alloys were electrodeposited from citrate-borate plating solutions at different [MoO$_4^{2-}$]/[Ni^{2+}] molar ratios of 0.1, 0.15, and 0.2 compared to pure nickel deposit.

Table 6.3: E_{corr}, i_{corr} and R_p of the alloy film electrodeposited from the [MoO$_4^{2-}$]/[Ni^{2+}] molar ratios of 0.1, 0.15, and 0.2 and pure nickel film in the citrate-borate plating bath.

[MoO$_4^{2-}$]/[Ni^{2+}] molar ratio	**E_{corr} (V)**	**i_{corr} (μA cm^{-2})**	**R_p (kΩ cm^2)**	**$β_c$ (V dec^{-1})**	**$β_a$ (V dec^{-1})**
Pure Ni	-0.29	0.316	38.89	-18	11
0.1	-0.33	0.039	1092	-25	20
0.15	-0.45	0.102	27.46	-24	5
0.2	-0.47	0.100	486.9	-16	14

6.3.4 Mechanical Properties

The averaged Young's modulus and hardness data with standard deviation for each sample are represented in table 6.4. The modulus of the nickel-molybdenum alloys are 194 ± 35 and 189 ± 21 GPa for the molybdenum content of 15 and 29 weight percent, respectively. It is presented that the alloy synthesized from the ratio of 0.1 gives slightly higher modulus values with higher standard deviation than that of 0.2. Obviously, the synthesized alloys exhibited higher modulus values than the nickel film (143 ± 18 GPa). The hardness values of nickel-molybdenum alloy for the molybdenum content of 15 and 29 weight percent are 8.6 ± 1.5 and 8.8 ± 1.8, respectively, both of which are higher than that of the nickel film of 4.3 ± 1.7 GPa. The hardness of nickel-molybdenum alloys increased over nickel film due to the incorporation of high stiffness molybdenum metal into the nickel structure.

Table 6.4: The influence of $[MoO_4^{2-}]/[Ni^{2+}]$ molar ratio in the solution on the hardness and Young Modulus of the alloys (deposited of 100 C).

$[MoO_4^{2-}]/[Ni^{2+}]$ molar ratio	**Hardness (GPa ± SD, n=16)**	**Young modulus (GPa ± SD, n=19)**
0	4.3 ± 1.7	143 ± 18
0.1	8.6 ± 1.5	194 ± 35
0.2	8.8 ± 1.8	189 ± 21

6.4 Conclusion

Molybdenum is attractive to electrochemically co-deposit with nickel onto stainless steel to extend the lifetime of the steel in salt water brine environments. The synthesized alloy comprised of 15 weight percent molybdenum demonstrates improved corrosion resistance in 3.5% sodium chloride solution as compared to a pure nickel film. The corrosion current density is the principal parameter used for evaluating the kinetics of the corrosion reaction. The corrosion current density (i_{corr}) for the nanocrystalline nickel-molybdenum alloy coatings varied from 0.100 to 0.039 μA cm^{-2}. The alloy containing 15 weight percent molybdenum offered the highest polarization resistance (R_p) value of 1092 kΩ cm^2, exhibiting a better corrosion resistance. Though there is not a significant difference Young's modulus in the between 15 (194 GPa) and 29 (189 GPa) weight percent molybdenum, there is an obvious improvement when compared to the that of the pure nickel film (143 GPa). The hardness properties of the alloy containing 15 and 30 weight percent molybdenum exhibited the same range, 8.6 and 8.3 GPa, respectively, while both of the alloys offer increased hardness over the pure nickel film (4.3 GPa). The nickel-molybdenum alloys synthesized through modified pulsed potential electrochemical deposition at ambient temperature provided a better nanocrystalline coating and reduced grain size (5.6-6.4 nm) over nickel grain (19.8 nm) lead to improved corrosion resistance with enhanced mechanical properties. This work has shown that nickel-molybdenum alloys synthesized through electrochemical deposition techniques provide a superior nanocrystalline coating resulting in an improvement of both corrosion resistance and mechanical properties of the materials.

6.5 Chapter References

[1] L. Caceres, T. Vargas, L. Herrera, *Corrosion Science*. **2009**, 51, 971–978.

[2] Z. Cvijovic, G. Radenkovic, *Corrosion Science*. **2006**, 48, 3887–3906.

[3] A. J. Sedriks, *Corrosion of Stainless Steels*, Sponsored by The Electrochemical Society, Inc. Princeton, 2nd Ed., A Wiley-Interscience publication, John Willey & Sons, Inc.: New Jersey.

[4] R.H. Jung, H. Tsuchiya, S. Fujimoto, *Corrosion Science*. **2012**, 58, 62-68.

[5] Y.C. Lu, M.B. Ives, C.R. Clayton, *Corrosion Science*. **1993**, 35(1-4), 89-96.

[6] J.M. Bastidas, C.L. Torres, E. Cano, J.L. Polo, Corrosion Science. 2002, 44(3), 625-633. [7] W.J. Tobler,S. Virtanen, *Corrosion Science*. **2006**,48, 1585–1607.

[8] A.K. Mishra, D.W. Shoesmith, *Electrochimica Acta*. **2013**, 102, 328– 335.

[9] M.K. Ahn, H.S. Kwon, H.M. Lee, *Corrosion Science*. **1998**, 40(2-3), 307-322.

[10] G.O. Ilevbare, G.T. Burstein, *Corrosion Science.* **2001**, 43, 485-513.

[11] E. G´omez, E. Pellicer, M. Duch, J. Esteve, E. Vall´es, *Electrochimica Acta*, 51, 2006, 3214–3222.

[12] M. Karolus, E. Rówiński, E. Łągiewka, *Journal of Achievements in Materials and Manufacturing Engineering*. **2006**, 18(1-2), 119-122.

[13] R. Mishra, R. Balasubramaniam, *Corrosion Science*. **2004**, 46(12), 3019-3029.

[14] L. Wang , J. Zhang , Y. Gao , Q. Xue , L. Hu , T. Xu, *Scripta Materialia.* **2006**, 55(7), 657-660.

[15] R. Mishra, B. Basu, R. Balasubramaniam, *Materials Science and Engineering: A*. **2004**, 373(1-2), 370-373.

[16] K.M.S. Youssef, C.C Koch, P.S Fedkiw, *Corrosion Science*. **2004**, 46(1), 51–64.

[17] C.C. Koch, *J Mater Sci*. **2007**, 42, 1403–1414.

[18] Y. Xuetao, W. Yu, S. Dongbai, Y. Hongying, *Surface and Coatings Technology*. **2008**, *202*(9), 1895-1903.

[19] T. Ohgai, Y. Tanaka, R. Washio, *J. Solid State Electrochem.* **2013**, 17, 743–750.

[20] T. Haubold, R. Bohn, R. Birringer, H. Gleiter,Materials Science and Engineering: A. **1992**, 153(1-2), 679-683.

[22] W.Z. Friend, *Corrosion of nickel and nickel-base alloys.* Willey-Interscience: New York, 1980.

[23] E. Chassaing, M.P. Roumegas, M.F. Trichet, *Journal of Applied Electrochemistry*. **1995**, 25(7), 667-670.

[24] J. Crousier, M. Eyraud, J. -P. Crousier and J. -M. Roman, *Journal of Applied Electrochemistry*. **1992**, 22(8), 749-755.

[25] A. Brenner, *Electrodeposition of Alloys: Principles and Practice*, Academic Press, 1963.

[26] E.J. Podhala and D. Landolt, *J. Electrochem. Soc.* **1997**,144, 1672-1680.

[27] T. Ohgai, R. Washio, Y. Tanaka, *Journal of Electrochemical Socciety*. **2012**, 159(10), H00-H804.

[28] E.J. Podhala and D. Landolt, *J. Electrochem. Soc.* **1996**,143, 885-892.

[29] S. Sun, E. J. Podlaha, *Journal of Electrochemical Socciety*. **2012**, 159(2), D97-D102.

[30] E. J. Podlaha, D Landolt, *J. Electrochem. Soc*. **1996**, 143(3), 893-899.

[31] S. M.J. Ksycki, L. F. Yntema, *J. Electrochem. Soc.* **1949**, 48-56.

[32] T. A. Green, A. E. Russell, S. Roy, *Journal of the Electrochemical Society*. **1998**, 145(3), 875–881.

[33] C.-Q. Li, X.-H. Li, Z.-X.Wang, H.-J.Guo, *Transactions of Nonferrous Metals Society of China*. **2007**, 17(6), 1300–1306.

[34] O. Y. Zelenin, *Russian Journal of Coordination Chemistry*. **2007**, 33(5), 346–350.

[35] S. Rode, C. Henninot, M. Matlosz, *Journal of the Electrochemical Society*. **2005**, 152(4), C248-C254.

[36] E. Chassaing, M.P. Roumegas, M.F. Trichet, Journal of Applied Electrochemistry, **1995**, 25(7), 667-670.

[37] D. Landolt, A. Marlot, Surface and Coatings Technology, **2003**, 169-170, 8-13.

[38] A Marlot, P Kern, D Landolt, *Electrochimica Acta*. **2002**, 48(1), 29-36.

[39] N.S Qu, D Zhu, K.C Chan, W.N Lei, *Surface and Coatings Technology*. **2003**, 168(2-3), 123-128.

[40] S. Yagi, A. Kawakami, K. Murase, Y. Awakura, *Electrochimica Acta*. **2007**, 52, 6041-6051.

CHAPTER 7

ELECTRODEPOSITED NICKEL/MOLYBDENUM/LAYERED SILICATE NANOCOMPOSITES FOR ENHANCED CORROSION AND HARDNESS RESISTANCE

7.1 Introduction

This project focused on electrochemically depositing nickel-molybdenum-layered ceramic nanocomposites to improve corrosion protection and mechanical properties of the materials used in oilfield applications. In the oil field industry, high corrosion resistance and hardness are needed to extend the lifetime of currently used materials due to long term exposure in high stress and salt environments. Replacement or repair of corrosion damaged equipment is the largest maintenance expense for the oil and gas industry. This loss could be minimized with better materials, procedures, or designs through the use of presently available technology.

Recently, metal matrix composites (MMCs) have received high attention from investigators due to high stability, high temperature performance, good electrical and thermal conductivity, improved corrosion resistance and excellent wear and abrasion resistance which make them extraordinary candidates for a wide range of applications. These applications extend from aerospace and automotive [1,2], electronic packing [3,4] to thermal management equipments [5,6].

Different fabrication techniques are currently used to manufacture MMCs including thermal spraying, plasma spraying, hot isostatic pressing, chemical and physical vapor deposition but electrodeposition has advantages of being of low cost, high deposition rate and uniform distribution of particles within the metal-matrix [7].

Nickel and its alloys are featured matrix for MMCs as they possess high tensile strength and good corrosion resistance, they can disperse second phase particles to improve microhardness, yield and tensile strengths and wear resistance. Ni-Mo alloys and their derived composites are of great interest due to their high corrosion resistance and low overpotential for the hydrogen evolution reaction [8]. The preparation of Ni-Mo alloys by metallurgical methods was found to be inconvenient due to oxidation during the crystallization step and high melting point of molybdenum [9]. Other methods were utilized such as powder metallurgy and mechanical alloying [10,11], spark plasma sintering [12] and electrodeposition [13-15]. Several studies investigated the electrodeposition of Ni-Mo alloys [8,16-19].

Nickel is commonly used as a corrosion protective coating material. Molybdenum is advantageous to alloy with nickel because it is not as susceptible to pitting attack by chloride ions, leading to improved corrosion resistance. Nickel alloys containing 9-16% molybdenum are highly resistant to all forms of corrosion in seawater. Previous works have codeposited molybdenum with iron-group metals with various complexing agents and buffers to enhance the quality of the deposits. This work focuses on the electrodeposition of a nickel molybdenum alloy with incorporation of a ceramic material. The addition of ceramic filler was found to increase the hardness and extend the corrosion resistance of the alloy material.

Layered silicates are an attractive option as the ceramic source for incorporation into the metallic nickel-molybdenum alloy film to improve mechanical properties, such as hardness. Once the materials have high hardness, they are able to better resist stress cracking corrosion. In previous work, a method was developed to incorporate a layered silicate into an electrodepositing nickel film. When studied, it was found that the electrodeposited nickel/layered silicate nanocomposite exhibited increased corrosion resistance and hardness over pure nickel films [20-23].

Layered silicate nanoclays are ceramic materials which have several beneficial properties including high resistance to chemicals, pH, and temperature extremes as well as high surface area. Layered silicates have been used to reinforce several kinds of materials such as polymers [25-29] and ceramics [30-31] in order to improve the mechanical properties of the composite coatings. Researchers have shown that layered silicates enhanced corrosion resistance in conductive polymer composite coatings [32-33]. In addition, previous studies examining the incorporation of layered silicates in metals showed an increase in corrosion resistance and hardness of the resulting nanocomposite films [20-24].

Stainless steels, although highly corrosion resistant in a wide range of environments, are subject to corrosion when surrounded by chloride ions, such as in marine systems. Chloride damages various points on the passive film where the initiation of the pitting nuclei occurs. If the passivity is not regenerated, the reactions inside the pits propagate through an anodic process creating high acidity in the elevated chloride environment, eventually leading to overall structure failure [34-38]. Molybdenum has been used in stainless steels to protect against corrosion in aggressive chloride media systems [39-43]. Additionally, the presence of molybdenum improves mechanical properties of alloys [44].

Nickel provides high ductile ability and enhanced toughness. Hence, nickel is a typical metal to alloy with other metals to protect against corrosion in aggressive environments, elevated temperatures, or high stresses [52-53]. Molybdenum is alloyed with nickel to improve corrosion resistance, mechanical strength and heat stability of coatings. Nickel-base alloys containing 9-16 weight percent molybdenum exhibit high corrosion resistance against chloride attack [54-55]. In addition, molybdenum is another alternative component to alloy with nickel to replace toxic components such as chromium which have been previously used for improved mechanical properties of the nickel-based alloys. Several engineering material coatings including metals, ceramics, polymers, or composites have been fabricated by an electrodeposition method [45]. The electrodeposition technique provided superior nanocrystalline coatings with enhanced corrosion resistance and mechanical strength [46-53]. Nickel-molybdenum nanocrystalline coatings have been electrochemically deposited for various applications such as catalysts [52].

In this work, nickel-molybdenum alloy incorporated with layered silicate is electrochemically deposited onto stainless steel to improve corrosion resistance and strength of the coating as compared to nickel-molybdenum alloys. Citrate is used as complexing ligand and boric acid is an additive to improve adhesion. Nickel-molybdenum-layered silicate nanocomposites are electrodeposited under pulsed potentiostatic conditions from an alkaline plating bath containing molybdate (MoO_4^{2-}), nickel (II) ions and exfoliated layered silicate (montmorillonite) and adjusted to pH with ammonium hydroxide of the electrodeposited films. Viscosity, conductivity, zeta potential, and particle size were studied to understand the incorporation of exfoliated montmorillonite into the molybdate-nickel plating solution. X-ray diffraction (XRD) was used to analyze the crystal structure of the films and crystalline size. Surface morphology of the coating layers was studied by scanning electron microscopy (SEM). Energy dispersive X-ray (EDX) was used to estimate the amount of incorporated layered-silicate into the Ni/Mo nanocomposite coating by monitoring Al, Si, Mo, and Ni signals. Surface topography and heterogeneities of nickel/molybdenum and nickel/molybdenum/layered silicate were examined by atomic force microscopy (AFM). Corrosion resistance of the coating layers was configured in 3.5% NaCl solution using Tafel plot, potentiodynamic polarization, and electrochemical impedance techniques. Nanoindentation experiments were performed to measure hardness and Young Modulus of the films.

7.2 Experimental

7.2.1 Materials

Nickel-molybdenum-layered silicate nanocomposites were electrochemically deposited from alkaline plating baths at pH 9.5 and 25 °C. The layered silicate used for this work was monrmorillonite. The montmorillonite (MMT) was prepared as an aqueous suspension. The MMT (0.5, 1.0, and 2.0 g/L), obtained from Southern Clay Products was mechanically agitated using a magnetic stirrer for 24 hours to obtain exfoliated layered silicate platelets. Sodium citrate dihydrate was used as a ligand to stabilize nickel (II) and molybdate ions in solution. Boric acid was used as a buffer and to improve adhesion on stainless steel. The 100-mL nickel-molybdate plating baths were prepared from 2.63 g sodium sulfate, $NiSO_4 \cdot 6H_2O$ (Alfa Aesar), 0.24-0.48 g sodium molybdate, $Na_2MoO_4 \cdot 2H_2O$ (Alfa Aesar), 2.94 g sodium citrate, $C_3H_4(OH)(COONa)_3 \cdot 2H_2O$ (Fisher Scientific Company), and 0.31 g boric acid, H_3BO_3 (Alfa Aesar). The different $[MoO_4^{2-}]/[Ni^{2+}]$ molar ratios with various MMT concentration (0.5 g/L, 1.0 g/L and 2.0 g/L) are as shown in table 7.1.

Table 7.1: The bath composition of $[MoO_4^{2-}]/[Ni^{2+}]$ ratios with no MMT, 0.5 g/L, 1.0 g/L and 2.0 g/L MMT.

MMT Concentration (g/L)	**$[MoO_4^{2-}]/[Ni^{2+}]$ Mole Ratio**	
	0.1	**0.2**
None	0.01:1	0.02:1
0.5	0.01:1	0.02:1
1.0	0.01:1	0.02:1
2.0	0.01:1	0.02:1

All of the solutions are prepared from analytical-grade chemicals dissolved in de-ionized water. The solution pH is adjusted to 9.5 using ammonium hydroxide, NH_4OH (Fisher Scientific Company). The solutions are deaerated with nitrogen for 10 minutes before deposition. The nitrogen is slowly puffed to maintain N_2 in solution during deposition. A stainless steel type 304

($1.8\ cm^2$) disc was used as the cathode (working electrode) and platinum mesh is used as the anode (counter electrode) for electrodepositing the alloy, while a saturated calomel electrode is used as the reference electrode. The stainless steel discs are polished mechanically with 600, 800, and 1000 grit silicon carbide paper, then with 3 and 1 μm diamond solution on felt cloth. After the electrode is polished to a mirror-like finish, it is sonicated in deionized water for 10 minutes, degreased with ethyl alcohol, and rinsed with water. Before deposition the working electrode surface was activated by soaking in 1-5% HCl solution for 10 minutes and rinsed with water.

7.2.2 Electrodeposition and Solution Studies

7.2.2.1 Electrodeposition

An EG&G PAR Potentiostat/Galvanostat Model 273A was used for all depositions, cyclic voltammetry, and corrosion studies. Pulsed electrodeposition of the film was carried out using a potential of -1.35 V for 10 seconds then stepped to -0.7 V for 3 seconds and cycled until a total charge of 100 C was reached.

7.2.2.2 Solution Studies

Cyclic voltametry was used to investigate the electrodeposition potential of the nickel-molybdenum-layered silicates from a $[MoO_4^{2-}]/[[Ni^{2+}]$ molar ratio of 0.1 with varying concentrations of exfoliated MMT (0.5, 1.0, and 2.0 g/L) and compared to the $[MoO_4^{2-}]/[[Ni^{2+}]$ solution without MMT. As presented in chapter 5, different $[MoO_4^{2-}]/[Ni^{2+}]$ molar ratios of 0.1 and 0.2 were found to offer the best adhesion, corrosion resistance and hardness for nickel-molybdenum alloys. These ratios were then examined with incorporation of MMT to further improve these properties.

7.3 Results and Discussion

7.3.1 Electrodeposition and Solution Studies

7.3.1.1 Viscosity and Zeta-Potential Measurements

The influence of MMT concentration on the properties of Ni-Mo and Ni-Mo-MMT plating solutions were studied in order to get more information about solution dynamics of the electrocodeposition process. The viscosity, conductivity, zeta potential, and particle size were measured (Table 7.2). As the MMT concentration increased in the plating solution, the viscosity of the solution increased and the particle size increased from about 0.5 µm to 3-4 µm at higher concentrations due to platelets agglomeration. At pH 9.5 and given concentrations of Ni^{2+} and MoO_4^{2-}, the surface of MMT particles is negatively charged in the solution as appears from zeta potential values which ranges from -41.7 mV to -33.6 mV. The shift in zeta potential values towards more positive values with addition of Ni^{2+} ions can be attributed to the adsorption of positively charged Ni^{2+} ions onto the surface of MMT platelets which leads to the drop in surface charge. This drop results in consequent decrease in the electrostatic stabilization of particles and hence leads to agglomeration of particles and increases the solution viscosity. However, these values are still within the range for a stable electroplating solution.

From table 7.2, as the amount of the MMT particles in the plating solution was increased, the viscosity of the solution also increased slightly. The particle size of the MMT in the plating solution increased as the amount of MMT present increased. The particle size of the MMT in the 0.1 molybdate/nickel molar ratio solution appeared larger than that of the 0.2 ratio due to the larger amount of free nickel ions remaining in solution, which associate with MMT. When MMT concentration was high, the conductivity of MMT increased due to the high concentration of intercalated ions, such as sodium ions, present after the MMT was exfoliated as layered silicate platelets. The solution of MMT in the 0.2 molybdate/nickel ratio showed higher conductivity over that in the 0.1 ratio because there are a higher number of ions in the solution. The zeta potential values range from -33 to -42 mV. The particles were stable as suspended species in the plating solutions. This was also confirmed by observation of the plating baths which remained cloudy without precipitation when held at ambient temperature for 24 hours.

Table 7.2: The influence of MMT platelets on the [MoO_4^{2-}]/[Ni^{2+}] plating solution at 298 K.

[MoO_4^{2-}]/[Ni^{2+}] molar ratio	**MMT (g/L)**	**Viscosity (cSt, n=3)**	**Conductivity (mS/cm)**	**Particle size (nm)**	**Zeta potential (mV, n=3)**
None	0.5	0.912 ± 0.001	0.053	447	-41.7 ± 0.6
None	1.0	0.929 ± 0.002	0.106	553	-42.6 ± 1.4
None	2.0	1.001 ± 0.002	0.207	586	-39.6 ± 0.6
0.1	0.5	1.025± 0.000	25.06	3058	-34.0 ± 0.1
0.1	1.0	1.112 ± 0.003	25.24	3690	-37.1 ± 0.4
0.1	2.0	1.327 ± 0.001	25.29	4020	-35.0 ± 0.7
0.2	0.5	1.051 ± 0.002	25.54	2290	-32.8 ± 0.2
0.2	1.0	1.177 ± 0.003	25.85	2832	-33.6 ± 0.5
0.2	2.0	1.471 ± 0.011	25.92	3570	-34.8 ± 1.4

7.3.1.2 Electrochemical Study

The influence of MMT concentration on the electrocodeposition process was investigated by cyclic voltammetry. Figure 7.1 shows the electrochemical response for plating solutions containing different concentrations of the exfoliated layered silicate at a sweep rate of 50 mV s^{-1}. The voltammograms show no significant effect for the addition of MMT on the electrodeposition process. The cathodic peak appeared in the voltammetric curves at potentials below -0.8 V vs. SCE is probably attributed to nickel hydroxide deposition [56] and the reduction of polyvalent molybdenum oxides or hydroxide [57-60], whereas the deposition of the metal alloy or the nanocomposite takes place at more negative potentials simultaneously with hydrogen evolution reaction.

Molybdenum, which is not able to deposit alone in aqueous solution, has been electrochemically co-deposited with many iron metals [61-73]. Nickel-molybdenum co-deposition behavior is examined by cyclic voltametry on a molybdate/nickel 0.1 molar ratio solution. The various layered silicate concentrations (0.5, 1.0, and 2.0 g/L) were introduced into the molybdate/nickel plating solution to investigate the influence of layered silicate on the molybdate/nickel reduction and oxidation reaction by cyclic voltametric scan as shown in Figure 7.1. MMT slightly shifted the reduction potential of water to more negative potentials leading to a decrease in hydrogen evolution during deposition at high negative potentials such as in the range of -1.3 to -1.5 V/SCE (Figure 7.1).

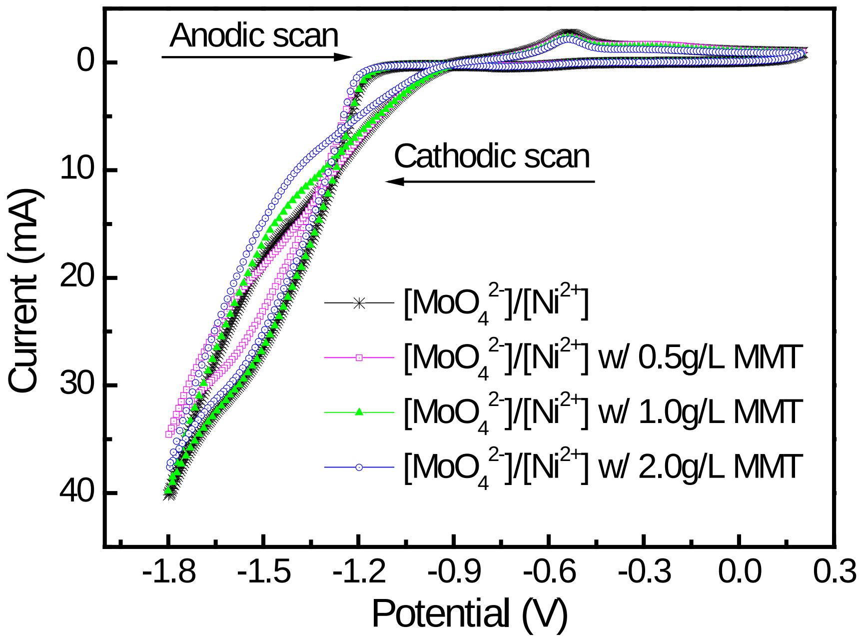

Figure 7.1: Cyclic voltammetry of $[MoO_4^{2-}]/[Ni^{2+}]$ molar ratio of 0.1 with no MMT, 0.5 g/L, 1.0 g/L, and 2.0 g/L MMT plating solution.

All cathodic scans of the molybdate/nickel ions with and without MMT show the reduction peak between -0.7 to -0.9 V/SCE (Figure 7.2). Nickel-molybdenum is co-deposited at the potential between -1.3 to -1.5 V/SCE where Ni^{2+}, MoO_4^{2-} ions, and water are discharged at the same time resulting in nickel-molybdenum film generation and hydrogen evolution. The electrodeposition of nickel/molybdenum without MMT evolves more hydrogen during the deposition than with MMT as can be seen from figure 7.1 and observed based on coating appearance. The film with 0.5 g/L MMT incorporated appears smoother and more uniform as compared to the one without MMT. The anodic scan of nickel/molybdenum exhibits two oxidation peaks. The first peak at -0.5 V/SCE is due to nickel dissolution. The second peak at around -0.3 V/SCE is due to the oxidation of molybdenum to form a molybdate species. At the potential of -0.3 V/SCE and pH 9.5, molybdenum metal is oxidized, forming molybdate species including MoO_2 and MoO_4^{2-} according to the Pourbiax diagram in chapter 1 (Figure 2.6a). When molybdenum metal is oxidized it does not generate Mo^{3+} ions except at pH values lower than 2. Therefore, the anodic scan results in the formation of molybdenum oxide species.

As shown in figure 7.2, MMT does not influence the reduction or oxidation potentials of the molybdenum-nickel alloy. However, MMT has a slight effect on the magnitude of the oxidation peak at -0.5 V/SCE, demonstrated by the reduction in current (Figure 7.2). The cyclic voltamogram of molybdate/nickel ions with 0.5 g/L MMT shows the highest oxidation current at -0.3 V/SCE due to creating the molybdate species.

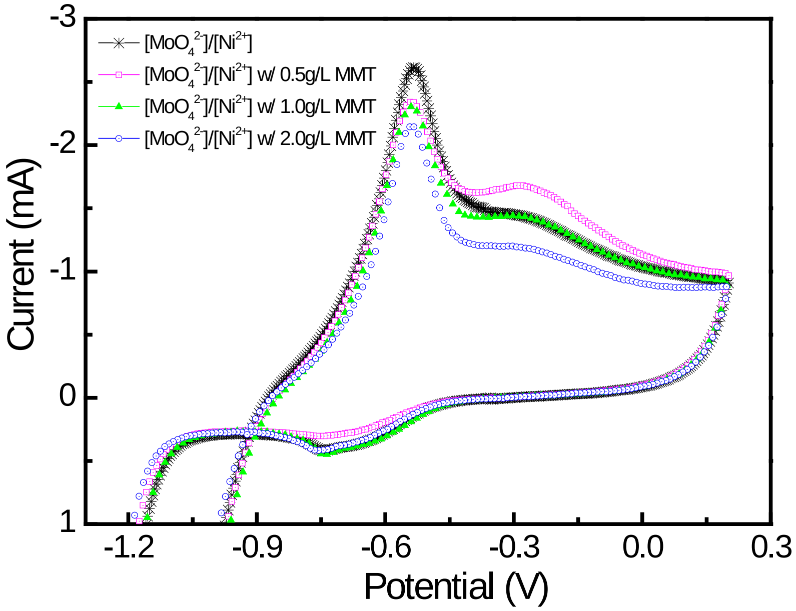

Figure 7.2: Cyclic voltammetry of [MoO_4^{2-}]/[Ni^{2+}] molar ratio of 0.1 with no MMT, 0.5 g/L, 1.0 g/L, and 2.0 g/L MMT plating solution.

Nickel/molybdenum/layered silicate was electrochemically co-deposited onto steel from the optimal solution of 0.1 M $NiSO_4 \cdot 6H_2O$, 0.1 M $Na_3C_3H_4(OH)(COO)_3$, 0.05 M H_3BO_3 and 0.01 M $Na_2MoO_4 \cdot 2H_2O$ by alternating pulsed potential of -1.35 V/SCE and -0.7 V/SCE. A cycle of the alternating pulsed deposition was started with the potential of -1.35 V, held for 10 seconds then pulsed back to the anodic potential of -0.7 V with the rate of 100 mV/s and held at the -0.7 V for 3 seconds. This was cycled through until the desired charge was obtained. The pulsed deposition enhanced the co-deposition process to obtain smooth uniform nanocrystaline nickel-molybdenum alloys with less bubble occlusion in the film. It was stated that the co-deposition of nickel-molybdenum by an alternating pulsed electrolysis process occurs through two electrochemical steps: anodic dissolution of nickel film and cathodic co-deposition of nickel-molybdenum alloys. The oxidized nickel ions surrounding the substrate during the anodic pulses (-0.7 V/SCE) induce

MoO_4^{2-} co-deposition with Ni^{2+} ions to form nickel-molybdenum alloy films during the cathodic pulses (-1.35 V/SCE).

Layered silicate nanoparticles were incorporated into the nickel/molybdenum film. MMT must be exfoliated in aqueous solution to obtain the individual layered silicate platelets. The platelets are nanoparticles which have an approximate thickness of 1 nm and effective diameter of 2 μm. MMT is not an electroactive species so no redox reaction occurs due to MMT during electrodeposition of the nickel-molybdenum alloy [20]. The exfoliated layered silicates are negatively charged particles. When incorporated into molybdate/nickel plating solutions, the platelets are countered with positive nickel ions and electrostatically adsorb onto the substrate during deposition [21]. The induced co-deposition of molybdenum with nickel in the citrate bath occurs by a 2-step reduction of molybdenum (i and ii) via a species of $[NiCitMoO_2]^-_{ads}$. Water molecules are simultaneously discharged at low potentials leading to hydrogen gas formation. In alkaline solutions, most of the citrate ligand is present as Cit^{3-} ions [65-68] and form complexes with nickel as $NiCit^-$ species. Some of the free nickel ions are available to associate with MMT. The following equation represented the mechanism of nickel/molybdenum induced codeposition.

(v) $NiCit^- + 2e^- \rightarrow Ni(s) + Cit^{3-}$ Eq. (6.1)

(vi) $MoO_4^{2-} + NiCit^- + 2H_2O + 2e^- \rightarrow [NiCitMoO_2]^-_{ads} + 4OH^-$ Eq. (6.2)

(vii) $[NiCitMoO_2]^-_{ads} + 2H_2O + 4e^- \rightarrow Mo(s) + NiCit^- + 4OH^-$ Eq. (6.3)

(viii) $2H_2O + 2e^- \rightarrow H_2 + 2OH^-$ Eq. (6.4)

7.3.2 Film Characterization

X-ray diffraction was used to examine phase structure and crystallite size of the nickel/molybdenum/layered silicate nanocomposite coatings obtained from different [MoO_4^{2-}

]/[Ni^{2+}] molar ratios (0.1 and 0.2) and various concentration of MMT (0.5, 1.0, and 2.0 g/L) incorporation. The X-ray diffraction patterns of Ni-Mo and Ni-Mo-MMT composite coatings prepared from deposition bath containing [MoO_4^{2-}]/[Ni^{2+}] molar ratio of 0. 1 are shown in figure. 6.3. The obtained XRD diffraction patterns were identical to solid solution of Mo in Ni i.e. Ni-Mo alloy. The incorporation of MMT into Ni-Mo matrix retarded the formation of the Ni-Mo alloy microcrystallites which is evident from reappearance of the reflection lines of pure Ni microcrystallites i.e. (200), (220), (311) and (222) reflections and increase its intensity with increasing the MMT content in the nanocomposite. It can be concluded from the observations that, the embedded layered silicate into the metallic matrix modifies the deposit texture from (111) in pure Ni-Mo to a mixed orientation along (111) as a main plane and other planes.

The vertical red lines indicate the face-centered cubic (fcc) standard nickel structure (JCPDS database (PDF #04-0850)) of the five characteristic peaks 44.45, 51.71, 76.41, 92.96, and 98.46 (two theta), corresponding to Miller indices (111), (200), (220), (311), and (222), respectively. Nickel-molybdenum-layered silicate nanocomposites electrodeposited from the plating solution of 0.1 [MoO_4^{2-}]/[Ni^{2+}] molar ratio and 2.0 g/L MMT matches the PDF #04-0850 file indicating the film retained the fcc structure observed without MMT incorporation. However, all peaks are slightly shifted to the left due to dissolved molybdenum in the solid nickel film and a change in the lattice parameters. The vertical black solid lines indicate the saturated fcc structure of the nickel-molybdenum alloy. Nickel-molybdenum solid solution without MMT shows the characteristic diffraction peaks of the saturated fcc phase at 43–44, 51, 74–75, (two theta), corresponding to planes: (111), (200), and (220), respectively. The XRD pattern of the nickel/molybdenum/layered silicate nanocomposite films deposited from 0.1 [MoO_4^{2-}]/[Ni^{2+}] molar ratio with 0.5 and 1.0 g/L MMT shown in figure 7.3, revealed that the peaks of 43–44, 51, and 74–75 (two theta) corresponding to the (111), (200), and (220) planes respectively are broadened and shifted to the left, showing the same pattern as the pure nickel-molybdenum alloy film. It is shown that introducing high MMT concentration into molybdate-nickel plating solution up to 2.0 g/L MMT lead to a lower incorporation of molybdenum in the alloy. The high MMT concentration may disturb the codeposition of molybdate as its deposits with nickel, leading to a weaker incorporation.

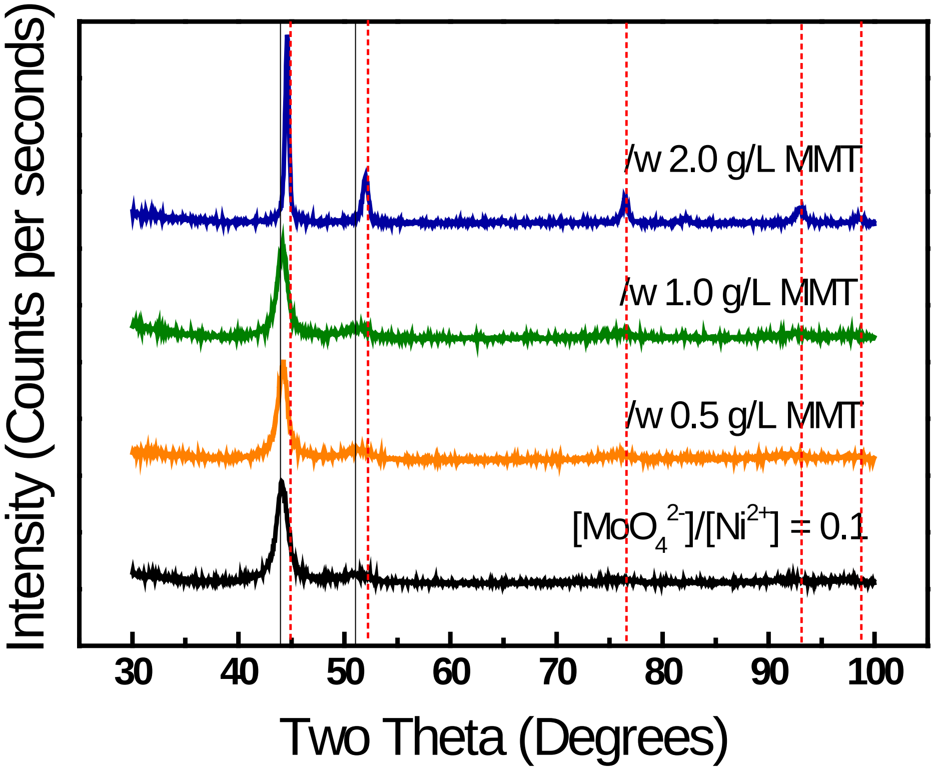

Figure 7.3: XRD patterns of nickel-molybdenum-layered silicate nanocomposites electrodeposited from plating solution of 0.1 [MoO$_4^{2-}$]/[Ni^{2+}] molar ratios with various MMT concentration of 0.5, 1.0, and 2.0 g/L incorporation.

According to figure 7.4, MMT concentration of 2.0 g/L in the plating bath with 0.2 [MoO$_4^{2-}$]/[Ni^{2+}] molar ratio lead to lower molybdenum content in the alloy than in the 0.1 molar ratio plating solution. The nickel-molybdenum-layered silicate nanocomposite film electrodeposited from the 0.2 [MoO$_4^{2-}$]/[Ni^{2+}] molar ratio plating solution incorporated with high

MMT concentration (2.0 g/L) shows all five peaks of the fcc nickel structure with slight left shifting. The plating solution of 0.1 molybdate/nickel molar ratio incorporated with 0.5 and 1.0 g/L MMT, and that of the 0.2 ratio with 0.5 g/L MMT resulted in a coating structure that was amorphous or nanocrytalline with only the preferred oriented (111) peak remaining with a broadened hollow shape, whereas the other peaks are flattened.

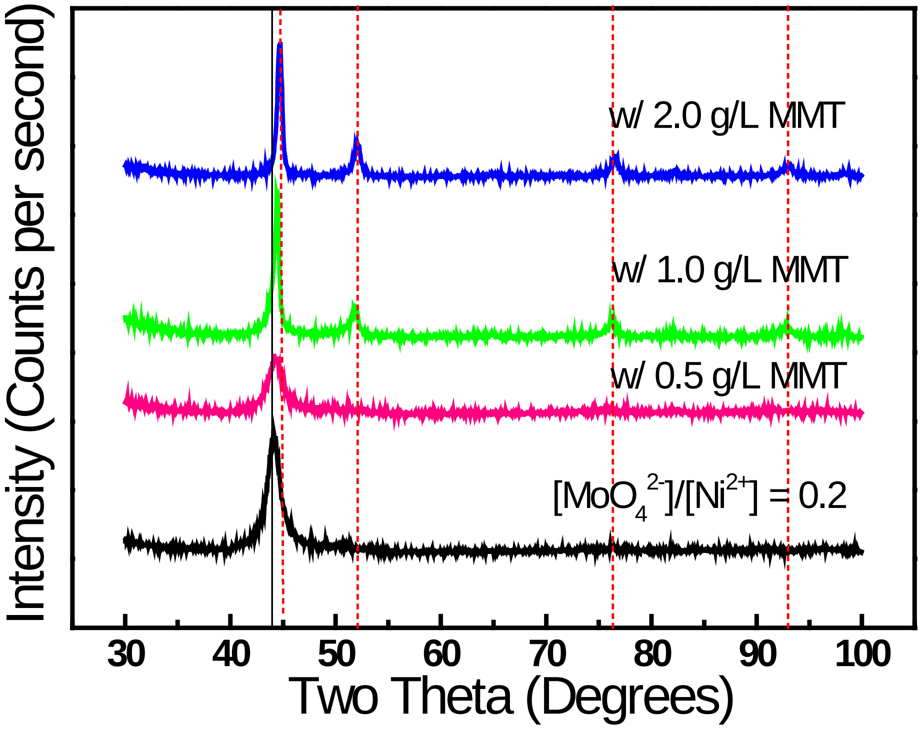

Figure 7.4: XRD patterns of nickel-molybdenum-layered silicate nanocomposites electrodeposited from plating solution of 0.2 $[MoO_4^{2-}]/[Ni^{2+}]$ molar ratios incorporated with various MMT concentration of 0.5, 1.0, and 2.0 g/L.

The crystallite size of different Ni/Mo/layered silicate nanocomposite films electrodeposited from plating baths with $[MoO_4^{2-}]/[Ni^{2+}]$ molar ratios of 0.1 and 0.2 reinforced with various MMT concentrations (0.5, 1.0, and 2.0 g/L) were compared with that of the Ni-Mo alloy electrodeposited from the same ratio (0.1 or 0.2) plating solution without MMT. The calculated values are shown in table 7.3. The five characteristic peaks correspond to Miller indices are (111), (200), (220), (311), and (222). The particle size of nickel/molybdenum/layered silicate composite film whose the characteristic peak represented a single broadening peak at the 2θ around 43–44° was calculated by Scherrer formula.

According to the calculated values of particle size, it is clear that the incorporation of MMT in the Ni-Mo matrix led to an increase in the particle size especially at high concentrations i.e. 2.0 g/l which resulted in an increase in the particle size to 21.9 nm and 16.6 nm for $[MoO_4^{2-}]/[Ni^{2+}]$ molar ratio 0.1 and 0.2, respectively. This increase in the particle size causes weakening of the grain refinement contribution to the hardness which explain the decrease in the hardness of Ni-Mo-MMT nanocomposite coating at 2.0 g/l MMT concentration.

Table 7.3: The particle size of molybdenum/nickel/layered silicate composites electrodeposited from plating baths with $[MoO_4^{2-}]/[Ni^{2+}]$ molar ratios of 0.1 and 0.2 reinforced with various MMT concentrations (0.5, 1.0, and 2.0 g/L).

MMT Concentration	**Particle size (nm)**	
	$[MoO_4^{2-}]/[Ni^{2+}] = 0.1$	**$[MoO_4^{2-}]/[Ni^{2+}] = 0.2$**
None	6.6	6.0
0.5 g/L	7.3	5.4
1.0 g/L	8.0	9.5
2.0 g/L	21.9	16.6

The particle size of the molybdenum/nickel/layered silicate which exhibited all five peaks of FCC structure: 44.45, 51.71, 76.41, 92.96, and 98.46 (two theta) was calculated from the Williamson-Hall plot. The Williamson-Hall plot for Ni/Mo/layered silicate nanocomposites electrodeposited from plating solution of $[MoO_4^{2-}]/[Ni^{2+}]$ molar ratio of 0.2 incorporated with 1.0 and 2.0 g/L MMT and from the plating solution of $[MoO_4^{2-}]/[Ni^{2+}]$ molar ratio of 0.1 incorporated with 2.0 g/L MMT are as shown in figures 6.5, 6.6, and 6.7, respectively. The five characteristic peaks correspond to Miller indices (111), (200), (220), (311), and (222), respectively. According to table 7.3, the increased molybdenum content in the alloy by adding more molybdate ions concentration (ratio 0.2) in the solution lead to smaller grain size (6 nm), compared with the ratio 0.1 (6.6 nm), corresponding to the more amorphous structure as shown in figure 7.3 and 6.4.

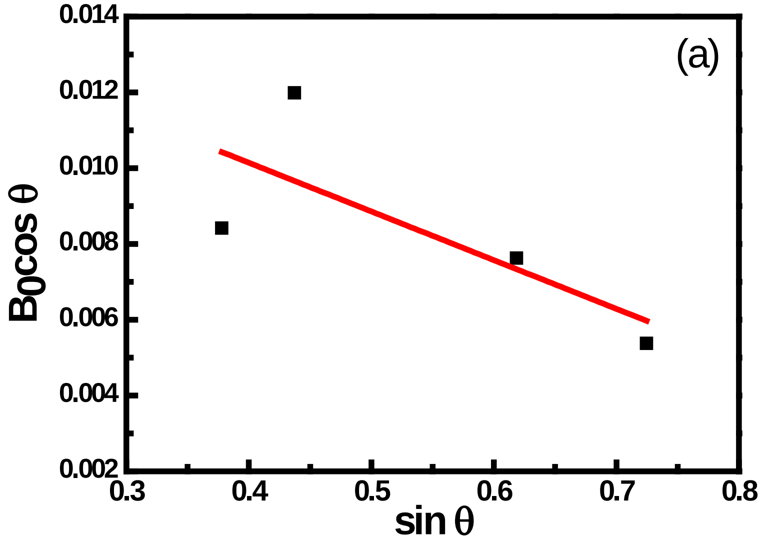

Figure 7.5: Williamson-Hall plot of a Mo/Ni/layered silicate film electrodeposited from a plating solution of [MoO_4^{2-}]/[Ni^{2+}] molar ratio of 0.2 incorporated with (a) 1.0 g/L MMT (Particle size of 9.5 nm).

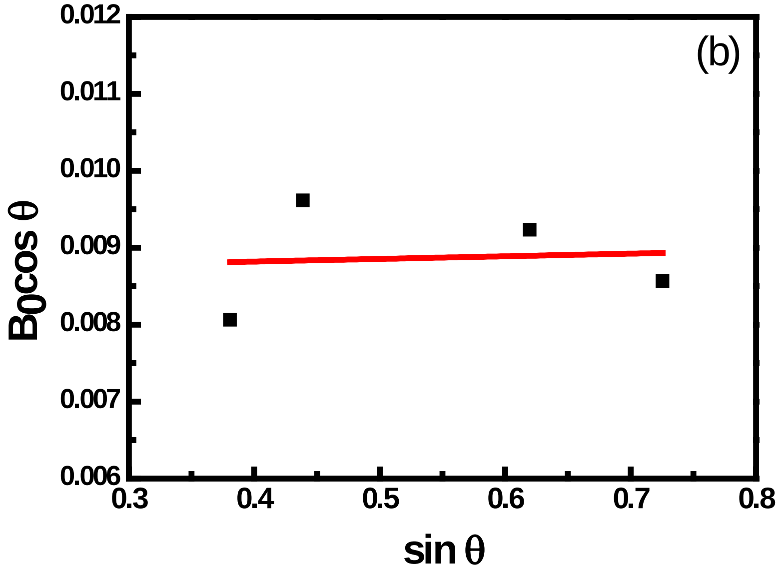

Figure 7.6: Williamson-Hall plot of a Mo/Ni/layered silicate film electrodeposited from a plating solution of [MoO_4^{2-}]/[Ni^{2+}] molar ratio of 0.2 incorporated with 2.0 g/L MMT (Particle size of 16.6 nm).

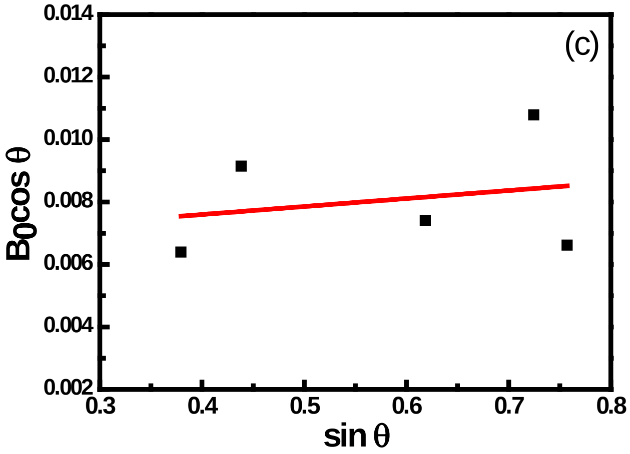

Figure 7.7: Williamson-Hall plot of a Ni/Mo/layered silicate film electrodeposited from a plating solution of [MoO_4^{2-}]/[Ni^{2+}] molar ratio of 0.1 incorporated with 2.0 g/L MMT (Particle size of 21.94 nm).

The induced co-deposition of molybdenum and nickel in a citrate bath is believed to occur by a 2-step reduction of molybdenum via a species of $[NiCitMoO_2]^-_{ads}$ as shown in the reactions, Eq. (6.2) and Eq. (6.3) [63-68].

When introducing MMT into the molybdate/nickel solution, the synthesized composites' particle sizes slightly increase. At the 0.1 ratio the particle sizes increase from 6.6 to 21.9 nm when the MMT concentration is raised from 0.5 to 2.0 g/L while at the 0.2 ratio the particle sizes increase from 6.0 to 16.6 nm when the MMT concentration is raised from 0.5 to 2.0 g/L. The resulting particle sizes are inversely proportional to the incorporation of MMT into the nickel matrix [21-23], hence, MMT does not affect nickel crystalline growth, but improves grain size. The incorporation of MMT may influence the molybdenum-nickel codeposition inhibiting the molybdenum reduction reaction at step (ii) or (iii) of Eq. (6.2) and Eq. (6.3), respectively. As a result the molybdenum content in the alloy is decreased with an increase in the amount of MMT in the plating solution (Table 7.4). To determine the amount of MMT incorporation in the coating, we can monitor the content of silicon and aluminum in sample through elemental analysis with

EDAX. As the amount of MMT in the plating solution is increased, the content of silicon and aluminum in the nanocomposites in increased, confirming a higher incorporation of MMT into the coating (Figure 7.8, Table 7.4). When the MMT concentration increases from 0.5 to 2.0 g/L, with the 0.1 $[MoO_4^{2-}]/[Ni^{2+}]$ molar ratio, silicon and aluminum content increases from 2.17 to 4.93 % and 1.94 to 3.00 %, respectively. In the 0.2 $[MoO_4^{2-}]/[Ni^{2+}]$ molar ratio, silicon and aluminum content increases from 2.84 to 5.21 % and 1.06 to 2.53 %, respectively. When raising the molybdate/nickel ratio from 0.1 to 0.2, the percent of molybdenum in the nanocomposites increases from 11.06 to 17.63 %, 10.64 to 16.69 %, and 9.50 to 12.36 % for the MMT concentrations of 0.5, 1.0, and 2.0 g/L, respectively. The increases of MMT concentration in the solution lead to reduced molybdenum content and elevated silicon and aluminum percentages in the nanocomposites, while nickel percentages stay relatively the same.

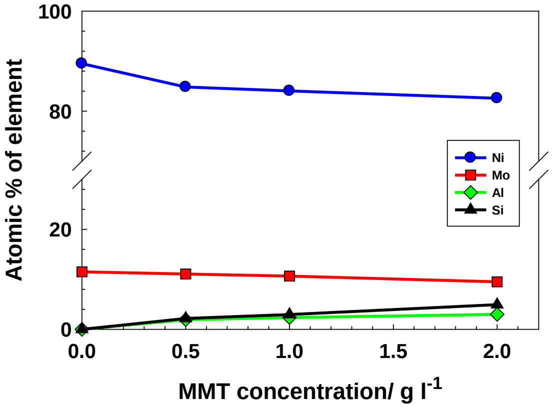

Figure 7.8: The variation of the atomic percentage of elements in Ni-Mo-MMT nanocomposite with the bath concentration of the layered silicate.

Table 7.4: The elemental composition of molybdenum/nickel/layered silicate nanocomposite films measured by EDX.

MMT Concentration	$[MoO_4^{2-}]/[Ni^{2+}] = 0.1$				$[MoO_4^{2-}]/[Ni^{2+}] = 0.2$			
	Elemental Composition (atomic %)							
	Al	Si	Mo	Ni	Al	Si	Mo	Ni
None	-	-	10.10	89.90	-	-	19.58	80.42
0.5 g/L	1.94	2.17	11.06	84.83	1.06	2.84	17.63	78.47
1.0 g/L	2.35	2.96	10.64	84.05	2.27	3.03	16.69	78.01
2.0 g/L	3.00	4.93	9.50	82.57	2.53	5.21	12.36	79.90

7.3.3 Surface Morphology and Topography

The surface morphologies of electrodeposited Ni/Mo/layered silicate films exhibit fine grains and smooth surfaces as shown by SEM in figures 6.9-6.10. The films exhibited a crack-free nodular morphology composed of compact nanocrystalline grains. The SEM image of nickel/molybdenum alloy (without MMT incorporation) (Figure 6.9a) electrodeposited from a plating solution of 0.1 $[MoO_4^{2-}]/[Ni^{2+}]$ molar ratio is compared with the nickel/molybdenum/layered silicate nanocomposites film incorporated with different MMT concentration of 0.5, 1.0, and 2.0 g/L as shown in figure 7.9b, 6.9c, and 6.9d, respectively.

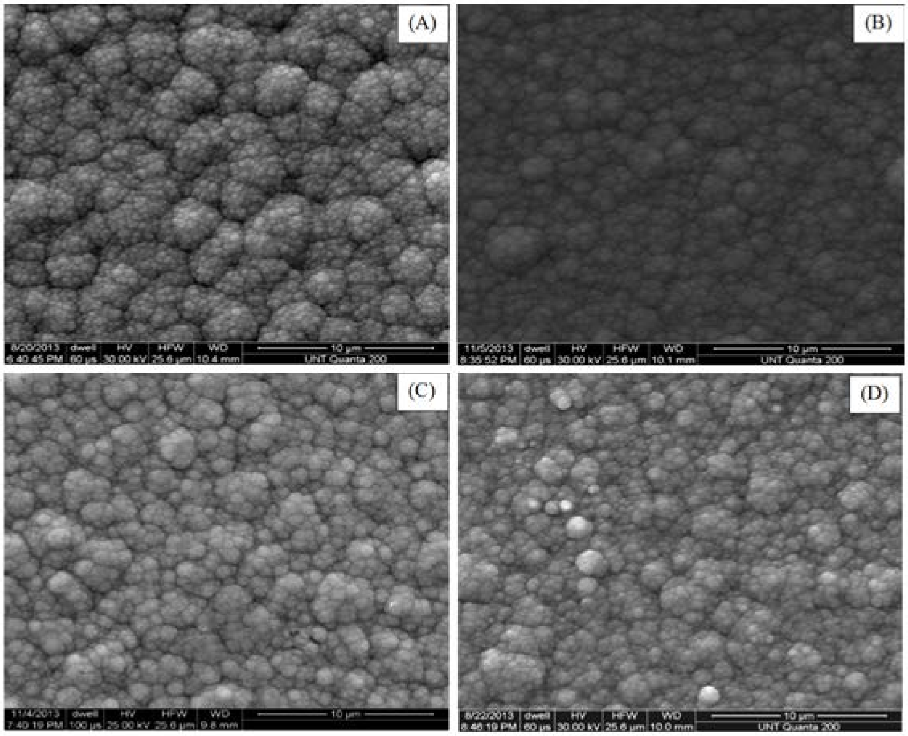

Figure 7.9: SEM images of a nickel/molybdenum alloy film electrodeposited from (a) $[MoO_4^{2-}]/[Ni^{2+}]$ molar ratio of 0.1 plating solution and that incorporated with different MMT concentration of (b) 0.5 g/L, (c) 1.0 g/L, and (d) 2.0 g/L

The SEM image of the nickel/molybdenum alloy deposit (Figure 6.10a) electrodeposited from plating solution of 0.2 $[MoO_4^{2-}]/[Ni^{2+}]$ molar ratio is compared with the nickel/molybdenum/layered silicate nanocomposites film incorporated with different MMT concentration of 0.5, 1.0, and 2.0 g/L as shown in figures 6.10b, 6.10c, and 6.10d, respectively.

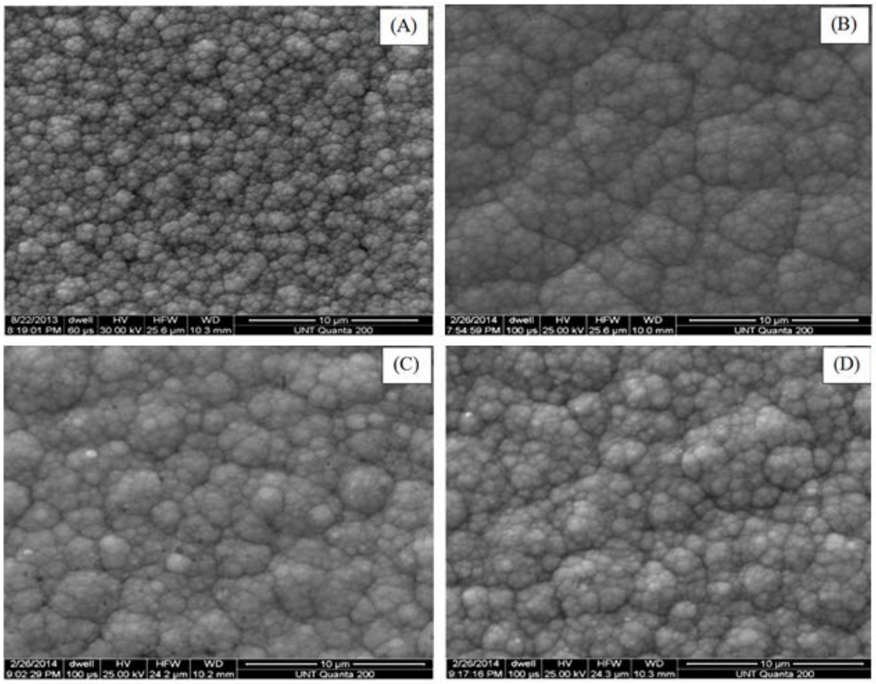

Figure 7.10: SEM images of a nickel/molybdenum alloy film electrodeposited from (a) [MoO_4^{2-}]/[Ni^{2+}] molar ratio of 0.2 plating solution and that incorporated with different MMT concentration of (b) 0.5 g/L, (c) 1.0 g/L, and (d) 2.0 g/L.

Figure 7.11 shows the AFM micrographs of Ni-Mo and Ni-Mo-MMT nanocomposite coatings. It can be seen that, there is an increase in the size of the domed structure and the surface roughness with increasing the content of layered silicate in the nanocomposite coatings. The surface roughness was expressed by an average deviation parameter (R_a). This value gives the average height of irregularities in the perpendicular direction to the surface. The surface of pure Ni-Mo was relatively smooth which is evident from its low value of R_a i.e. 7.83 nm but this value is significantly increased from to 17.39, 20.05 and 25.19 for Ni-Mo-0.5MMT, Ni-Mo-1MMT and Ni-Mo-2MMT, respectively.

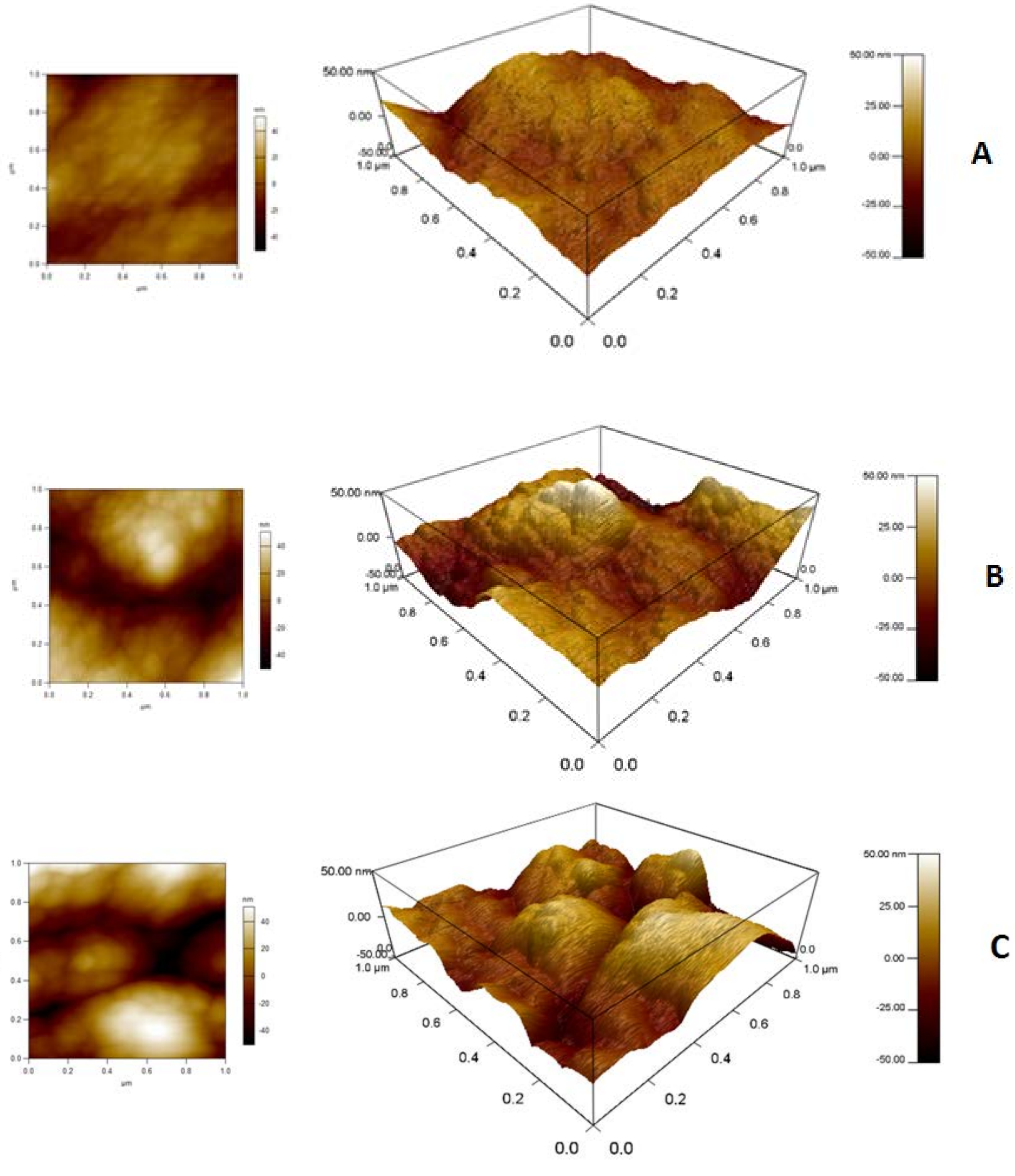
50.00 nm
0.00
-50.00
1.0 µm
0.8
0.6
0.4
0.2
0.0
0.0
1.0 µm
µm
nm
50.00 nm
25.00
0.00
-25.00
-50.00
A
B
C

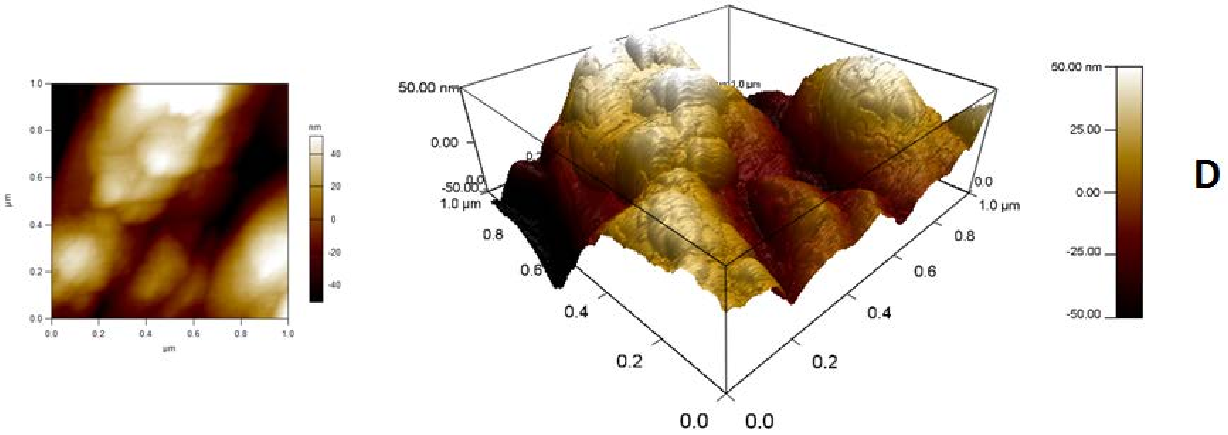

Figure 7.11: AFM micrographs of (a) Ni-Mo and Ni/Mo/layered silicate nanocomposite coatings (b) 0.5, (c) 1.0, and (d) 2.0 g/L MMT concentration prepared from plating solutions containing $[MoO_4^{2-}]/[Ni^{2+}]$ ratio of 0.1

7.4 Corrosion Behavior of Ni-Mo-MMT Nanocomposites

7.4.1 Potentiodynamic Polarization Measurements

In order to investigate the corrosion resistance of the Ni-Mo-layered silicate coatings as compared to that of pure Ni-Mo, the corrosion behavior of both types of coatings was studied in 3.5% NaCl solution using both polarization and impedance techniques. Figure 7.12 and 6.13 show the Tafel polarization curves of Ni-Mo and different Ni-Mo-MMT nanocomposite coatings after 24h immersion in 3.5% NaCl solution. The corrosion parameters are given in table 7.5. The calculated values of the polarization resistance showed an improvement in the corrosion resistance of the nanocomposite coating compared to pure Ni-Mo alloy. This improvement in the corrosion resistance of the nanocomposite was attributed to two main reasons; the first is that the incorporation of an inert phase into the metal matrix constitutes a physical barrier that inhibits the initiation and propagation of the defect corrosion. Secondly, the dispersion of MMT particles forms micro-corrosion cells that facilitate the anodic polarization and retards the localized corrosion [86-88].

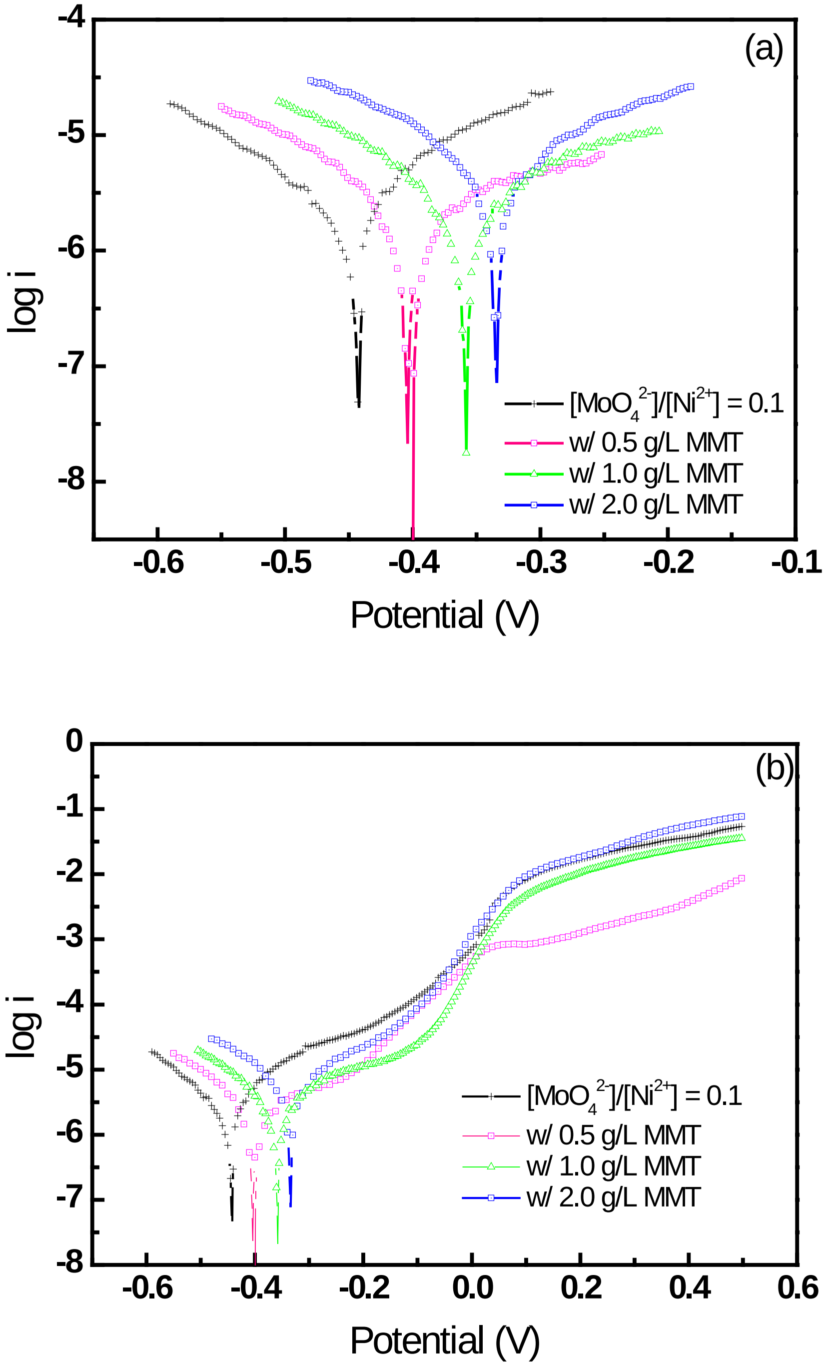

Figure 7.12: Tafel plots (a) and potentiodynamic polarization measurements (b) in 3.5% NaCl of nickel/molybdenum alloys electrodeposited from 0.1 $[MoO_4^{2-}]/[Ni^{2+}]$ molar ratio with various MMT concentrations of 0.5, 1.0, and 2.0 g/L MMT incorporated in the plating solution**.**

Tafel plots and potentiodynamic polarization curves of the electrodeposited nickel/molybdenum/layered silicate nanocomposites compared with nickel/molybdenum alloys were measured in 3.5% NaCl solution as illustrated in figures 6.12 and 6.13. The electrochemical parameters including corrosion potentials, corrosion current, and polarization resistance obtained from the Tafel plots are summarized in table 7.5. Molybdenum influences the passive behavior of the nickel/molybdenum/layered silicate nanocomposite. The nanocomposites with 0.5 g/L MMT incorporation (Figure 7.12b and 6.13b) show the widest passivation region (0.0-0.5 V/SCE) with the lowest current density. Molybdenum in the films influences the anodic dissolution reaction by enhancing passive oxide film growth [18,69,70,72]. Although the nanocomposites with 0.5 g/L MMT (in the 0.1 or 0.2 [MoO_4^{2-}]/[Ni^{2+}] molar ratios contained lower molybdenum percent than that without MMT, the passivation region was improved as compared to the pure nickel/molybdenum alloy. This may be the result of the smoother packed grain of the films. The molybdenum content in the film with an MMT concentration of 0.5g/L is adequate to resist corrosion. The nickel/molybdenum/layered silicate nanocomposite films also have lower current densities than that of their corresponding pure nickel/molybdenum alloy films (for both of the molar ratios, 0.1 and 0.2) as shown in figure 7.12b and 6.13b. This confirms that the incorporated layered silicates in the nickel/molybdenum nanocomposites enhanced corrosion protection. For the ratio of 0.2, the corrosion potential (E_{corr}) of the nickel/molybdenum/layered silicates nanocomposites showed an improved noble potential, shifted toward more positive potentials from -0.42 to -0.34 V/SCE (Table 7.5 and Figure 7.17a and 6.18a) as the MMT concentration was increased from 0.5, 1.0, and 2.0 g/L, respectively while the E_{corr} for the alloy is -0.47 V/SCE. The nanocomposite film fabricated from the incorporation of 0.5 g/L MMT into the 0.2 [MoO_4^{2-}]/[Ni^{2+}] ratio offered the lowest corrosion current density (i_{corr}) value of 0.631 μA cm^{-2} and has the highest polarization resistance (197.5 kΩ cm^2). Corrosion current density is the primary parameter used for evaluating the kinetics of the corrosion reaction. Lower corrosion current density leads to a better corrosion protection. The corrosion current density for the nickel/molybdenum/layered silicate nanocomposite coatings ranged from 0.631 to 1.00 μA cm^{-2}. The corrosion protection of nickel/molybdenum/layered silicate nanocomposite films fabricated from 0.1 [MoO$_4^{2-}$]/[Ni^{2+}] molar ratio with MMT concentrations of 0.5, 1.0, and 2.0 g/L bath show the same tendency as the 0.2 [MoO$_4^{2-}$]/[Ni^{2+}] molar ratio, as shown in table 7.5.

Table 7.5: Corrosion potential (E$_{corr}$), corrosion current density (i$_{corr}$) and polarization resistance (Rp) of the nickel/molybdenum alloy and their layered silicate nanocomposite films incorporated with various MMT concentrations (0.5, 1.0, and 2.0 g/L).

Plating solutions		**E$_{corr}$ (V)**	**i$_{corr}$ (μA cm^{-2})**	**Rp (kΩ cm^2)**
[MoO$_4^{2-}$] / [Ni^{2+}] mole ratio of	[MoO$_4^{2-}$]/[Ni^{2+}] = 0.2	-0.47	2.00	80.0
	w/ 0.5 g/L MMT	-0.42	0.631	197.5
	w/ 1.0 g/L MMT	-0.36	1.00	107.0
	w/ 2.0 g/L MMT	-0.34	1.26	87.8
[MoO$_4^{2-}$] / [Ni^{2+}] mole ratio of	[MoO$_4^{2-}$]/[Ni^{2+}] = 0.1	-0.46	5.70	67.7
	w/ 0.5 g/L MMT	-0.40	0.131	217.9
	w/ 1.0 g/L MMT	-0.35	1.70	73.4
	w/ 2.0 g/L MMT	-0.33	6.34	32.6

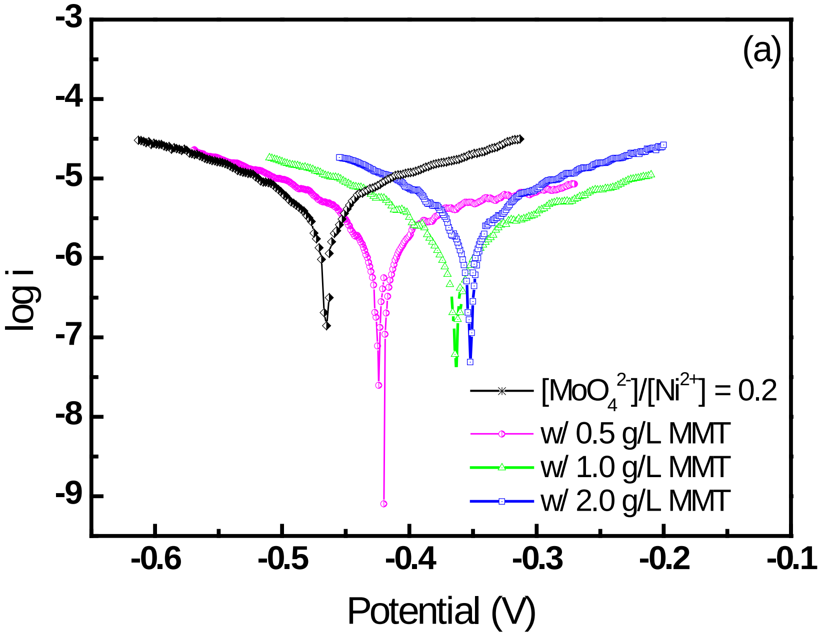

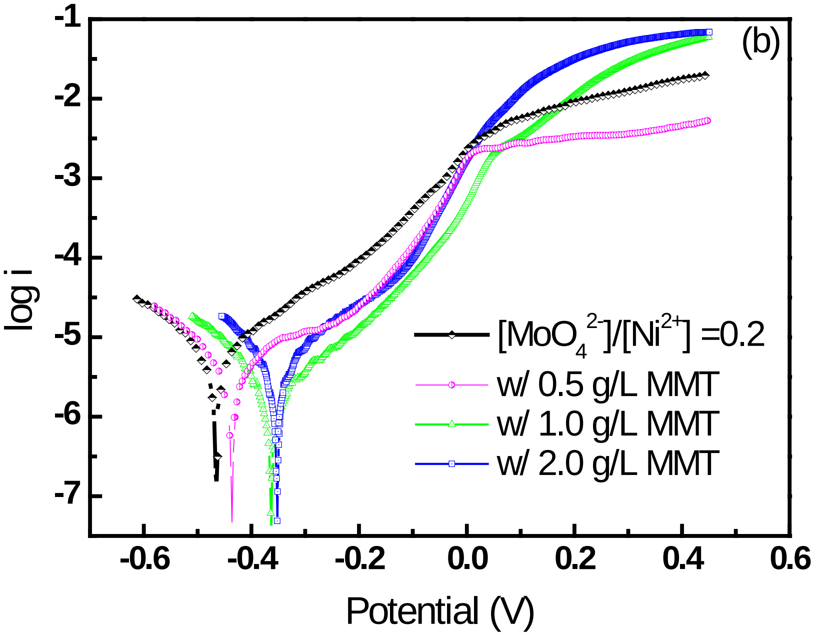

Figure 7.13: Tafel plots (a) and potentiodynamic polarization measurements (b) in 3.5% NaCl of nickel/molybdenum alloys electrodeposited from 0.2 $[MoO_4^{2-}]/[Ni^{2+}]$ molar ratio with various MMT concentrations of 0.5, 1.0, and 2.0 g/L MMT incorporated in the plating solution.

7.4.2 Electrochemical Impedance Measurements

Nyquist impedance plots of Ni-Mo and Ni-Mo-0.5 MMT nanocomposite coatings after 24h of immersion in 3.5 % NaCl solution are given in figure 7.14a. The diameter of the semicircle is much higher for the nanocomposite coating as compared to pure Ni-Mo alloy which confirms higher resistance for the nanocomposite. Figure 7.14b represents Bode impedance plots of Ni-Mo and different Ni-Mo-MMT nanocomposite coatings after 24h of immersion in 3.5 % NaCl solution. The data confirms the presence of two time constants for the electrode/electrolyte interface in NaCl solution. The experimental data were analyzed and fitted according to the equivalent circuit model shown in figure 7.15. The model consists of a solution resistance (Rs), R_1Q_1 couple which represents the resistance and capacitance of the double layer, and R_2Q_2 which refers to the passive layer resistance. The fitting procedure shows good coincidence between the measured and simulated values.

The equivalent circuit parameters are shown in table 7.6. These parameters showed that the passive layer resistance, R_2 of Ni-Mo-MMT nanocomposite coatings is much higher than pure Ni-Mo which is consistent to the results obtained from polarization measurements.

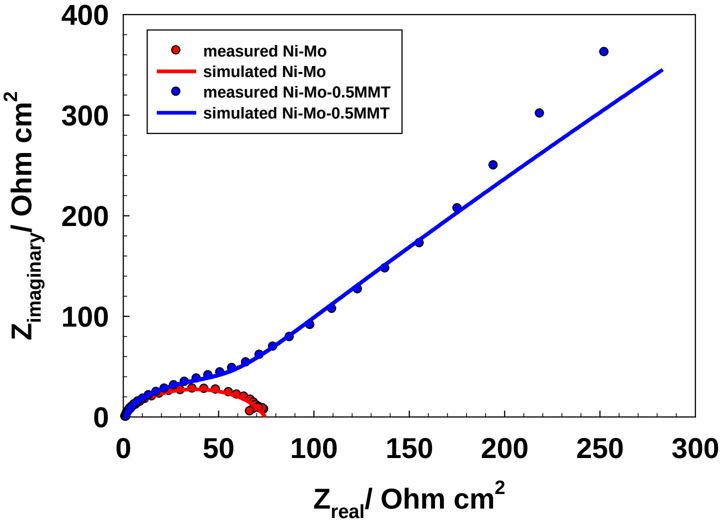

a: Nyquist impedance plot.

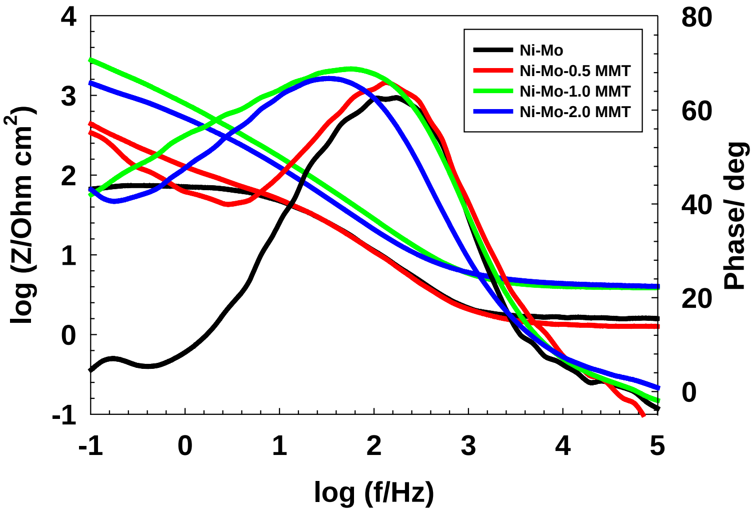

b: Bode impedance plots.

Figure 7.14: plots of Ni-Mo and Ni-Mo-0.5MMT after 24h of immersion in 3.5 % NaCl solution.

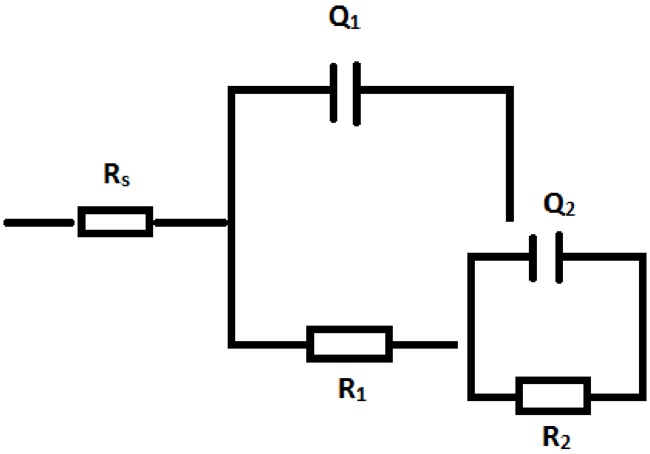

Figure 7.15: Equivalent circuit model representing the electrode/electrolyte interface of Ni/Mo and Ni/Mo/MMT nanocomposite coatings in 3.5% NaCl solution.

Table 7.6: Equivalent circuit parameters of pure Ni/Mo and different Ni/Mo/layered silicate nanocomposite films after 24h immersion in 3.5 % NaCl solution.

Concentration of MMT g/L	**R_s (Ω cm^2)**	**R_1 (Ω cm^2)**	**Q_1 (Ω^{-1} s$^{\alpha}$ cm^{-2})**	**α_1**	**R_2 (kΩ cm^2)**	**Q_2 (Ω^{-1} s$^{\alpha}$ cm^{-2})**	**α_2**
-	1.62	20.64	132.0	0.99	0.052	680.0	0.71
0.5	1.29	65.57	303.0	0.89	18.22	2996	0.64
1.0	4.23	730.0	258.0	0.82	16.28	963.0	0.58
2.0	3.91	280.5	321.0	0.88	11.08	321.0	0.51

7.5 Mechanical Properties

The averaged data for each sample are represented as the curves of Young's modulus (Figure 7.16) and hardness (Figure 7.17) for the layered silicate nanocomposites fabricated from different $[MoO_4^{2-}]/[Ni^{2+}]$ molar ratios of 0.1 and 0.2 incorporated with various MMT concentrations (0.5, 1.0, and 2.0 g/L). The nickel/molybdenum/layered silicate nanocomposite films incorporated with 1.0 g/L MMT both from the $[MoO_4^{2-}]/[Ni^{2+}]$ molar ratios of 0.1 and 0.2 bath have the greatest hardness and Young modulus values over the nickel/molybdenum alloy films. The high MMT concentration (2.0 g/L) introduced into the bath lead to lower mechanical strength compared to the alloy films. This is due to lower molybdenum content in the nanocomposites with an increase in MMT incorporation. However, the values of these films are still higher than that of the nickel/layered silicate nanocomposite films due to the incorporation of both molybdenum and layered silicates into the nickel film [20-21].

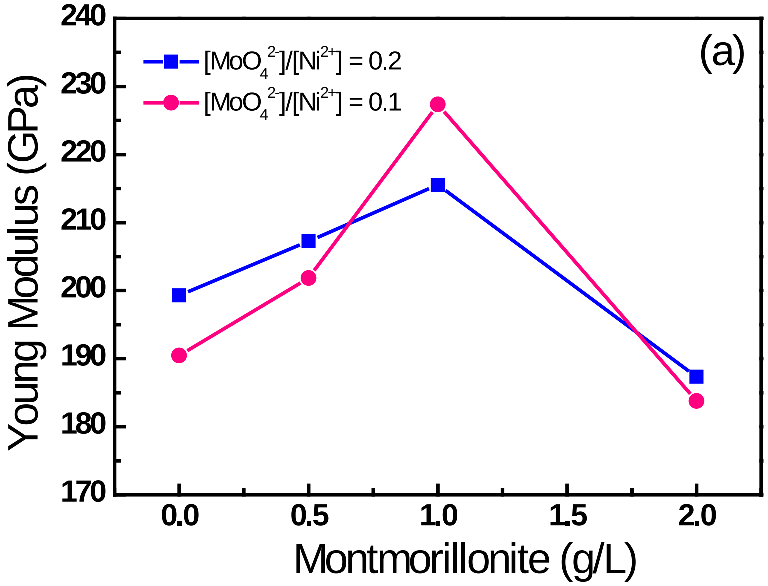

Figure 7.16: The influence of montmorillonite concentration (0.5, 1.0, and 2.0 g/L) on the Yong's modulus values of the nanocomposite films.

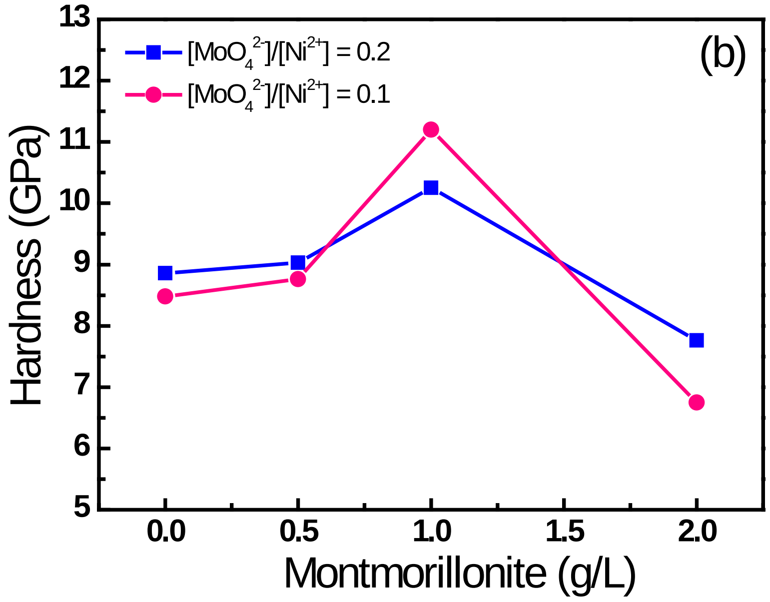

Figure 7.17: The influence of montmorillonite concentration (0.5, 1.0, and 2.0 g/L) on the hardness values of the nanocomposite films.

The incorporation of MMT particles into Ni-Mo matrix results into an increase in the film Young's Modulus (Figure 7.16) and hardness (Figure 7.17) but up to a maximum at MMT concentration 2% in the plating bath at higher concentrations there is a decrease in both the film hardness and young's modulus. The strengthening mechanism of the nanocomposite coating as compared to pure Ni-Mo is probably related to the load transfer from the softer metallic matrix to the harder composite.

There are three main reasons for the increase in hardness [74]: particle-strengthening, dispersion-strengthening and grain refinement. Particle-strengthening results from the incorporation of hard particles and volume fraction above 20%. In this case, the load is distributed between both the matrix and the particles where particles restrain the matrix deformation. Incorporation of fine particles (less than 1 micron) and volume fraction less than 15% results in dispersion-strengthening. In such case load is carried by matrix and the small particles hinder the dislocation motion. The third mechanism is grain refinement which results from the nucleation of small grains on the surface of the incorporated particles. In this case, the presence of smaller grains impedes dislocation motion resulting in an increase in the microhardness.

According to the results obtained here, the grain size was increased by embedding of MMT particles into the metal matrix without decreasing in the grain size of Ni-Mo, and the size of MMT platelets is not very small to cause dispersion-strengthening, so it can be concluded that the main reason for increase in the hardness of the nanocomposite coating compared to that of pure Ni-Mo is particle-strengthening.

7.6 Conclusion

Nickel/molybdenum/layered silicate nanocomposites are electrochemically deposited onto stainless steel to extend the lifetime of currently used materials surrounded in high stress and salt water brine environments. This work has shown that nickel/molybdenum/layered silicate nanocomposite films synthesized through electrochemical deposition techniques provide better corrosion protection and higher hardness and Young modulus values over nickel/molybdenum alloys, leading to the following conclusions:

- The XRD pattern showed that the embedding of MMT particles impeded the formation of nanocrystalline Ni-Mo alloy and led to increase in the grain size of Ni-Mo.
- Potentiodynamic polarization and impedance measurements showed higher corrosion resistance for Ni-Mo-MMT nanocomposite coatings compared to pure Ni-Mo alloy.
- The incorporation of MMT particles into Ni-Mo matrix results into a significant increase in the film hardness and Young's Modulus with a maximum values at 1g/L MMT concentration in the plating bath but decreases at higher concentrations.
- AFM micrographs showed higher surface irregularities and surface roughness for the nanocomposite films compared to the binary alloy.

7.7 Chapter References

[1] M.K. Surappa, P.K. Rohatgi, *J. Mater. Sci*. **1981**, 16, 983.

[2] S.C. Tjong, Z.Y. Ma, *Mater. Sci. Eng*. **2000**, 29 49.

[3] H.S. Lee, K.Y. Jeon, S.H. Hong, *J. Mater. Sci.* **2000**, 35, 6231.

[4] Y.L. Shen, A. Needleman, S. Suresh, *Matell. Mater. Trans. A*. **1994**, 25, 839.

[5] X.H. Han, Q. Wang, Y.G. Park, C. T'Jeon, A. Sommers, A. Jacobi, *Heat Transfer Eng*. **2012**, 33, 991.

[6] X. Qu, L. Zhang, M. Wu, S. Ren, *Prog. Nat. Sci. Mater. Int*. **2011**, 21, 189.

[7] J.L. Stojak, J. Fransaer, J.B. Talbot, in: R.C. Alkire, D.M. Kolb, Eds., *Advances In Electrochemical Science and Engineering*, Wiley-VCH Verlag.: Weinheim, 2002.

[8] Y.C. Chang, K.C. Fan, C.I. Lin, J. Chin. *Inst. Chem. Eng*. **2002**, 33, 499.

[9] M. Donten, H. Cesiulis, Z. Stojek, *Electrochim. Acta*. **2005**, 50, 1405.

[10] P. Kedzierzawski, D. Oleszak, M. Janik-Czachor, *Mater. Sci. Eng. A.* **2001**, 300, 105.

[11] D. Oleszak, V.K. Portnoy, H. Matyja, *Mater. Sci. Forum*. **1999**., 312 (4), 345.

[12] S.D. De la Torre, D. Oleszak, A. Kakitsuji, K. Miyamoto, H. Miyamoto, R. Martinezm-S, F. Almeraya-C, A. Martinez-V, D. Rios-J, *Mater. Sci. Eng. A.* **2000**, 276, 226.

[13] E.J. Podlaha, D. Landolt, *J. Electrochem. Soc*. **1996**, 143(3), 885.

[14] E.J. Podlaha, D. Landolt, *J. Electrochem. Soc*. **1997**, 144(5), 1672.

[15] E. Gómez, E. Pellicer, E. Vallés, *J. Electroanal. Chem*. **2005**, 580, 222.

[16] E. Beltowska-Lehman, A. Bigos, P. Indyka, M. Kot, *Surf. Coat. Technol*. **2012**, 211, 67.

[17] T. Ohgai, Y. Tanaka, R. Washio, *J. Solid State Electrochem.* **2013**, 17, 743.

[18] S. Yagi, A. Kawakami, K. Murase, Y. Awakura, *Electrochim. Acta.* **2007**, 52, 6041.

[19] C.C. Nee, W. Kim, R. Weil, *J. Electrochem. Soc*. **1988**, 135 (5), 1100.

[20] R. A Horch, T. D. Golden, N.A. D'Souza, L. Riester, *Chemistry of Materials.* **2002**, 14 (8), 3531-3538.

[21] J. Tientong, Y.H. Ahmad, M. Nar, N.A. D'Souza, A.M.A. Mohamed, T.D. Golden, *Materials Chemistry and Physics*. **2014**, 145(1), 44-50.

[22] J. Tientong, C. R. Thurber, N.A. D’Souza, A. Mohamed, T. D. Golden, *International Journal of Electrochemistry*. **2013**, 1-8.

[23] Y.H. Ahmad, J. Tientong, N. D'Souza, T.D. Golden, A.M.A. Mohamed, *Surface and Coatings Technology*. **2014**, 242, 170-176.

[24] A.Q. Wang, N.A. D'Souza and T.D. Golden, *Journal of Material Chemistry* **2006**, 16(5), 481-488.

[25] E. Ogunsona, S. Ogbomo, M. Nar and N.A. D'Souza, *Cellular Polymers.* **2011**, 30(2), 79-93.

[26] M.C. Richardson, J. Kim, D. Ho, C.R. Snyder, N.A. D'Souza and G.A. Holmes, P*olymer Composites*. **2011**, 32(1), 67-78.

[27] Q. Wang, N.A. D'Souza and T.D. Golden, *Applied Clay Science*. **2008**, 42, 310-317.

[28] A.Q. Wang, N.A. D'Souza and T.D. Golden, *Journal of Material Chemistry*. **2006**, 16(5), 481-488.

[29] D. Zaarei, A.A. Sarabi, F. Sharif and S.M. Kassiriha, *Journal of Coating Technology Research*. **2008**, 5, 241-249.

[30] A. Olad, M. Amini and A. Rashidzadeh, *Fibers and Polymers*. **2012**, 13, 475-480.

[31] C.W. Macosko, *Rheology: Principles, measurements and applications*, Ed. John Wiley & Sons: New York, 1993.

[32] C. Dedeloudis, J. Fransaer and J.-P. Celis, *Journal of Physical Chemistry B.* **2000**, 104, 2060-2066.

[33] A. M. L. Kraepiel, K. Keller and F. M. M. Morel, *Journal of Colloid and Interface Science.* **1999**, 210, 43-54.

[34] Luis Caceres, Tomas Vargas, Leandro Herrera, *Corrosion Science.* **2009**, 51, 971–978.

[35] Z. Cvijovic, G. Radenkovic, *Corrosion Science.* **2006**, 48, 3887–3906.

[36] A. J. Sedriks, *Corrosion of Stainless Steels,* 2nd Ed., Sponsored by The Electrochemical Society, Inc. Princeton: A Wiley-Interscience publication, John Willey & Sons, Inc.: New Jersey.

[37] R.-H. Jung, H. Tsuchiya, S. Fujimoto, *Corrosion Science.* **2012**, 58, 62–68.

[38] Y. C. Lu, M. B. Ives, C. R. Clayton, *Corrosion Science*. **1993**, 35(1-4), 89-96.

[39] J.M. Bastidas, C.L. Torres, E. Cano, J.L. Polo, *Corrosion Science*. **2002**, 44(3), 625–633.

[40] W.J. Tobler,S. Virtanen, *Corrosion Science*. **2006**, 48, 1585–1607.

[41] A.K. Mishra, D.W. Shoesmith, *Electrochimica Acta*. **2013**, 102, 328– 335.

[42] M.K. Ahn, H.S. Kwon, H.M. Lee, *Corrosion Science*. **1998**, 40(2-3), 307-322.

[43] G.O. Ilevbare, G.T. Burstein, *Corrosion Science*. **2001**, 43, 485-513.

[44] E. G´omez, E. Pellicer, M. Duch, J. Esteve, E. Vall´es, *Electrochimica Acta.* **2006**, 51, 3214-3222.

[45] M. Karolus, E. Rówiński, E. Łągiewka, *Journal of Achievements in Materials and Manufacturing Engineering.* **2006**, 18(1-2), 119-122.

[46] R. Mishra, R. Balasubramaniam, *Corrosion Science*, **2004,** 46(12), 3019–3029.

[47] L. Wang , J. Zhang , Y. Gao , Q. Xue , L. Hu , T. Xu, *Scripta Materialia.* **2006**, 55(7), 657-660.

[48] R. Mishra, B. Basu , R. Balasubramaniam, *Materials Science and Engineering: A,* **2004**, 373(1), 370-373.

[49] K.M.S Youssef, C.C Koch, P.S Fedkiw, *Corrosion Science*, **2004**, 46(1), 51–64.

[50] C.C. Koch, *J Mater Sci.* **2007**, 42, 1403-1414.

[51] Y. Xuetao, W. Yu, S. Dongbai, Y. Hongying, *Surface and Coatings Technology*, **2008**, 202(9), 1895-1903.

[52] T. Ohgai, Y. Tanaka, R. Washio, *J. Solid State Electrochem*. **2013**, 17, 743-750.

[53] T. Haubold, R. Bohn, R. Birringer, H. Gleiter, *Materials Science and Engineering: A,* **1992**, 153(1-2), 679–683.

[54] W.Z. Friend, *Corrosion of nickel and nickel-base alloys*, Ed., Willey-Interscience: New York, 1980.

[55] E. Chassaing, M. P. Roumegas, M. F. Trichet, *Journal of Applied Electrochemistry*, **1995**, 25(7), 667-670.

[56] R.S. Jayashree, P. Vishnu Kamath, *J. Power Source.* **2001**, 39, 273.

[57] E. Gomez, E. Pellicer, E. Valles, *J. Electroanal. Chem.* **2001**, 517, , 109.

[58] Y. Zeng, L. Zelin, M. Ming, Z. Shaomin, *Eletrochem. Commun.* **2000**, 2, 36.

[59] F.A. Marinho, F.S.M. Santana, A.L.S. Vasoconcelos, R.A.C. Santana, S. Prasad, J. Brazil. *Chem. Soc.* **2002**, 13 522.

[60] T. Sato, H. Takahashi, E. Matsubara, A. Muramatsu, *Mater. Trans.* **2002**, A 43, 1525.

[61] Abner Brenner, *Electrodeposition of Alloys: Principles and Practice*, Academic Press, 1963.

[62] T. Ohgai, R. Washio, Y. Tanaka, *Journal of Electrochemical Society*, **2012**, 159(10), H800-H804.

[63] S. Sun, E. J. Podlaha, *Journal of Electrochemical Society.* **2012**, 159(2), D97-D102.

[64] S. M.J. Ksycki, L. F. Yntema, *J. Electrochem. Soc.* **1949**, 48-56.

[65] T. A. Green, A. E. Russell, and S. Roy, *Journal of the Electrochemical Society*. **1998**, 145, 3875–3881.

[66] C.-Q. Li, X.-H. Li, Z.-X.Wang, and H.-J.Guo, *Transactions of Nonferrous Metals Society of China*. **2007**, 17(6), 1300-1306.

[67] O. Y. Zelenin, *Russian Journal of Coordination Chemistry.* **2007**, 33(5), 346-350.

[68] S. Rode, C. Henninot, and M. Matlosz, *Journal of the Electrochemical Society*. **2005**, 152(4), C248-C254.

[69] E. Chassaing, M. P. Roumegas, M. F. Trichet, *Journal of Applied Electrochemistry*. **1995**, 25(7), 667-670.

[70] D. Landolt, A. Marlot, *Surface and Coatings Technology*. **2003**, 169, 8–13.

[71] A Marlot, P Kern, D Landolt, *Electrochimica Acta.* **2002**, 48(1), 29-36.

[72] N.S Qu, D Zhu, K.C Chan, W.N Lei, *Surface and Coatings Technolog.* **2003**, 168(2-3), 123–128.

[73] M. Donten, H. Cesiulis, Z. Stojek, *Electrochimica Acta*. **2005**, 50, 1405-1412.

[74] A. Robin, R.Q. Fratari, *J. Appl. Electrochem.* **2007**, 37, 805-812.

CHAPTER 8

CONCLUSIONS AND FUTURE WORK

8.1 Conclusions

Electrodeposited nickel and nickel alloy films were examined for increased corrosion resistance and hardness properties. In addition, a layered silicate, specifically montmorillonite (MMT) was incorporated into the films to further enhance these properties. The films were deposited on stainless steel substrates from the following electrochemical plating solutions:

(1) Nickel sulfate, sodium citrate, at pH 1.6, 2.5, 3.0 and 9.0

(2) Nickel sulfate, sodium citrate, 5g/L MMT at pH 1.6, 2.5, 3.0 and 9.0

(3) Nickel in the Watt's bath solution

(4) Nickel in the Watt's bath solution with 10, 30 and 50 g/L MMT

(5) Molybdenum/nickel alloy, molar ratio 0.1 and 0.2 at pH 9.5

(6) Molybdenum/nickel alloy, molar ratio 0.1 and 0.2 with 0.5, 1.0 and 2.0 g/L MMT at pH 9.5

Nickel/layered silicates and Nickel/molybdenum alloy/layered silicates were electrochemically deposited from acidic and alkaline bath solutions. Citrate was used as a ligand to stabilize Ni^{2+} ions in the plating solution. MMT was exfoliated by stirring in an aqueous solution for over 24 hours. The plating solutions were analyzed for zeta-potential, particle size, viscosity, and conductivity to investigate the effects of the composition at various pHs. These findings are summarized in Table 8.1.

The conductivity and viscosity of the solutions was used to determine the optimal plating bath conditions for the deposits. Particle size and zeta potential were used to further aid in understanding the dynamics of each system.

Table 8.1: Electrochemical plating solution property measurements.

MMT (g/L)	Ni plating solutions w/ or w/o MMT (g/L)	Conductivity (mS/cm, n=3)	Viscosity (cSt, n=3)	Particle size (nm)	Zeta potential (mV, n=3)
0.5	MMT solution	0.053	0.912 ± 0.001	447	-41.7 ± 0.6
1	MMT solution	0.106	0.929 ± 0.002	553	-42.6 ± 1.4
2	MMT solution	0.207	1.001 ± 0.002	586	-39.6 ± 0.6
5	MMT solution	0.502	1.003 ± 0.003	591	-43.2 ± 0.8
10	MMT solution	1.48	1.009 ± 0.01	674	-41.4 ± 0.9
30	MMT solution	2.59	1.16 ± 0.01	1835	-41.9 ± 0.8
50	MMT solution	5.59	18.4 ± 0.1	4079	-26.3 ± 1.4
5	Ni-MMT-Cit pH 1.6	24.3 ± 0.1	2.86 ± 0.03	3120	-10.1 ± 0.3
5	Ni- MMT-Cit pH 2.5	28.1 ± 0.2	2.64 ± 0.01	2756	-22.2 ± 0.9
5	Ni- MMT-Cit-pH 3.0	33.7 ± 0.3	2.21 ± 0.02	2517	-21.9 ± 0.4
5	Ni-MMT-Cit pH 9.0	18.9 ± 0.2	1.22 ± 0.02	1358	-36.7 ± 0.3
1	Ni Watt's bath-MMT	51.8 ± 0.2	1.20 ± 0.01	>7000	-13.5 ± 0.7
5	Ni Watt's bath-MMT	50.2 ± 0.2	2.77 ± 0.05	>7000	-18.3 ± 0.6
10	Ni Watt's bath-MMT	50.0 ± 0.2	17.8 ± 0.8	>7000	-17.4 ± 0.6
30	Ni Watt's bath-MMT	46.2 ± 0.3	1299 ± 12	>7000	-9.5 ± 0.7
50	Ni Watt's bath-MMT	43.5 ± 0.4	>3000	>7000	-1.9 ± 0.7
0.5	$[MoO_4^{2-}]$ / $[Ni^{2+}]$ mole ratio of 0.1	25.06	1.025± 0.000	3058	-34.0 ± 0.1
1.0		25.24	1.112 ± 0.003	3690	-37.1 ± 0.4
2.0		25.29	1.327 ± 0.001	4020	-35.0 ± 0.7
0.5	$[MoO_4^{2-}]$ / $[Ni^{2+}]$ mole ratio of 0.2	25.54	1.051 ± 0.002	2290	-32.8 ± 0.2
1.0		25.85	1.177 ± 0.003	2832	-33.6 ± 0.5
2.0		25.92	1.471 ± 0.011	3570	-34.8 ± 1.4

Initially, the MMT was examined in water without metal salts or complexing agents to determine optimal concentration addition of MMT into the pre-established plating bath systems for nickel and nickel-molybdenum alloys. The ionic conductivity of MMT in water (0.053 to 5.59 mS/cm) increased with increasing MMT concentration (0.5 to 50 g/L). As the MMT becomes delaminated, sodium ions are released in the solution (MMT is Na^+-Cloisite), leading to an increase in the overall conductivity of the solution. The viscosity of the MMT solution (0.912 to 18.4 cSt) and particle size (447 to 4079 nm) increased with increasing MMT concentration in the solution due to an increase in the number of platelets. The zeta potential of MMT for the concentration range of 0.5 to 30 g/L is in the range of -39.6 to -43.2 mV. As the MMT concentration was increased to 50 g/L the solution stability decreased as demonstrated by a decrease in zeta potential (-26.3 mV) and an increase in particle size (4079 nm).

The nickel citrate based plating systems were studies with and without the addition of MMT. The nickel citrate plating systems were examined at a range of pH including 1.6, 2.5, 3.0 and 9.0. At pH lower than 2, most of the nickel exists as free nickel ions (Ni^{2+}). At pH 2.5-3.0, nickel-citrate complexes are formed including NiCitH and NiH_2Cit^+ while at pH 9 most of the Ni is complexed with citrate as $[Ni(C_6H_4O_7)]^{2-}$. The Ni-MMT-Cit solution at lower pH (pH 1.6 to 3.0) had a higher conductivity (24.3 to 33.7 mS/cm) than the system at pH 9 (18.9 mS/cm). The viscosities of Ni-MMT-Cit in acidic solution (pH 1.6 to 3.0) decreased from 2.86 to 2.21 cSt and were higher than that the Ni-MMT-Cit at pH 9.0 (1.22 cSt). The viscosities under acidic conditions are higher than alkaline conditions due to the agglomeration effect. Under acidic conditions, there is an attractive force between Ni^{2+} and NiH_2Cit^+ ions with the negatively charged MMT. The solution particles at pH 2.5 (−22.2 mV) and pH 3.0 (−21.9 mV) were more stable than at pH 1.6 (−10.1mV) as shown by zeta-potential values of the Ni-MMT-Cit plating solution (Table 8.1). Under alkaline conditions, the nickel ions are complexed with citrate creating a $[Ni(C_6H_4O_7)]^{2-}$ complex, resulting in a repulsive force between the nickel citrate complex and negatively charged MMT particles. This effect is also seen in the particle size and zeta potential values. Smaller particle size (1358 nm) and increased zeta potential (-36.7 mV) is observed in the alkaline solution as compared to those in the acidic bath. In the acidic bath the particle size decreased from 3120 to 2517 nm with increasing pH from 1.6 to 3.0.

All coatings from the Watt’s bath with different MMT concentrations (1-50 g/L) had higher conductivities (43-52 mS/cm) than the Ni-Cit-MMT bath (18.9-24.3 mS/cm) due to high nickel concentration in the system. The viscosities increased from 1.20 to >3000 cSt as the MMT concentration was increased from 1 to 50 g/L. The particle sizes measured from the Watt's bath were larger than 7 μm. The high nickel concentration in the bath increased the agglomeration effect leading to decreased stability of the particles suspended in the solution as shown by the zeta potential values (-1.9 to -18.3 mV).

The molybdate-nickel molar ratios of 0.1 and 0.2 with different MMT concentrations (0.5 to 2.0 g/L) showed similar solution properties including conductivities (~25 mS/cm), viscosities (~1.1 cSt), particle sizes (~3 μm), and zeta potential values (~35 mV) corresponding to the same suspension stability resulting in the homogenous incorporation of MMT into the Ni/Mo alloy coatings.

The coatings from the described plating solutions were examined for corrosion potential, corrosion current, resistance, Young's modulus and hardness of the films. These findings are summarized in Table 8.2.

Table 8.2: Summarized characterizations of electrodeposited coatings.

Ni Plating solutions w/ or w/o MMT (g/L)		E_{corr} (V)	i_{corr} ($\mu A\ cm^{-2}$)	Rp ($k\Omega\ cm^2$)	Modulus (GPa)	Hardness (GPa)
Ni-5MMT-Cit pH 1.6		-0.320	0.902	147	147.2 ± 50.4	4.1 ± 1.5
Ni-5MMT-Cit pH 2.5		-0.340	0.948	184	173.5 ± 52.3	3.3 ± 1.2
Ni-5MMT-Cit-pH 3.0		-0.390	0.734	116	233.9 ± 56.5	5.3 ± 1.6
Ni Watt's bath		-0.283	4.270	114	-	430kgf/mm^2 Vickers
Ni Watt's bath-10MMT		-0.274	0.584	625	-	530kgf/mm^2Vickers
Ni Watt's bath -30MMT		-0.316	1.460	221	-	545kgf/mm^2Vickers
Ni Watt's bath -50MMT		-0.296	2.960	141	-	515gf/mm^2Vickers
Ni-Cit-pH 9		-0.370	3.240	131	163.1 ± 53.6	3.8 ± 1.6
Ni-5MMT-Cit-pH 9		-0.290	1.230	210	224.3 ± 21.6	5.9 ± 0. 8
$[MoO_4^{2-}]$ / $[Ni^{2+}]$ mole ratio of 0.1	No MMT	-0.460	5.700	67.7	190.5±14.1	8.48±1.1
	0.5 g/L MMT	-0.400	0.131	217.9	201.46±12.5	8.76±0.6
	1.0 g/L MMT	-0.350	1.700	73.4	227.4±16.3	11.2±1.3
	2.0 g/L MMT	-0.330	6.340	32.6	183.8±17.2	6.75±1.5
$[MoO_4^{2-}]$ / $[Ni^{2+}]$ mole ratio of 0.2	No MMT	-0.470	2.000	80.0	199.3±12.3	8.86±0.9
	0.5 g/L MMT	-0.420	0.631	197.5	207.3±11.7	9.03±1.4
	1.0 g/L MMT	-0.360	1.000	107.0	215.5±15.1	10.25±1.1
	2.0 g/L MMT	-0.340	1.260	87.8	187.32±16.8	7.76±1.6

E_{corr} of the Ni-MMT-Cit films ranged from −0.320 to −0.390 V with varying pH from 1.6 to 3.0 (Table 8.2). The film coated from Ni-MMT-Cit at pH 3.0 gave the lowest i_{corr} (0.734 µA cm^{-2}) as compared to the more acidic baths of pH 1.6 and 2.5. Although the R_p value for the film coated at pH 3.0 was lowest (116 kΩ cm^2) compared to pH 1.6 (147 kΩ cm^2) and pH 2.5 (184 kΩ cm^2), it seems to give lower current density when polarized anodically implying stable passive nickel oxide film formation on the coating. The films were immersed in a 3.5% NaCl solution and the open circuit potential was monitored for one month. The coatings deposited at pH 3.0 were stable 13 days longer in the salt solution than the coatings at pH 1.6 and 2.5. X-ray diffraction showed a change in the (111)/(200) ratio for the coatings at the various pHs. Scanning electron microscopy (SEM) and hardness results showed the electrodeposition of nickel/layered silicates at pH 3.0 (234 GPa) had improved hardness and morphology compared to pH 2.5 (174 GPa) and pH 1.6 (147 GPa).

Films deposited onto stainless steel from a plating solution adjusted to pH 9 containing nickel sulfate, sodium citrate, and incorporated with 5 g/L MMT exhibited improved stability and adhesion. Pure nickel films cracked and peeled from the substrate when immersed in 3.5% NaCl solution within 5 days, while the nanocomposite films remained attached even after 25 days. The Ni-Cit-pH 9 without MMT coating had a corrosion potential of E_{corr}= -0.370 V, corrosion current of i_{corr} =3.24 µA cm^{-2}, and resistance value of R_p = 131 kΩ cm^2. The Tafel parameters shown in table 8.2 for Ni-5MMT-Cit-pH 9 including E_{corr} (-0.290 V), i_{corr} (1.23 µA cm^{-2}), and R_p (210 kΩ cm^2) showed improved corrosion resistance over the pure Nickel layered silicate composites, a 25% increase in Young’s modulus (224.3 GPa) and a 20% increase in hardness (5.9 GPa) over pure nickel films (163.1 GPa and 3.8 GPa, repectively).

Pure nickel and nickel/layered silicate composite coatings were produced using pulse current electrodeposition from a Watt's type bath. Experimental results showed that the codeposition of layered silicate particles into the nickel matrix improved the microhardness of the coatings and modified the [100] texture of the pure nickel deposits to a mixed crystal orientation through [100] and [211] axes. Nickel/layered silicate nanocomposite coatings show improved corrosion resistance in simulated seawater as compared to pure nickel as indicated in the electrochemical polarization and impedance measurements. SEM and AFM micrographs indicate a reduction in the nickel crystallite grain size and increase in the surface roughness of the film due to embedding of MMT particles in the nickel matrix. The corrosion resistance from the Watt's bath for Ni-10MMT showed the most noble corrosion potential (E_{corr} -0.274 V), the lowest i_{corr} (0.584 µA cm^{-2}) and highest R_p (625 kΩ cm^2) as compared to the pure Ni film and Ni films incorporated with higher MMT concentrations (30 and 50 g/L). Ni coatings from the Watt's bath with 10, 30 and 50 g/L MMT incorporation displayed improved microhardness values (530, 545, and 515 kgf/mm^2, respectively) over the pure Ni film (430 kgf/mm^2) under the same plating conditions.

The nickel-molybdenum alloys deposited through modified pulsed potential electrochemical deposition at ambient temperature provided nanocrystalline coatings with reduced grain size (5.5-6.4 nm) as compared to the nickel crystalline grain (19.8 nm). The smaller grain size is preferred as it is known to result in improved corrosion resistance with enhanced mechanical properties. The Ni/Mo alloys demonstrated an increase in the corrosion resistance in 3.5% sodium chloride solution as compared to a pure Ni film. The incorporation of molybdenum creates a molybdenum oxide film which is able to self-heal from pitting nucleation. The Ni/Mo films showed a wider passivation region over the Ni film which also leads to increased corrosion resistance. The Young's modulus for different Mo contents (15-30 wt%) are higher (189-194 GPa) over the pure Ni film (143 GPa). The hardness values for the Ni-Mo films (8.3-8.6 GPa) also increased over the pure Ni film (4.3 GPa).

Ni/Mo and Ni/Mo/MMT nanocomposite coatings were prepared by electrodeposition from an alkaline citrate bath (pH 9.5) containing different concentrations of exfoliated MMT (0.5, 1.0, and 2.0 g/L). XRD results revealed that embedding the layered silicate modified the texture of the Ni/Mo matrix and lead to an increase in the grain size. Nanoindentation measurements showed increased hardness (11 GPa) and Young's modulus (230 GPa) for the nanocomposite coatings containing low content of the layered silicate (1.0 g/L) compared to pure Ni/Mo films (8.6 GPa and 189 GPa, respectively). The potentiodynamic polarization and electrochemical impedance measurements showed that the Ni/Mo/MMT nanocomposite coatings had higher corrosion resistance in 3.5% NaCl solution as compared to pure Ni-Mo films. SEM and AFM micrographs showed a slight increase in the particle size and surface roughness of the electrodeposited films as a result of incorporation of MMT particles into Ni-Mo alloy matrix.

In summary, for the electrodeposited Ni-MMT films, in a citrate stabilized bath with increasing pH from acidic to alkaline conditions, the E_{corr} values tended to shift to a more noble potential. As the pH was increased, the i_{corr} values increased; however, R_p values also increased implying a decline in the corrosion rate of the film (Table 8.2). The increased R_p values are influenced by anodic (β_a) and cathodic (β_c) slope parameters which is more pronounced when the i_{corr} values of the films are not significantly different. With increasing pH, the hardness values tended to increase implying that MMT preferred to insert into Ni coatings at higher pH. This is also suggested due to increased zeta potential values at higher pH (Table 8.1). The coatings incorporated with MMT were harder than the corresponding pure Ni films confirming MMT incorporation into the Ni matrix.

8.2 Future Work

1) The incorporation of layered silicate leads to an overall improvement in corrosion resistance and hardness properties. However, nickel-layered silicate and nickel-molybdenum-layered silicate nanocomposite films must be examined under standard engineering material testing parameters including abrasive or wear resistance, adhesive strength, and ductility to determine the mechanical strength of the material. The deposits should not crack while in service either as a result of internal stress or external loading. The incorporation of layered silicate into metal matrix should not be brittle. The coatings should not fail before the substrate material. The basic characteristics of strength and ductility of the metal are exhibited by the stress-elongation diagram. The tangent to the slope of this diagram is equivalent to the modulus of the elasticity of the material. The characteristic point consequently shows the limiting value of ductility and strength. Wear resistance and hardness are related to these properties. The simplest adhesion measurement such as grinding, polishing or scratching/brushing also could be used to examine film with less than 30 μm thickness and the test should be short, i.e. 15 s.

2) Determining the heat stability of the coating and thermal expansion for nickel-molybdenum-layered silicate films is of interest.

3) The coatings before and after corrosion measurements should be investigated for metal oxide generation by XPS.